Development of Improved Graphene Production and Three-dimensional Architecture for Application in Electrochemical Capacitors

by

Victor Chabot

A thesis
presented to the University of Waterloo
in fulfillment of the
thesis requirement for the degree of
Master of Applied Science
in
Chemical Engineering - Nanotechnology

Waterloo, Ontario, Canada, 2013

Author's Declaration

I hereby declare that I am the sole authors of this thesis. This is a true copy of my thesis, including any required final revisions, as accepted by my examiners.

I understand that my thesis may be made electronically available to the public.

Abstract

With the worlds increasing energy demand there is growing concerns for the development of clean portable energy storage devices. This fuels the large amount of research being pursued by the development of fuel cells and batteries which offer high energy storage. However, one of the major advantages of oil as an energy source is it can be used to conjure large quantities of power in short time periods. This is where electrochemical capacitors can continue to carve out a niche market supplying moderate energy storage, but with high specific power output. The market, since its inception in the 1970's has been dominated by electrochemical double layer type capacitors made with high surface area activated carbon materials. Variation in pore size, shape and network structure between carbon precursors necessitates further development. Further, production requires high temperature, energy intensive carbonization to create the active pore sites and develop the pores.

Double-layer capacitive materials researched to replace active carbons generally require properties that include: very high surface area, high pore accessibility and wettability, strong electrical conductivity, structural stability, and optionally reversible functional groups that lend to energy storage through pseudocapacitive mechanisms. Heteroatom rich carbon precursors, template and fibrous carbons offer an alternative to traditional activated carbons from coke and pitch; however these materials can suffer from difficult preparation procedures or deficient physical properties with respect to the criteria listed above. In recent years, nanostructured carbon materials which could in future be tailored through bottom up processing have the potential to exhibit favourable properties have also contributed to the growth in this field.

This thesis presents research on graphene, an emerging 2-dimensional carbon material derived from an abundant, cheap graphite precursor. So far, production of graphene in bulk exhibits issues

including restacking, structural damage and poor exfoliation. However, the high chemical stability, moderate conductivity and high electroactive behaviour even with moderate exposed surface area makes them an excellent standalone EDLC material or a potential support material. Two projects presented focus on enhancing the capacitance through functionality, finding new production methodology and controlling graphene formation to enhance performance and utility.

The first study addresses graphene enhancement possible with heteroatom functionality, produced by a single step low temperature hydrothermal reduction process. In contrast to other work utilizing high temperature and vaporized nitrogen precursors such as ammonia. The dopant methodology was successful in adding nitrogen functionality to the reduced graphene oxide basal and the effect of nitrogen type was considered.

The second study addresses the need for greater control of the rGO structure on the macro-scale and lessening processing complexity. By harnessing the change in interactions between the GO intermediate and final rGO sheets we were able to induce and control the assembly of graphene, creating micro and macro-pore order and high performance. Several production methodologies have been investigated and once their processes were optimized, tested for capacitive performance. Self assembly directly onto the current collector eliminates process steps involved in the production of EDLC electrodes and further investigation into performance optimization was considered.

Acknowledgements

I would first like to give thanks to my family and friends, specifically Amanda Carruthers, for their support and patience throughout my time here. A special thank you goes to my supervisor, Dr. Aiping Yu for her support, advice in my research and for offering opportunity to take part in other projects. I would also like to thank Dr. Luis Sandoval, Dr. Zhongwei Chen and my colleagues including: Aaron Davies, Brian Kim, Fathy Hassan, Zhu Chen, Drew Higgins, Dong Un Lee, Jordan Scott and Jason Wu for their assistance and support.

Table of Contents

List of Figures

List of Tables

List of Abbreviations, Symbols and Nomenclature

A	Shape Factor
B	Full Width Half Maximum
AA	Ascorbic Acid
AC	Activated Carbon
BET	Brunauer-Emmett-Teller
C_s	Specific Cell Capacitance
C_m	Specific Material Capacitance
CD	Charge discharge Chronopotentiometry
CNT	Carbon Nanotubes
CVD	Chemical Vapor Deposition
CV	Cyclic Voltammetry
d	crystal lattice spacing
DOE	Department of Energy
E	Energy Density
EDA	Ethylenediamine
EPA	Environmental Protection Agency
EDLC	Electronic Double Layer Capacitor
EIS	Electrochemical Impedance Spectroscopy
ES	Electrochemical Supercapacitor
ESR	Equivalent Series Resistance
EDX	Energy Dispersive X-ray
Ex-rGO	Rapidly reduced/exfoliated GO
f	mass fraction

FD-rGO	Freeze Dried Graphene Oxide, Reduced
FWHM	Full width at half maximum
FTIR	Fourier Transform Infrared Spectroscopy
GO	Graphene/Graphitic Oxide
HPGC	Highly Porous Graphitized Carbon
I	Current
L_c	Size of Crystal Domins
m	Mass
NG	Nitrogen Doped, Reduced Graphene Oxide
P	Power
q	Charge
rGO	Reduced Graphene Oxide
R	Resistance
R_p	Parallel Leakage/Charge Transfer Resistance
RS	Raman Spectroscopy
SA-rGO	Reduction Induced Self Assembled Graphene Oxide
SCE	Saturated Calomel Electrode
SEM	Scanning Electron Microscopy
SSA	Surface Area
t	Time
TEM	Transmission Electron Microscopy
V	Voltage
XRD	X-ray Powder Diffraction
XPS	X-Ray Photoelectron Spectroscopy
Z	Impedance

ρ	density
λ	Wavelength
θ	Angle

Section 1: Introduction of Thesis Project

The world's energy needs are increasing dramatically and along with it the development of a sense of awareness and environmental responsibility. The need for sustainable and recyclable energy technologies is becoming a key societal issue, made more pressing by the depletion of fossil fuels which are expected to run out in the next few decades if energy policy does not change. According to the United States Environmental protection agencies (EPA) global emission data, through 2004; electricity supply and transportation accounted for 26% and 13% of global greenhouse gas emissions, respectively [1]. Batteries and fuel cell technologies are posed to capitalize on the electrification of the supply chain as opposed to emission sensitive fuels with high energy density.

However, both batteries and fuel cells lack the high power density required to compete with the immediate and variable power supplied by fuel. At high loads, battery efficiency begins to drop due to side reactions. Limitations stem from an insufficient ability for ions to diffuse from bulk and for reaction rates to meet the power requirements put on the electrode materials. Thermal side reactions waste energy as heat, increasing the changes of by-product phase shift reactions. Stress caused from operating a battery beyond its rated power level can significantly decrease cycle lifetime through reduced storage ability and material corrosion. Grid storage from clean energy, will be incredibly important to displacing the energy supply because of the non-constant energy generation of wind and solar technologies. The ability to quickly and efficiently store peak energy requires high charging rates or else the systems must off-load excess energy as heat. In electric vehicles high power advantages can be realized with recapturing energy through regenerative breaking and in the efficient use of energy during acceleration events. This creates a potential market for high power energy storage devices known as supercapacitors used as stand-alone or in hybrid systems with high energy

storage systems such as batteries. Electrical double-layer capacitors (EDLCs) incorporate an electrolyte that allows charged ions to assemble on porous electrode surfaces with much higher areas than traditional parallel plate and electrolytic capacitors. The charge is separated by only 5 to 10 angstroms, which in combination with high surface area the small charge separation enables the generation of farad scale charges [2],[3].

In addition, the rapid growth of mobile electronics and alternative energy vehicles have created a need for advanced electrochemical energy storage devices with high power capabilities. Although the power density of supercapacitors still far exceeds that of batteries and the cycle life of carbon based EDLC's is in excess of 100000 cycles, there is still much work to be done to boost energy density. This is being achieved by continued development of electrode materials, composites, hybridizations, and suitable electrolytes to improve performance and reduce costs.

1.1 Summary of Objectives and Motivation

This project is focused on the development of next-generation, high-energy density supercapacitor materials. These materials are based on the modification of graphene, a few layer derivative of graphite. In theory, few layer graphene materials are an ultra-high surface area material with high conductivity and exceptional double-layer capacitance. These properties make it a very competitive material for next-generation supercapacitors. However, in practice the surface area and conductivity achieved for supercapacitor applications are still much lower than that offered by theory. Because of this, there is constant motivation to produce graphene materials that better harness the theoretical capacity promised by graphene. This project is focused on accomplishing improved capacitance through the control of surface structure and interaction between graphene sheets.

In the first part of this project the objective is to develop nitrogen doped graphene which has been previously shown to enhance conductivity and provide an improvement to graphene's capacitance, although upon initiation of this project the mechanism of enhancement is still largely unknown. The objective of this part of the project is to investigate and design a hydrothermal process that enables nitrogen doping at relatively low temperatures, while still achieving high performance seen by producing doped graphene by high temperature annealing.

In the second part of this project, the objective is to synthesize a three dimensional graphene network capable of providing porous ion channels, while maintaining high network conductivity on a macroscale. There is significant motivation for this approach. Firstly, combination of the active material synthesis and electrode preparation can simplify production. Ideally, a free-standing network would drastically reduce the inactive cells mass by removing components including current collectors, binder materials and conductive additives. The objective is to remove some, if not all, of these components based on the success of this work. This technique will also be important for harnessing graphene in composite with pseudocapacitance and high voltage electrolytes that have the ability to significantly boost the overall energy density of current carbon based supercapacitors. The main goal is to design a three dimensional graphene electrode which can be utilized for future projects involving either novel electrolytes or the growth of pseudocapacitive materials with high energy density and the retention of high ion and electron transport pathways.

1.2 Organization of Thesis

This thesis, which explores two separate methodologies for improving graphene performance, is divided into seven sections. Section 1 is intended to provide the reader with a general knowledge of the research goals and objectives. In addition, this section highlights the importance of this work.

Section 2 provides a background on supercapacitors and the important factors which govern performance. In addition, Section 2 provides a literature review on the development of both the commercial activated carbon materials and other more advanced carbon derivatives being considered for next generation batteries. This background is important for the reader to follow and understand the content discussed in later sections. Section 3 provides an additional ongoing literature review on the structure and techniques used to prepare three dimensional graphene materials, as well as, their focus for use in supercapacitors. Due to rapid developments in this field it is important that part of this project include, remaining aware of advances occurring simultaneous to this project. Part of this review has been altered and presented in Section 3, while the review in its entirety is subject to future publication. Section 4 discusses the theory behind the characterization/analysis techniques discussed throughout the literature and important to this project. Sections 5 and 6 describe the experimental work completed during this project, which attempt to produce high capacitance graphene. These sections introduce and describe the motivation for the work, explain the experimental procedures and discuss/summarize the results. Section 5 is based on previously published work, while section 6 focuses on the development of a platform for work to be published in the future. Section 7 provides a summary of the projects results and a brief discussion on the direction of future work.

Section 2: Electrode Materials for Electrochemical Supercapacitors

2.1 Introduction

In order to better understand and design materials for supercapacitors, a review of the current market for supercapacitor materials is required. A fundamental understanding of supercapacitor design, operation, performance, and component optimization will lead to future improvements of supercapacitor performance. However, equipped with knowledge of the current technology this project can focus in future chapters on trying to enhance the important characteristics of these materials.

Presently, activated carbon (AC) materials made from coal pitch precursors are the industrial standards for ESs, although newer materials and process variation can alter the characteristics of AC materials. Improvements to AC are under investigation in attempts to improve pore structures and increase surface areas through templating AC carbon, functionalization, and generating AC using different precursor materials. This project is focused on the application of more advanced carbons, such as: carbon nanotubes (CNTs), carbon nano-onions, and graphene. These electrode materials have been shown to offer a variety of improved properties because of their small size scales in at least one dimension, enabling the possibility of large area and improved performance. Therefore, literature review of these materials is presented in addition to the electrode parameters which govern their future potential for energy storage. Also considered, are the effects and design impacts of utilizing pseudocapacitive materials and selecting an electrolyte. This chapter is important in order to select an advanced carbon platform with promising performance, as well as, to determine what electrode properties are required to utilize pseudocapacitance or high voltage electrolyte in future work.

2.2 Electrode Requirements

Static storage mechanisms in EDLCs efficiently store charges upon the electrodes at high rates. Unlike rechargeable batteries, ESs involves no chemical breakdown or redeposition of electrode materials during operation. This lowers the risk of electrode phase changes during operation and enables long electrode cycle lives. The static charge storage in EDLCs enables the anode and cathode to be interchangeable and unlike specific electrode requirements seen in many batteries, the anode and cathode of an EDLC are composed of the same material. If the positive and negative current collector terminals and cell casing are also made of similar materials, theoretically the EDLC has no true polarity [4]. The important requirements for the optimization of electrode materials include:

-Minimal irreversible redox processes

-High specific surface area

-Thermodynamic stability for a large potential window of operation

-Ability to control morphology, pore size, particle size, and material distribution

-Surface wettability

-High electrical conductivity

2.2.1 Electrode Conductivity

Strong electrical conductivity is important in enabling ES devices to operate at high power. During discharge, charges stored within the material must effectively maneuver through the thick electrode layers and out to the circuit. Electron transport is dependent upon the quality of conductive pathways within the material and the conductivity of the material used in the electrode. If the conduction through the electrode is not strong enough or the path is too tortuous, performance will suffer. If there is too much resistance high power will not be achievable, as charges will not be able to respond

quickly enough to match the rated load of the circuit. This is because the high capacitance provided by a poorly conductive material at very low power will be much lower at a desirable power output. Charges cannot organize efficiently to match the load and some charges will dissipate as heat to meet the current demanded by the circuit load. Eventually the device will no longer be able to meet the power demands and the ES will no longer store any charge. For poorly conducting electrodes, this will happen at much lower current density.

Metals used in traditional capacitors utilize highly conductive metals as electrode materials that can achieve very high power; however, ESs commonly use carbons as the active electrode components. Not all carbon is sufficiently conductive to support high power operation. Graphitic planes are highly conductive but temperatures used in the activation processes are limited to prevent complete restructuring into nonporous graphite.

A balance is achieved between conductivity of the active carbon and porosity, which in effect translates to better capacitive performance. The result is that many active carbon materials lack sufficient conductivity to support long range or short range conduction of current within the electrode layer. To restrict the range over which carbon conduction must occur, metal collectors are used as supports for the carbon layer. Further, when the active carbon is unable to effectively conduct over short distances, specifically designed small carbon additives (e.g., carbon black, Super P) are used to increase the conduction of the electrode, although they carry little capacitive storage themselves.

In electrochemical supercapacitors, the equivalent series resistance (ESR) involves: the contact resistance between the current collector and the electrode layer, the inter-particle resistance of the electrode layer due to the porous electrode matrix, the resistance of the external lead contacts, the resistance of the electrolyte, and the resistance caused by the dielectric loss of the solvent and ions

when the AC frequency is higher than hundreds of megahertz (MHz). At very high frequencies, a phase delay occurs because the molecular relaxation of the dielectric is kinetically limited and polarization cannot occur quickly enough [5]. The reported effective ESR is taken from a Nyquist plot of real versus imaginary impedance. At high frequency approaching infinity, the imaginary impedance tends to zero as the capacitor becomes an AC short circuit. The ESR can be taken from the phase delay or intercept of the real impedance at high frequency. Alternatively, the ESR can be determined from the voltage drop seen during constant current discharge.

ESR is an important parameter in evaluating a supercapacitor's performance, in particular its power density, because the ESR restricts the rates at which the capacitance can be charged or discharged upon application of a given current or voltage. The voltage drop created by cell resistance affects both the charge and discharge capacities of a cell. The non-ideal loss limits the effective region for usable charge storage and thereby limits the charge capacity of the cell. The lost charge is primarily dissipated as heat ($P=I^2R$). The non-ideal resistive power losses can generate an unacceptable amount of heat very quickly. As devices age, degradation sets in, causing an increase in series resistance. Continued device operation at extreme temperatures or high power, lack of proper cooling, or contamination through gas leakage or permeation will increase degradation rates and the ESR will increase, leading to reduced performance and shorter cycle life.

Instabilities in ECs drive resistive losses when energy is stored for longer periods. Diffusion of charge and restructuring of ions in pores (charge imbalances) can both lead to loss of charge while a device has no external connections to its terminals [6]. The magnitude of self discharge or internal leakage current is an important indicator of the quality of a commercial EC. Leakage behavior can be determined by measuring the self-discharge voltage by: (1) charging the device by applying a slow voltage ramp (1 to 50 $mV.s^{-1}$), (2) optionally holding voltage to establish steady state, or (3) switching

the device to open circuit and monitor voltage over time. Variations in discharge based on hold time and charge time allow the determination of any steady state effects and charge rate effects, providing additional insight into the leakage current mechanisms affecting the device.

2.2.2 Surface Area

Increased electrode surface area plays an important role in performance. In supercapacitors, the electrolyte concentration is normally high (>1.0 *M*), causing the diffuse part of the double layer to disappear and the Helmholtz layer to remain. This increases the capacitance of the electrode layer and allows for more charge storage. Furthermore, if the material particle size is larger than the thickness of the Helmholtz layer (<1 nm), conclusions derived from the planar electrode may still be applicable to the situation of particles. To express the capacitance of such a high surface electrode material, a specific capacitance (C_s, expressed in $F.g^{-1}$) is defined as C_m/m. Where C_m is the measured capacitance (F) using the electrode layer constructed from this material and m is the mass of the electrode material (g). Theoretically, we should be able to calculate the specific capacitance of an electrode material according to its mass in the matrix layer, its differential capacitance density, multiplied by the total specific surface area of the carbon particles and divided by mass. In normal conditions, this surface area can be measured by the Brunauer-Emmett-Teller (BET) technique and expressed as *SSA* in square meters per gram ($m^2.g^{-1}$).

Enhanced area allows more electrolyte ions to organize at the electrode surface. Larger pores and channels in the electrode layer increase the accessibility and speed at which ions can organize onto the electrode pores from bulk electrolyte. Area plays a significant role for deciding on the materials for the electrode layers and the electrolyte. The pore structures of materials vary (macroporous >50 nm, mesoporous <50 nm, microporous <2 nm) and the ability to control the type of porous area

available will lead to increased optimization between accessible power and maximum charge storage. Maximizing the amount of surface area provides the greatest number of active sites in the material and improves the performance of the ES. It would seem that the larger the material surface area, the higher the specific capacitance. However, when the specific surface area (SSA) is larger than ~1200 $m^2.g^{-1}$, the specific capacitance of AC will be saturated by further increasing the SSA [7]. Surface area analysis is conducted with gas that can penetrate pores that are too small for ions so large inactive electrode areas may exist. Blocked pores or tightly bound planes prevent ions from organizing at the surface and can be ion resistive due to poor long range order or collapsed channels within the electrode. To prevent blockages, materials are often designed with periodic structures or large macroporous channels. Chemical activation with KOH is another way to increase surface area by unblocking pores and creating new ones in the carbon materials. However, if the macropores are too big, they become macroscopic voids that detract from otherwise usable surface area.

It is not accurate to estimate the specific capacitance of an electrode material based on surface area due to the large scattering of differential capacitance values for carbon porous materials. The reason is the wide variety of carbon types, such as active carbon powders and fabrics, nanotubes, and aerogels. There is even a great distribution of properties within each group. This allows even some low surface area advanced carbon materials to outperform that of high surface area carbon black materials. As an example, it is expected that the calculated specific capacitance value based on BET surface area should be larger than that of the measured value. Another reason for this is that a small portion of the carbon particle area is ineffective in the matrix layer. Thus the utilization of the particle area does not reach 100%. Therefore, although high surface area is beneficial to increasing the theoretical maximum capacitance, in practice efficient storage use of the area also plays a key role in determining the overall capacitance observed.

2.2.3 Pore Structure

In the past, desirable surface area encompassed macroporous structures for the increased flow of ions and mesoporous structures to maximize surface area. The comparably large solvent cage around the ions blocked entrance into the smaller micropores [8], [9]. Recent discoveries by *Chmiola et al*. and *Huang et al*. [10], [11], [12], [13], [14] have shown that this is not entirely true. **Figure 1** shows that as pore size decreases into the sub-5 nm range, capacitance also decreases. The standard parallel plate model (applicable to region IV in **Figure 1**) of capacitance begins to fail below pore sizes of 5 to 10 nm (region III). However, below 1 nm, a large increase in capacitance is observed. Further research reveals that around 1 nm the capacitance exhibits a sharp increase reaching a maximum at the ion size. The increase in capacitance below 1 nm is characterized as the ions shedding their solvent cage, entering the micropore, and contributing to the storage mechanism of the double-layer.

Another important property to consider in EDLCs is pore regularity and distance. In classical electrochemistry, ion transport time has a quadratic link to transport length [15]. Regular pore structures provide reliable short diffusion pathways between storage sites, but pore defects disrupt pore regularity, which increases the pore interspacing and causes ion scattering. Irregular pore spacing and ion scattering detract from ion transport speed and throughput, resulting in fewer accessible ions and lower power. Scattering can also be caused by poor interfacial wetting of the electrode. Depending on the character of the electrolyte solvent, hydrophobic or hydrophilic dopants or functional groups can be applied to the material.

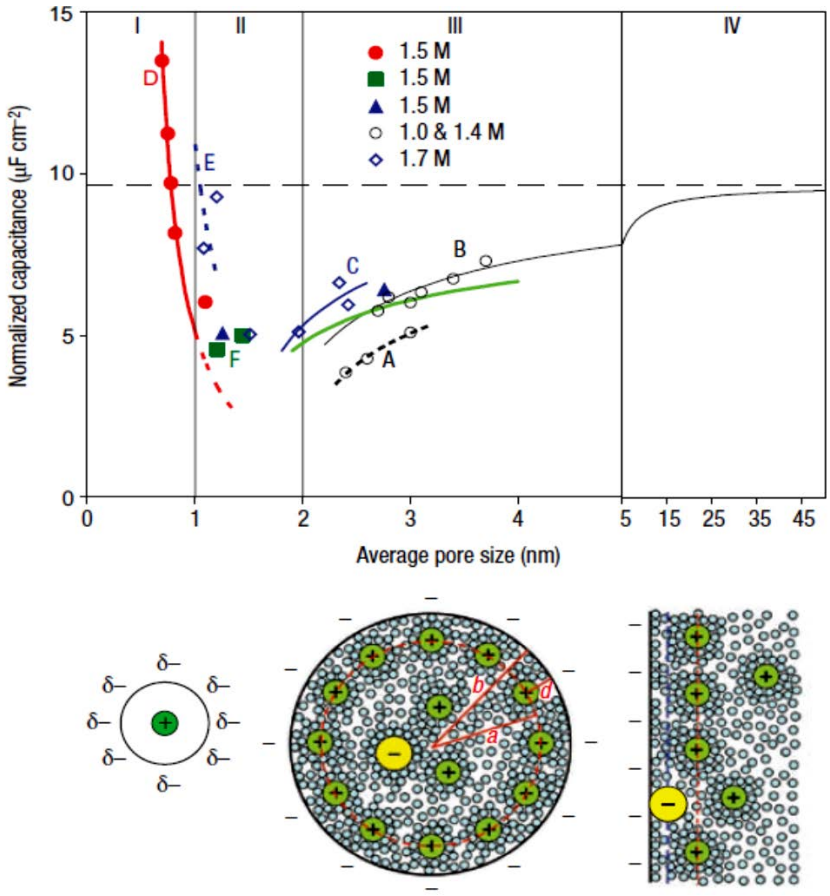

Figure 1: Capacitance tested with various ionics in acetonitrile (TEAMS: 1.7M, $TEABF_4$: 1,1.4,1.5M) for various carbon structures. Templated mesoporous carbon (a, b), activated carbon (c), microporous carbide derived carbon (d, f), and microporous activated carbon (e). The bottom images from right to left illustrate model of planar EDLC with negligible curvature, EDLC with pores of non-negligible curvature, and model single ion wire within cylindrical pore. The models can accurately estimate capacitance in their pore regions. Reproduced with permission from [16]. Copyright: Nature Publishing Group 2008.

2.2.4 Functionalization Effects on EDLCs

Small functional groups on the electrode layer materials, such as carbon particles, improve wetting with the electrolyte and allow increased solvent penetration within small pores of the electrode materials. For example, nitrogen dopants and oxygen functional groups can improve wettability in aqueous systems by altering surface effects [17]. Stable oxygen functional groups on the surface can also introduce reversible pseudocapacitive character in addition to double layer charge storage [17], [18], [19], [20]. Nitrogen can form strong covalent bonds with carbon that can regulate electrical and

chemical properties of carbon because of its comparable size and five valence electrons. These nitrogen dopants can manifest in the form of pyridinic, pyrrolic, and quaternary bonds that contribute a large number of electrons to the delocalized graphitic π network within the carbon structure, and can alter the surface and catalytic properties of the carbon structures.

Pseudocapacitive metal oxide and metal nitride coatings deposited and adsorbed on carbon supports are also effective in increasing the maximum energy density possible for an ES and are discussed in detail later in this chapter. Oxygen dopants such as carboxyl, carbonyl, and hydroxyl groups can improve wetting and open surface area for increased capacitance and higher power. However, an overabundance of oxygen functionalities disrupts the graphitic π-bonding network of the material and reduces conductivity of the material too much. In active carbons, this can occur when activation temperatures and activation reagent concentrations are too high. Graphene oxide (GO), the precursor material of graphene, contains a very large number of oxygen groups introduced by a harsh oxidation reaction from bulk graphite. The precursor material is insulating until it is reduced with a strong reduction technique (sodium borohydride, high temperature, and hydrazine) that aims to remove most of the oxygen functionalities and restore the graphitic plane to create conductive few-layer graphene for use in ESs.

2.3 Carbon Materials for EDLC Supercapacitor

2.3.1 Activated Carbon

Carbons act as excellent conductors, are chemically stable, and have a high surface area, making them the preferred material for double layer electrodes in today's ES's. Carbon however comes in many varieties and not all are applicable to electrode materials. The industrial standard and most

basic high surface area carbon material is known as activated carbon. Activated carbons are widely used because of their moderate cost and easy preparation.

The activated carbon material can be generated from a number of different precursor's materials through carbonization and high temperature annealing in an inert atmosphere. Materials are pitch or resin derived from coal and petroleum which exhibit a liquid phase shift, allowing alignment during graphitization, creating heavily microporous area which requires activation for successful use in ES's. In general, high surface area alone is not easily correlated to capacitance, pore structure seems to be critical. Mesopores are important to allow sufficient ion diffusion kinetics to support high power and area (suggested to be in 20-50 % range) [21]. Meanwhile, surface level micropores allow large area for storage and macropores are important to provide high throughput ion channels on a macroscopic scale.

Alternative carbon precursors are derived from more structured compounds such as wood, polymers and hard shells which do not exhibit a liquid phase during carbonization, maintaining alignment and rigidity. Carbons derived from natural biomass exhibit large voids inherent to the natural structure of the material which can boost transport but can also greatly reduce volumetric performance. Activated carbons in literature can often achieve capacitances as high as 100-200 $F.g^{-1}$ in aqueous electrolyte systems and 50-150 $F.g^{-1}$ in organic mediums [21], [22], [23], [24] [25]. The commercial carbon *Maxsorb* (produced in Kansai, Japan) is made by KOH activation of petroleum coke at 700 ˚C and illustrates over 3100 $m^2.g^{-1}$ [26]. In lab scale three electrode tests, maxsorb carbon was able to produce capacitance in aqueous electrolyte of 225 $F.g^{-1}$ at 1 $A.g^{-1}$ current density, higher than other commercial carbons with much lower area and capacitance. This suggests that BET measurements of surface area are not an effective indicator of capacitance in many cases. In the same test they showed that polymeric activated carbon derived from KOH activation of resorcinol–formaldehyde exhibited

only 1673 $m^2.g^{-1}$ surface area but was able to obtain 325 $F.g^{-1}$ in aqueous electrolyte [27]. Still these powders suffer in cost compared to the more scalable production processing cost of high surface area cloths that exhibit lower performance.

2.3.2 Templated active carbons

As carbon electrode technology moves forward, there is a large array of advanced carbon structures which have higher pore order and increased conductivity. Closed pores produced by the activated carbon process reduce charge rate capabilities and overall storage capacities. Template systems offer to improve this deficiency by creating long range order within carbon structures. The process commonly involves mesoporous silica or zeolite templates [28], [29], [30]. However, the cost of templating currently limits their use towards building a theoretical understanding of the effects of pore size on capacitance and ion kinetics. With improved production methods and lower costs, these methods may become accessible to commercial energy storage applications over time. Zeolite templated carbons exhibit high performance without extensive activation due to the high surface area and long range order of their porous structure. Studies into zeolite X and Y showed performance between 140 F.g-1 to 300 $F.g^{-1}$, with significant performance retention at discharge rates of 2 $A.g^{-1}$ [28], [31], [32], [33]. Mesoporous carbon structures produced by templating with MCM-48 and SBA-15 could produce larger ion conducting channels at lower costs than using rare zeolite minerals (**Figure 2**). The ion channels allow electrolyte to access the microporous area of the precursor carbon and provide enhanced performance versus activated carbons of equal surface area. Templated carbon derived from MCM-48 and SBA-15 created particles with ordered pore size between 2-10nm, realizing performance of 100-180 $F.g^{-1}$ [30], [34], [35], [36].

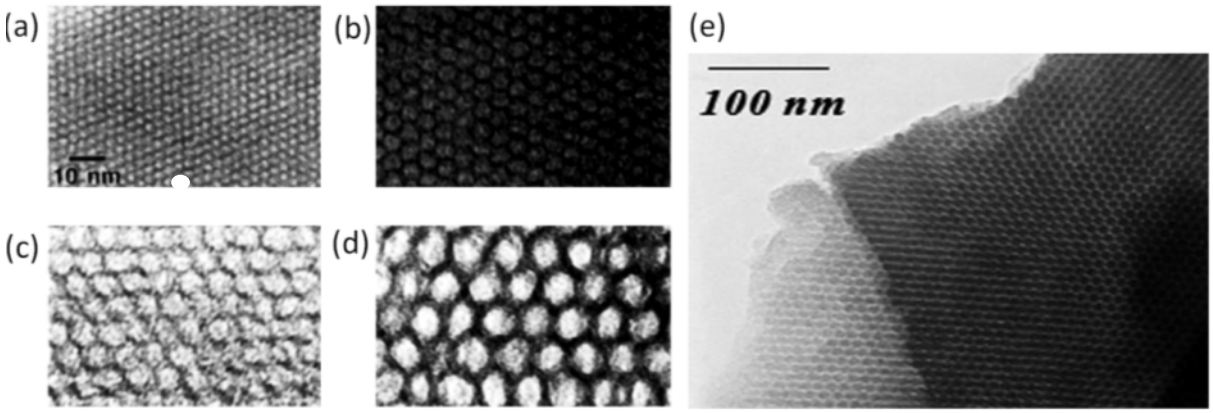

Figure 2: TEM images of MCM-41 (a-d) with pore sizes ranging from 2 nm (a) to 10 nm (d). (e) is a TEM image of carbon prepared from MCM-48 using pitch as the carbon source. Illustrating the highly ordered structure compared. Reproduced with permission from [37] (a-d) and [38] (e). Copyright: American Chemical Society 1992 (a-d) and Elsevier 2005 (e).

Silica nanospheres can also be used to template carbon with interesting results. *Lei et al. p*roduced nanospheres of 2.7 nm, resulting in tight, mesoporous carbon area of 2400 $m^2.g^{-1}$ [39]. The carbon sphere material showed capacitances of 225 $F.g^{-1}$ and 180 $F.g^{-1}$ in aqueous and organic electrolyte, respectively. The capacitance in organic electrolyte showed only a small drop compared to aqueous, leading to a high energy density of 62.8 $Wh.kg^{-1}$ at low power density under 1 $kW.kg^{-1}$. However, the high energy density faded quickly, leading to moderate energy of 9 $Wh.kg^{-1}$ at high power density of 30 $kW.kg^{-1}$ [39]. From this and the results of various micro and mesoporous templates, it is clear that templated carbons are capable of improving upon most AC materials; yet the materials still lack the macropores needed to support higher energy density at high power output. Improving upon this, *Wang et al*. [40] developed the templated highly porous graphitized carbon (HPGC) which showed better capacitance retention (seen in **Figure 3a**) and improved electrode performance at high power. The HPGC material is a composite composed of ordered micro, meso and macropores as illustrated in **Figure 3b**. The composite structure can create short diffusion pathways for the electrolyte to enter the microporous walls and generate high energy density of 22.9 $Wh.kg^{-1}$ in organic electrolyte. Furthermore, the accessibility of the pores allowed the energy density to remain above 20 $Wh.kg^{-1}$,

even for high power rates of 23 $kW.kg^{-1}$. This example demonstrates the promise of EDLC electrodes with refined pore structure for obtaining both high energy and power density.

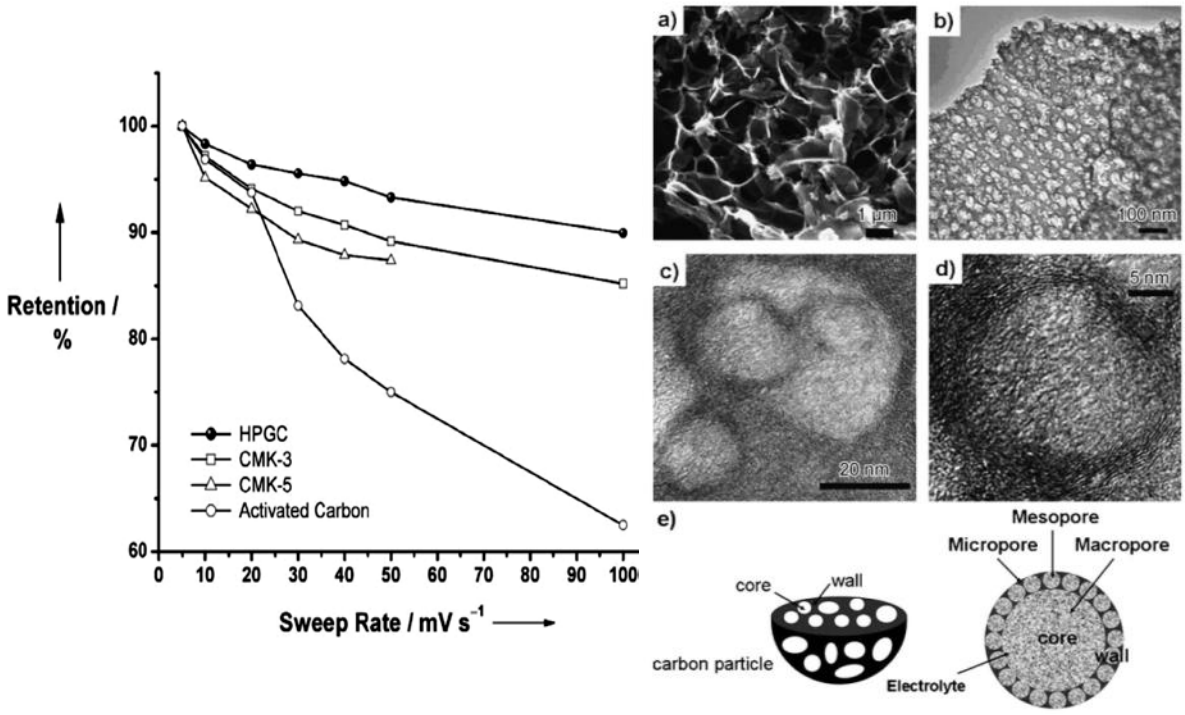

Figure 3: (left) Retention of capacitive performance with increasing sweep rate and power for various carbon materials. a) SEM image of the macroporous cores of HPGC, b) TEM image of the mesoporous walls, c) TEM image showing the micropores, d) TEM image of the localized graphitic mesopore walls and e) schematic representation of the 3D hierarchical structure. Reproduced with permission from [41]. Copyright Wiley-VCH 2008.

2.3.3 Carbon Nanotubes

More advanced carbons are being heavily studied for their potential in controlling structure as well as enhanced properties compared to activated carbon. Carbon nanotubes (CNT) are cylindrical nanostructures which exhibit a near 1-dimensional structure. The cylinders are composed of graphitic carbon walls and exist in the form of single wall (SWCNT) and multiwall nanotubes (MWCNT). The radius of the CNT's is on the order of nanometres, while length can reach millimetre size scales and the graphitic planes in the CNT result in electrically conductive carbon tubes with conductivity as

high as 1000 $S.cm^{-1}$ depending on CNT type [22]. An ordered array or a loosely entangled layer of CNTs has high surface accessibility, leading to high ionic conductivity. The combination of rapid ion diffusion and high electrical conductivity allows for the creation of high power devices compared to AC electrodes. However, the low surface area due to heavily trapped graphitic surface layers (in multi-wall) and CNT bundling often decrease the achieved capacitance and energy density [42], [43].

MWCNT array electrodes produced by *Honda et al.* illustrate the potential of CNTs for high power capacitors [44]. At low current density the MWCNTs exhibited a low capacitance of only 15 $F.g^{-1}$ due to poor surface area. However, the combination of very low electrode equivalent series resistance (ESR) (1.9 Ωcm^2) and high ionic conductivity could enable the MWCNT electrode to retain 12 $F.g^{-1}$ or 2.2 $Wh.kg^{-1}$ for high current density of 200 $A.g^{-1}$, corresponding to power density of 125 $kW.kg^{-1}$. In comparison, when an AC cloth was charged at rates above 10 $A.g^{-1}$, there was a large resistance present, preventing the development of any energy or capacitance on the electrode. Maximum power of the device is calculated to be 3.2 $MW.kg^{-1}$.

CNT's are fabricated by a number of different Alternatively, CVD methodology allows lower operating temperatures and an increased potential for moving to the higher scales required to bring down the high cost of CNTs. All CNT production strategies are expensive due to the high energy processes, extensive purification, scalability issues and CNT size control required for commercialization. Methods include Arc discharge, CVD, High Pressure Carbon Monoxide (HiPco) and Laser Ablation. The high cost and safety issues of CNTs, especially SWNT, is a limiting factor in their adoption into ESs. Further to achieve acceptable surface area, steps must be taken to separate bundles by sonication and through the addition of stabilizers or dispersants [45]. Similar to AC's, electrochemical oxidation with KOH can be performed to increase the surface area and the capacitance of the CNT's [46]. The oxidation increases area by uncapping the nanotubes and

exposing more internal surface area. Too much oxidation or the presence of a large concentration of dispersants can negatively alter CNT performance, so care needs to be taken to optimize the properties. When SWNT are well dispersed capacitance has been shown to reach 100-180 F/g, much higher than that of MWNT [42], [44], [47], [48], [49], [50], [51]. This shows that even SWNTs that exhibit moderate surface area between 200-800 $m^2.g^{-1}$ perform similar to AC materials when gravimetric capacitance is considered. However, the low gravimetric capacitance of CNTs is compensated for by their higher packing density creating volumetric capacitance exceeding that of many AC materials [22]. AC's also suffer degradation of capacitance more rapidly than CNTs at high rates of operation because they exhibit less ionic and electrical conductivity. As a result, CNT's offer superior performance in high power electrodes.

2.3.4 Graphene

Graphene is a new advanced carbon material with unique morphology that distinguishes it from other materials in the EDLC market. Graphite is a highly ordered carbon structure consisting of many tightly stacked graphene sheets which exhibit angstrom level interspacing due to strong *pi-pi* bonding between the basal lattice planes of the graphene **(Figure 4a**). The graphene sheet consists of many carbon atoms arranged into a large 2-dimensional crystal lattice and when separated into fewer layers through the application of some physical or chemical energy (single layer or few layer graphene), the material takes on very different properties from its bulk graphite state [52]. Unlike the one-dimensional nature of carbon nanotubes, graphene is considered much safer due to it microscale dimensions in two dimensions. Pristine single layer graphene is mechanically robust, exhibiting a quantum hall effect at room temperature and undergoing ballistic conduction of charge carriers along the basal planes and resulting in excellent conductivity in the material. The most important properties for the ES market include graphene's ability to reach the high theoretical surface area of 2630 $m^2.g^{-1}$

of its parent graphite and the highly regular pore spacing across the crystal lattice [53]. Due to the atomic thickness, there are also negligible diffusion transport distances resulting in low ionic resistance. The high theoretical surface area of the fully exposed graphene sheets could provide a maximum theoretical capacitance of 550 $F.g^{-1}$ [54].

In practice graphene's surface area is significantly lower than pristine monolayer graphene due to sheets partially restacking and because higher yield production methods can only achieve few/multi layer graphene derivatives. The most common preparation involves oxidizing graphite, to increase lattice spacing and weaken the van der waal forces. Then the insulating few layer graphene sheets can be reduced to regain moderate conductivity around 0.05 $S.cm^{-1}$ -5 $S.cm^{-1}$ and remove the lattice defects [55]. One advantage is that the basal plane acts as a stable site for the reversible oxygen and nitrogen functionalities to store additional charge even with low overall surface area. The high in plane conductivity helps to reduce resistance within the materials and provides power gains similar to those exhibited by CNTs in some cases. *Stoller et al.* were one of the first to utilize chemically reduced graphene (CMG) for ES applications [53], [56], [57]. They produced a CMG graphene which exhibited area of 705 $m^2.g^{-1}$ and capacitances reaching to 107 $F.g^{-1}$ in KOH and 100 $F.g^{-1}$ in acetonitrile using cyclic voltamettry with a 20 $mV.s^{-1}$ scan rate. Many graphene based materials report between 100-200 $F.g^{-1}$, outperforming CNT devices in aqueous electrolyte [58], [59]. Similar to in AC devices, KOH was shown to boost the surface area of TEGO and MEGO graphenes up to 3100 $m^2.g^{-1}$ by restructuring the carbon, exposing hidden graphene sheets and producing extra pores. MEGO powder was weighed and mixed with KOH to undergo a secondary activation reaction (800 ^oC, 400 torr, 1 hour) that increased the surface area significantly and generated a well defined pore distribution dominated by micropores (~0.8 nm) and mesopores (~4 nm). However, in use the device was still only able to achieve 165 $F.g^{-1}$ in organic electrolyte [57]. *D*oping graphene planes with nitrogen can enhance local electronic interactions and improve binding with ions in solution. Plasma

treatment was used to impregnate nitrogen functionalities into defects along the basal plane of the graphene sheets. The performance increase was related to a change in energy band-gap behaviour which increases the quantum capacitance and boosts the available capacitance per unit mass [60]. Further, the presence of nitrogen functionalities could generate cross linking along the graphene plane and create wrinkled graphene sheets with high levels of curvature and performance of 250 $F.g^{-1}$ (at 1 $A.g^{-1}$) in aqueous electrolyte [61].

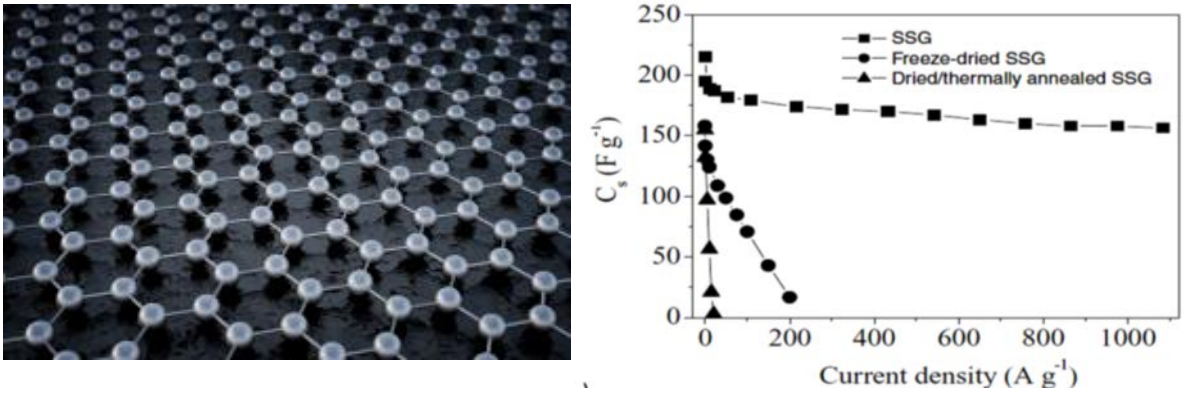

Figure 4: a) Schematic representation of the ideal carbon lattice in graphene. b) Capacitive performance of chemically reduced graphene over a large range of current density for different handling methodology. Reproduced with permission from [62] (a) and [63] (b). Copyright: Nature Publishing Group 2013 (a) and Wiley-VCH 2011 (b).

Yang et al. reinvestigated the source of restacking phenomena in graphene materials which limited device performance [63]. Instead of improving performance by altering the graphene, they drew inspiration from the irreversible damage that could occur when moisture levels dropped to critical levels. They synthesized a solvated graphene film by keeping the active material wet after the reactions as well as in storage. Performance testing, illustrates that the film capacitance can be able to retain 175 $F.g^{-1}$ at a very high current discharge rates above 100 $A.g^{-1}$ in aqueous H_2SO_4 electrolyte (**Figure 4b**). The freeze dried graphene was able to fare better than thermally dried by restricting the forces that caused the tightly bound pores to collapse during thermal drying. But, neither sample

exhibits the same high power high energy performance seen by the wet graphene electrode presented, which is a clear representation of the film design and configuration playing an integral role in the overall performance even with exactly the same material, and in this case film formation technique. As discussed later, formation techniques can also play an integral role in promoting capacitance and high-rate performance.

2.4 Effect of Pseudocapacitance

To further increase energy density and bridge the gap with batteries, more advanced supercapacitors called *pseudocapacitors*, in which the electroactive materials are combined with carbon particles to form composite electrode materials, are being developed. The electrochemical reaction of the electroactive material in a *pseudocapacitor* takes place at the interface between the electrode and electrolyte via adsorption, intercalation, or reduction–oxidation mechanisms (metal oxides and conductive polymers)[64], [65], [66], [67], [68], [69], [70], [71]. In this way, the capacitance of the electrode can be increased significantly. Pseudocapacitive materials increase energy density by storing more than one charge per reactive surface site and also allow storage deeper than the surface, which restricts the storage ($F.cm^{-2}$) of carbon [72], [73], [74]. However, the cost is generally the lower operating voltages of aqueous solution, which counteracts the gains in energy density. The quadratic ($E=0.5CV^2$) energy gains realized by the technologies moving toward higher voltages suggests that improvements to carbon electrode materials could still be competitive with higher capacity pseudocapacitive materials. Further, the cycle durability and rate capabilities of most psuedocapacitor materials still lag behind that of carbon materials.

2.5 Effect of Electrolyte

Commercialized electrolyte materials in carbon devices are dominated by organic electrolytes containing quaternary salts (tetraethylammonium tetrafluoroborate, TEA^+ BF_4^-) because of their moderate ionic conductivities and voltage windows (2-2.7 V) [75]. The most common solvents include acetonitrile and polypropylene carbonate. In comparison aqueous electrolytes have very high ion conductivity rates and are easier to handle than organic electrolytes making them a great candidate for research purposes, but they are unstable at high potential (potential window limited to approximately 1 V). Common aqueous electrolyte solvents used in the development of electrode materials include sulfuric acid (H_2SO_4), potassium hydroxide (KOH), potassium chloride (KCl), and sulfates (K_2SO_4, Na_2SO_4). Attempts to design new and improved electrolyte performance have led to ionic liquids that are capable of high voltage windows, but suffer from low ionic conductivity (3 to 5 V) [76], [77], [78], [79], [80], [81]. Also, attempts to reduce packaging complexity and minimize corrosion and safety problems have led to investigations of gel and solid-state polymers that combine both the separator and the electrolyte into a single component within an ES.

2.6 Summary

In order to reach mass market, supercapacitors need to overcome several large obstacles in order to compete with modern battery technologies. Firstly, the energy density must be increased without compromising existing advantages. Second, the price of the materials used must be decreased through further development. This suggests a new generation of carbon materials is necessary to boost the energy density and maintain or increase existing power density.

From the information presented in this chapter, it is clear that graphene has shown some examples of exceptional high rate performance and has the potential for very high double layer capacitance. Control of carbon surface structure is also shown to have a great effect on capacitive storage which

suggests doping is an important area of development. Further, this information supports the project objectives to develop three dimensional structures that harness a greater percentage of graphenes' potential. After considering the increased capacity for ion conduction and conductive networks, there is also promise to enhance utilization of pseudocapacitance or improve the rate performance of high voltage electrolytes.

Section 3: Three dimensional Graphene

3.1 Introduction

One of the methods being considered to enhance graphene application is the utilization of three dimensional assembly of graphene, which can help improve the surface area and reliability of graphene powders or even be made free-standing. The benefits for the supercapacitor and energy storage field include: higher conductivity due to strong networking, controlled arrangement prevents restacking of basal planes, elimination of inactive conductive carbon mass and binders and in some cases high performance EDLC or composite support materials. This field can be broken down into two main techniques: 1) CVD growth on template materials which are coated with a catalytic metal that can induce the controlled growth of graphene [82], [83], [84], [85], [86], [87] and 2) the self assembly of carbon structures either through the interaction between GO sheets in solution followed by pyrolysis to create ultralight foams or by the shift to hydrophobicity during reduction causing the formation of rigid aerogels [88], [89], [90], [91], [92], [93], [94], [95], [96], [97], [98], [99], [100], [101]. The template methodologies can create highly conductive graphene networks and have shown significant application as conductive pseudocapacitive composite supports, but the multi-layer graphene produced limits the direct EDLC capacitance to only 50-60 $F.g^{-1}$. Further, the high furnace temperatures and sacrificial templates increase costs, similar to the issues observed with template activated carbons.

3.2 Characteristics of Graphene Foam

3.2.1 Drying Techniques

Hydrogels, such as the ones made from graphene oxide dispersions, provide an alternate route for the formation of three dimensional graphene structures with extraordinary surface area and properties[102]. These gels commonly consist of a solid network which interact through physical or chemical bonds that are also capable of trapping many times their weight in water, where hydrophilic groups create strong surface tension. The surface tension within the gel prevents the liquid from flowing and disrupting the bonds. During drying, capillary action caused by the evaporation of water would normally collapse the pore structure. To avoid this, either critical point drying or freeze drying can be used to limit stress on the pore structure, replacing the liquid with gas, forming foam. By this method self-assembled structures composed of hydrogel or strong interactions in frozen solution between the 2D sheets can be preserved resulting in high surface area macroscale foam. The drying process is an integral step for the formation of free standing foams.

Freeze drying, a process used within this study, limits the capillary stress by going around water's triple point boundary, lowering the temperature of water and then going directly from solid to the gas phase via low pressure **(Figure 5).** However, the stress caused by crossing the solid-gas boundary can still disrupt more fragile monolayer/bi-layer structures[103], [104]. Further, water crystallization on freezing must be controlled to prevent sample damage[105], [106]. Critical point drying has the distinct advantage of avoiding any phase boundary by forming a supercritical fluid at elevated temperature and pressure. The critical point of water is at 374 ^{o}C, high enough to damage many foam structures[102]. Instead acetone is often exchanged for water and then acetone is washed away with liquid CO_2 in a high pressure chamber[95], [106], [107]. CO_2 is an excellent supercritical fluid which exhibits its critical point at only 1000 psi and 31 ^{o}C[102]. The pressure in the chamber is slowly released as gas after the temperature is raised above the critical point, leaving the dry sample with minimal distortion of the gelled structure. Freeze drying is used due to its availability, proven scalability within the food industry and because of the lower operating costs and safety factors.

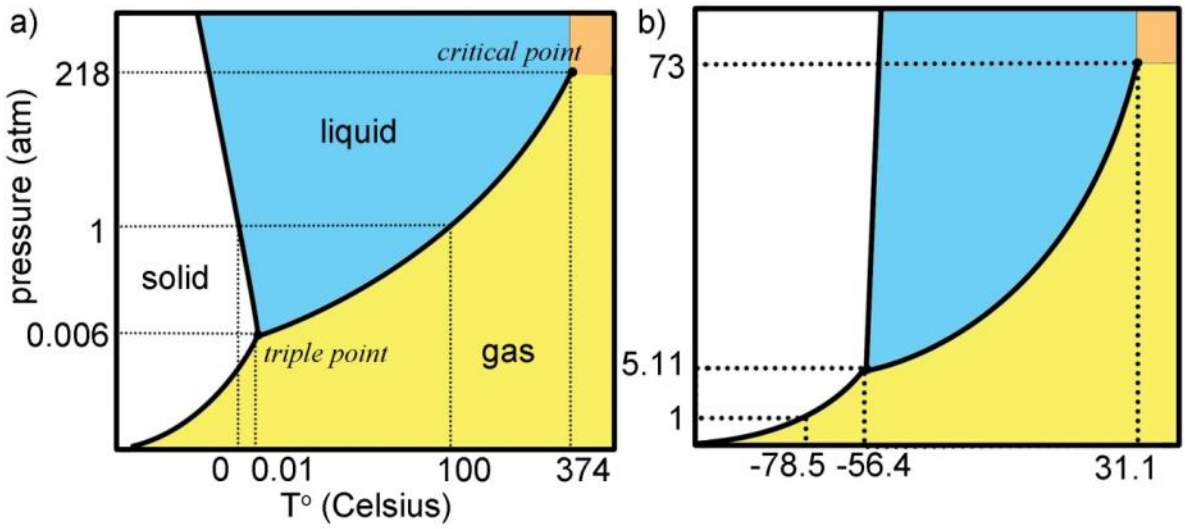

Figure 5: Phase diagrams revealing the triple point boundary as well as the supercritical stage for a) water and b) CO_2. Adapted from [108], [109].

3.2.2 Direct Drying from Graphene Oxide Precursors

Graphene oxide (GO) is currently the most common precursor for the preparation of graphene materials in bulk application. GO is prepared by the intercalation and oxidation of graphite powder, using sulfuric acid and potassium permanganate[53], [110], [111]. The reaction forms a strongly oxidizing species known as dimanganeseheptoxide (Mn_2O_7) [112]. When heated to around 55 ^oC and or placed in contact with graphite, a series of microdetonations occur which functionalize the carbon surface.[112] Functionalities consist of primarily epoxide and hydroxyl groups which are highly hydrophilic and form strong hydrogen bonds with water.[113] Intercalation with water causes lattice expansion, increasing the distance between the graphite planes from 0.335 nm to 0.6-1.2 nm[114]. Then, after strong mixing or weak sonication the van der waal binding forces are easily overcome to form thin mono or few layer graphene oxide materials[115].

The high solubility and hydrophilic edges of graphene oxide compared to pristine graphene allow it to be well dispersed at high concentrations. However, the basal plane retains some of its

hydrophobicity, rendering GO amphiphilic[116], [117]. Even un-gelated solutions between 1-15 $mg.mL^{-1}$ exhibit strong enough bonding interactions that they can be directly freeze dried to form GO foams[118], [119], [120]. However, the grains created from ice crystal formation during rapid solution freezing can cause internal expansion and macroscale cracking of the freeze dried solution[121], [122]. Improving the quality and strength of GO networks will be important to the production of repeatable, scalable foam production. To increase the applicability and harness the desired properties of GO foams they must be reduced to reduced graphene oxide (rGO) foam. However, reintroducing GO to moisture, it disperses and swells, preventing chemical reduction in solution with a reducing agent such as sodium borohydride, hydrazine, ascorbic acid and HI[53], [55], [56], [113], [123], [124], [125]. To increase the range of applications GO foam can be reduced with high temperature (~600-1000 ^{o}C) in a dry argon environment [98], [126]. For best results the ramp rate for temperature needs to be kept low or the foam rapidly releases gas, disrupting the integrity of the foam structure[118], [120], [127], [128].

Higher aspect ratio materials are capable of inhibiting rotational motion within a gel and increasing the number of contact points between sheets. Therefore, larger lateral dimensions of the GO sheets should exhibit increased solution viscosity and increased hydrophobic character. *Bai et al's* investigation into the effect sheet size and solution acidification revealed that GO hydrogels can also be rapidly formed at room temperature, with a low critical gelation concentration of only 3 $mg.mL^{-1}$[129]. Small GO flakes did not form a solid gel, but instead favored the rapid precipitation of flocculated powders even at high concentrations. When flake size was greater than 1 μm, instead of precipitating the restricted rotational motion of the larger sheets and the increased bond strength triggered a nearly 40x increase in viscosity and hydrogels formed within a few seconds. Initial graphite size is not the only factor, sonication has also be shown to induce scission of the GO basal

plane, observed in **Figure 6**.[130] Cross linking polymers and divalent ions applied to GO solutions have also helped to strengthen the intersheet binding [129], [131].

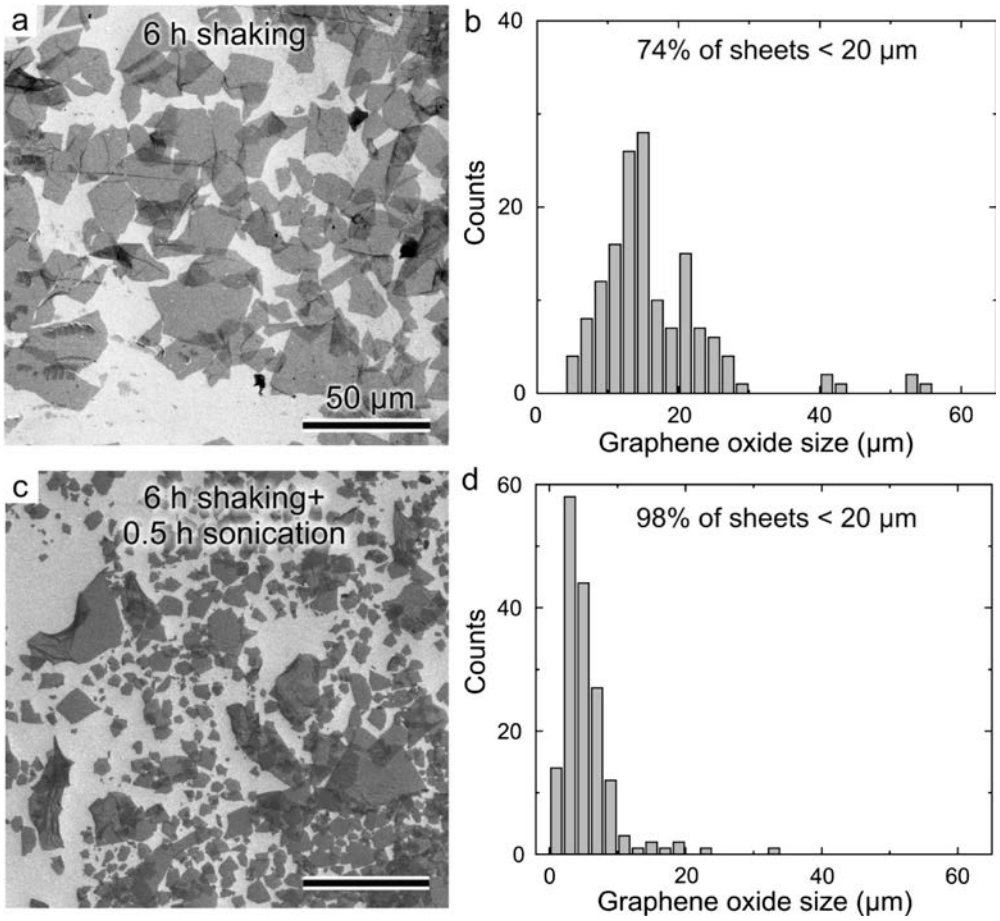

Figure 6: a) SEM image of graphene oxide sheets that underwent 6 h of mechanical shaking. b) Histogram of sheet sizes observed in panel a. c) SEM image of graphene oxide sheets that underwent 6 h of mechanical shaking and 0.5 h of sonication. d) histogram of sheet sizes observed in panel c. All the scale bars are 50 μm. Reproduced with permission from [130]. Copyright 2011 American Chemical Society.

With continuing improvements to graphene foam networks a goal it is possible to produce solid materials that are comparable to or even less dense than air, <1 mg.cm^{-3}. *Sun et al* showed that integrating the beneficial effects of giant GO sheets (GGO) with carbon nanotube (CNT), 4-50 μm size range, which allow for the formation of ultraporous graphene foams down to 0.16 mg.cm^{-3}[132], [133]. However, realizing the process for achieving these large sheets is still difficult and not widely used in other literature. The foams could be achieved with a simple direct solution freeze drying

process, followed by a 90 ^{o}C hydrazine vapor reduction[98], [126]. With the addition of up to 50 wt% CNTs to the GGO solution a highly synergistic effect was observed where the strong van der waal forces between the rGGO and CNTs caused the CNTs to lay flat on the graphene sheets (**Figure 7a,b**) [98], [132]. As a result the flexible reduced GGO (rGGO) network favors load transfer to the strong CNT ribs, creating a compressible foams (0.75-1.5 mg.cm^{-3}) which can recover from 50% strain after more than 1000 cycles (88% stress retention).

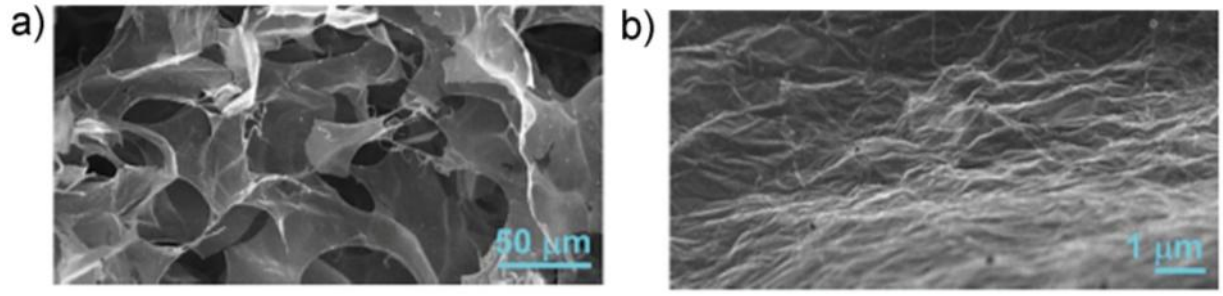

Figure 7: a) SEM image of the CNT/reduced GGO foams (ρ= 1 mg.cm^{-3}, f_{CNT}= 0.5) after 1000 cycles of compression-release and b) CNT distribution on individual graphene sheets at higher magnification. Reproduced with permission from [132]. Copyright: 2013 Wiley.

3.2.3 Self Assembly by GO Reduction

Three dimensional graphene foams have also be generated by utilizing the unique properties of graphene oxide to produce high concentration solutions and gels. During the initial stages of low temperature thermal reduction the basal plane of graphene oxide shifts from a hydrophilic state to a more hydrophobic regime. Hydrogen bonding with water is weakened and the van der waal attraction between the planes increases, creating sticky graphene sheets, which if undisturbed self assemble, as illustrated by *Qui et al* in **Figure 8a**[105], [119]. Conversely, **Figure 8c** reveals when concentration is insufficient, porous precipitates form and settle out of solution[94]. However, if the concentration is high enough the attractive forces between sheets and the mutual restriction of mobility cause the slightly reduced graphene materials to assemble into a porous hydrogel, taking on the shape of the

containment vessel[134]. Reduced further, the C/O ratio of the network increases, the van der waal forces become stronger and the self assembled rGO hydrogel becomes more dense (**Figure 8d**). After assembly, the structure can be dried to prepare foam or applied in the wet hydrogel form. The main benefit of this approach is higher strength and in some applications the higher density of the foams, while still achieving very high surface area and thin pore walls **(Figure 8b)**. Various methods for graphene foams formed by reduction self assembly can be found in the literature using high pressure and high temperature in autoclaves or low temperature variations[94], [97], [105], [106], [107], [135]. The reduction can also be performed with the addition of crosslinking agents or more environmentally friendly reducing agents and the reduction process can be further supplemented with high temperature annealing.

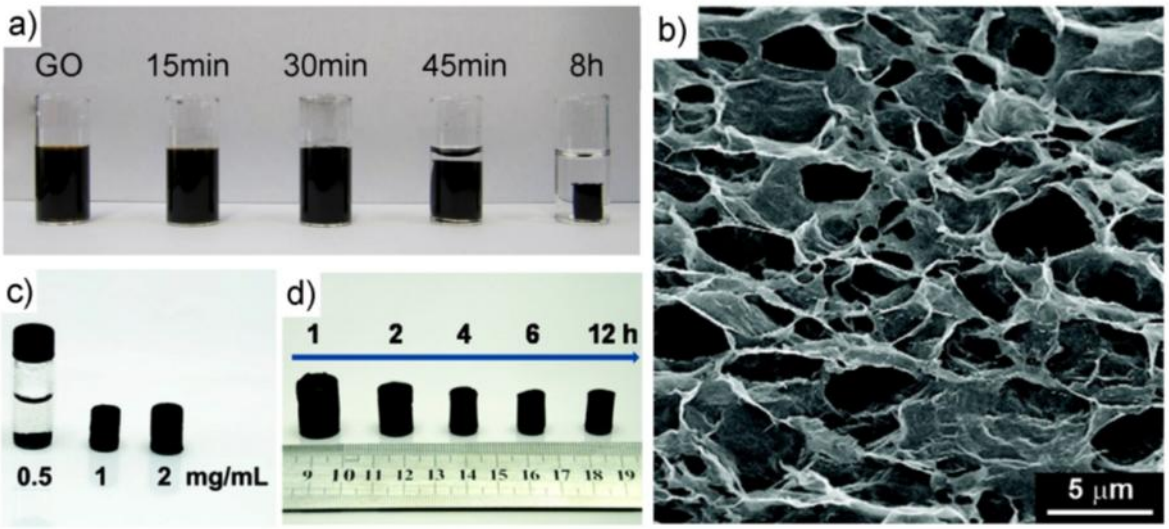

Figure 8: a) Photos of GO dispersions after being subjected to ascorbic acid reduction at 100 °C for different periods of time. b) SEM image of a typical self assembled 2 mg.mL^{-1} rGO foam formed with 180^{o}C in autoclave. c) Image depicts that the GO concentration must be above a critical point before self assembly will occur and that d) after a network is formed it will continue to tighten and become denser with reduction. Reproduced with permission from [105] (a) and [94](b-d). Copyright: 2012 Nature Publishing Group (a) and 2010 American Chemical Society (b-d).

Crosslinkers have also been employed to improve the sheet interactions and or to functionalize the graphene surfaces prepared with high temperature and pressure in an autoclave. In one example, pyrrole was able to interact with the GO sheets through hydrogen and pi-pi bonding to reduce self stacking of the GO during reduction, while still promoting binding between rGO [96], [97]. Thiourea has also been shown as a crosslinker additive which when heated decomposes to form ammonia and hydrogen sulfide gases which in small quantities leaven the hydrogel, creating larger pores and doped the basal plane with crosslinking $–NH_2$ and $–SO_3H$ groups as it was reduced[134]. It should be noted that the carbon to oxygen (C/O) ratio of the self assembled rGO foams reduced through temperature and pressure alone is significantly less than that of graphene powders reduced through hydrazine (C/O~10.3)[55] and $NaBH_4$ (C/O~8.6) [123]. But, the rapid gas release during aggressive reduction in these aqueous mediums limits the self assembly behaviour during the reduction of GO solutions prepared by these methods. Instead the reduction can be accomplished by low rate heating to pyrolyze the assembled aerogels and achieve greatly improved conductivity[106], [107]. Differences in the GO precursor are likely to create variation in the results achieved between one report and another. However, the low processing temperatures resulted in less aggressive restacking/assembly, which after critical point drying produced rGO foams with 1200 $m^2.g^{-1}$ surface area.

In addition to controlled high temperature reduction, covalent cross linkers have also been used to demonstrate improved rGO foam strength and conductivity by increasing binding strength, flexibility and controlling intersheet spacing more efficiently than physical interactions alone. *Gogotsi et al* presented a low density, compression tolerant foam using ethylenediamine (EDA), a short carbon chain capped with amine groups, to covalently crosslink GO's structure[135]. During 95 ^oC reduction the FTIR band corresponding to epoxy groups on the GO surface weakens, replaced by $–CH_2$ and -NH groups, suggesting a ring opening reaction is occurring on the epoxide groups, leaving EDA covalently bound to the GO surface (**Figure 9a**) [135], [136]. In addition to the mild thermal

reduction at 95 ^{o}C, EDA is capable of acting as a mild reducing agent, removing hydroxyl functionalities from the GO surface. The EDA promotes covalent linkages between multiple GO sheets, while hydrogen bonds between amine functionalities further promote intersheet binding and yet the functionalities minimized restacking, thereby eliminating the XRD diffraction peaks normally seen for GO and rGO materials (**Figure 9c**). The achieved foam was only mildly reduced (C/O~2.3). before the functionalized graphene foams (FGA) were fully reduced by microwave irradiation, removing the remaining oxygen and creating ultralight foams (ULGA, 3 mg.cm^{-3}) with excellent compressibility at up to 90% strain (**Figure 9d**). In a separate report rGO hydrogels which used EDA as a covalent cross-linker still prevented restacking at high concentrations up to 15 mg.mL^{-1} when formed at 90^{o}C [101]. This was confirmed by XPS results indicating that nearly all the nitrogen exists in the C-NH-C form, indicating that EDA is covalently bound to graphene.

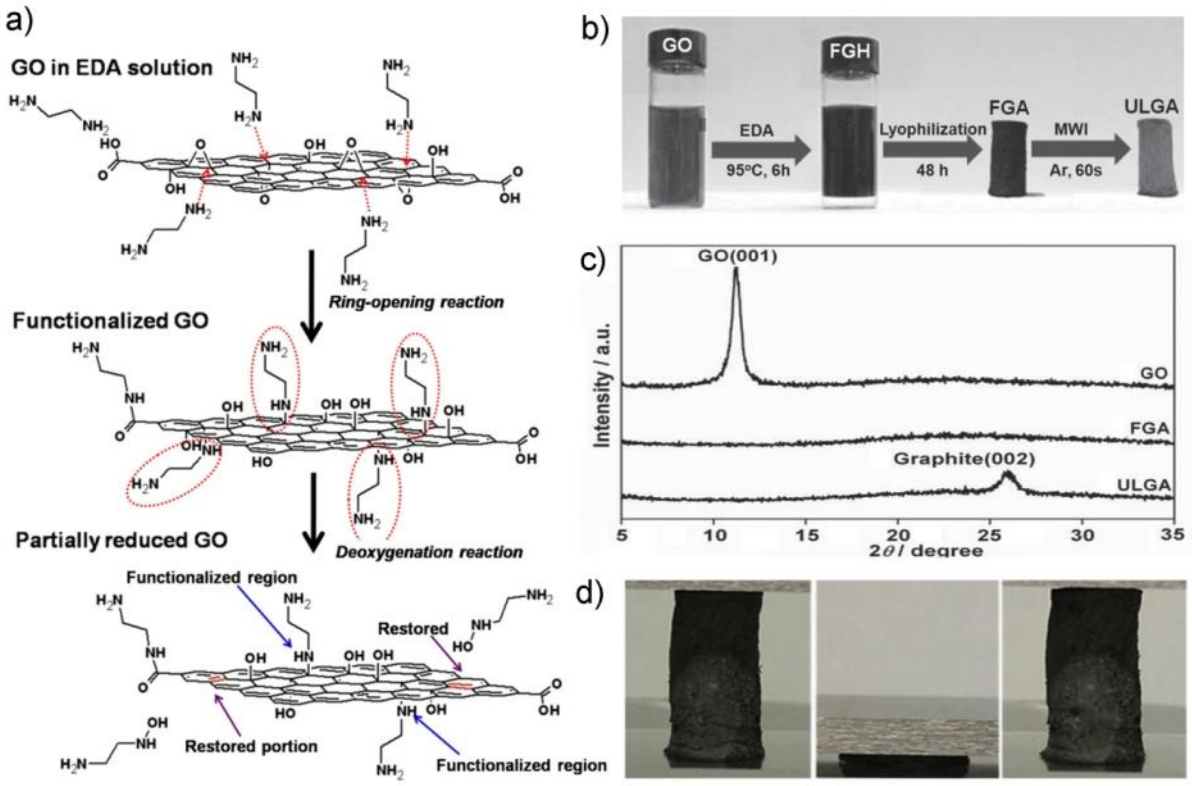

Figure 9: a) Schematic illustration of mechanism of EDA-mediated functionalization and reduction of GO, the restored sp^2 regions are marked with red line. b) Illustration of different steps in the fabrication process of the ultralight graphene foam (ULGA). c) XRD patterns and of GO, FGA and ULGA. d) the digital images showing compressibility of ULGA. Reproduced with permission from [135]. Copyright 2013 Wiley.

If graphene foams are desired without high temperature annealing, such as the desire in this thesis, effective reducing agents are necessary to achieve high conductivity rGO foams. However, the strong reducing properties of the most common agent's, hydrazine and $NaBH_4$, generate large quantities of gas capable of breaking apart the forming hydrogels during their critical state of reduction. Further, hydrazine has high toxicity and $NaBH_4$ has strong reactivity with water. Ascorbic acid (AA), also known as "Vitamin C" is an edible, non-toxic mild reducing agent that *Fernanadez-Merino et al* have shown to be an effective substitute for reducing graphene oxide, reducing GO as efficiently as hydrazine (AA, C/O~12.5) [95], [105], [124]. The proposed reaction mechanism involves gradual hydride transfer from the AA molecule to the epoxide or hydroxyl groups on GO, releasing primarily water upon heating, as opposed to gases produced by other reduction methods. In addition, the gradual reduction allows for the tuning of the C/O ratio. These steps towards more environmentally friendly, low temperature processing with controlled porosity suggest a wide range of application and utility.

3.3 Graphene Foams in Supercapacitor literature

The chemical stability, large surface area and high conductivity make graphene a natural competitor for the future of electrochemical double layer capacitors. Restacking prevents utilization of 2D graphene powders full 2600 $m^2.g^{-1}$ surface area and there is still room for improvement [54], [137]. Assembly of graphene into porous three dimensional systems has the potential to enhance surface area, boost network conductivity, and create large macropore channels to better facilitate ionic transport in electrolyte. More importantly free standing networks can also reduce inactive electrode

mass originating from polymer binders, conductive additives and current collectors. This simplified electrode production is important to the reasoning for direct growth onto current collectors or self-supported 3D graphene, discussed in this thesis. With optimized processing the rate performance and capacitance of graphene aergoels can also compete with their two dimensional graphene counterparts [94][100][97][87]. Nitrogen doped graphene foam has also been used by *Zhao et al* to report one of the highest capacitive performances of any carbon materials to date[96], [98]. Pyrrole monomer, a carbon ring which contains a secondary amine group, was added to an autoclaved GO reduction to form pi-pi and hydrogen bonding with graphene oxide during reduction and freeze drying. The pyrrole effectively prevents restacking during reduction and introduces a nitrogen source into the initial foam structure. The foams were then annealed at 1050 ^{o}C, burning away the pyrrole, leaving a highly conductive (1.2 S.cm^{-1}), nitrogen doped graphene foam (**Figure 10ab**). Nitrogen has been shown to modify the electronic structure of pristine graphene leading to increased quantum capacitance[60]. It follows then that the performance of the high surface area foam pressed onto a collector plate could reach 484 F.g^{-1} at 1 A.g^{-1}, close to the theoretical maximum for graphene. More importantly, the conductive heteratom doped structure retained 400 F.g^{-1} at a high discharge rate of 100 A.g^{-1} for over 1000 cycles with negligible loss in performance (**Figure 10c**).[98][96] The high temperature is process limiting and the size scale used was small, however the high performance highlights potential for continued work into 3D foams.

Aqueous electrolytes hold several advantages such as high ion mobility and lower toxicity compared to organic electrolytes used in commercial electrochemical double layer capacitors (EDLC). However, the low voltage breakdown of aqueous cells limits the energy density. This has been mitigated by implementing nanostructured metal oxides with fast redox reactions and specific capacitance much higher than double layer charge storage on carbon [64], [66], [68], [69], [74], [138], [139], [140]. Further, metal oxides are more dense, leading to higher volumetric performance.

But, the conductivity of these materials is low, which limits the utilization at the discharge rates required for practical supercapacitive applications. By using 3D graphene as a high surface area conductive support it may be possible to achieve yet higher performance. However, the high conductivity of CVD-G foams appears necessary to realize the high capacitance of the metal oxides (up to 1100 $F.g^{-1}$) [85], [86], [140], [141], [142]. The high conductivity of the graphene network allows for effective utilization of the pseudocapacitive material even at high rates, increasing high power retention and making the cycle life more competitive with EDLC devices. **Table 1** reviews the composite performance of several nanostructured metal oxides grown on CVD-G foam materials. Various morphologies of the deposited metal oxides can be seen in **Figure 10d-f**. Similar rate enhancement could also be expected for other metal oxides such as RuO_2/2D-G composite powders which have displayed high 570 $F.g^{-1}$ capacitance at low 0.1 $A.g^{-1}$ rates.[143]

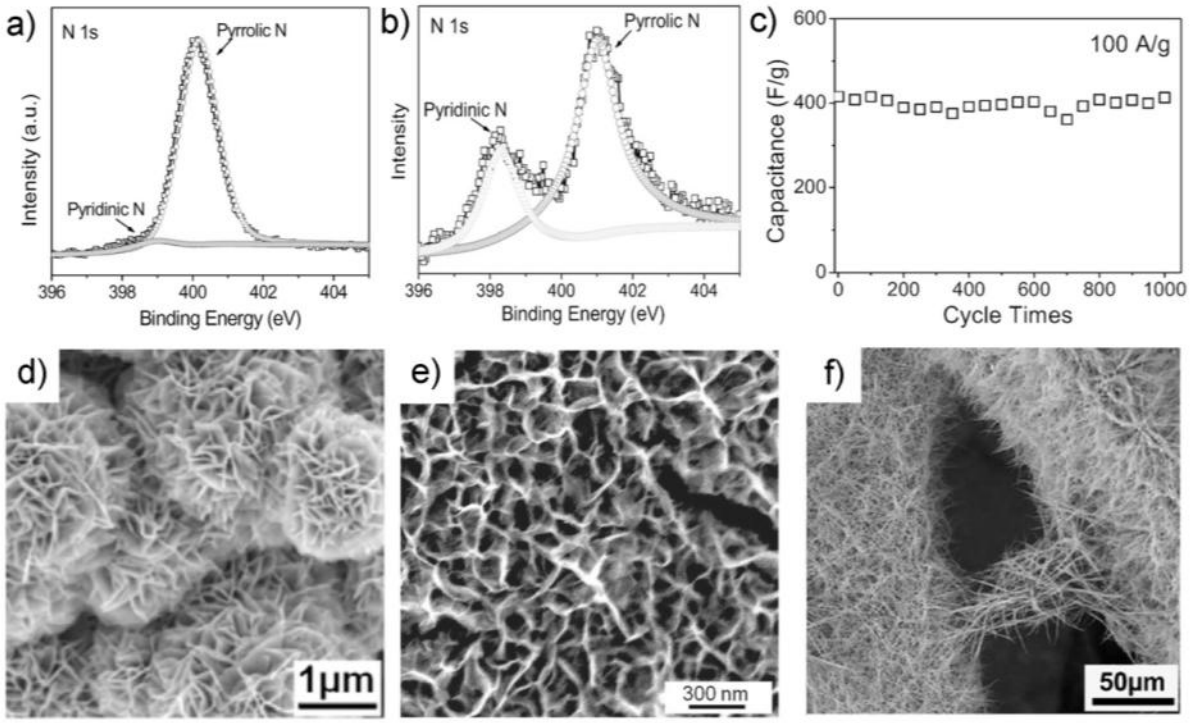

Figure 10: High resolution XPS spectrum for the N1s peak of the a) freeze-dried N-containing foam by hydrothermal treatment of a GO dispersion mixed with 5 vol% Py and b) the shift to pyrridinic N in the 1050 ^{o}C annealed foam. c) 1000 cycle stability of the N-doped foam at a high rate of 100 $A.g^{-1}$. High resolution SEM of

well anchored pseudocapacitive CVD-G foam electrodes coated with d) MnO_2, e) NiO and f) Co_3O_4. Reproduced with permission from [98](a-c), [85](d), [86](e)and [142](f). Copyright: 2012 Wiley (a-c), 2012 Elsevier (d), 2011 Wiley (e), and 2012 American Chemical Society (f).

Table 1: Pseudocapacitive performance of CVD-Graphene foams coated with various metal oxide surface coatings.

Metal Oxide	Demonstrated Morphology	Voltage Range (V)	Discharge Rate	Capacitance (F/g)	Stability (1000 cycles)	References
ZnO	Nanorods	0.4V	5-50 mV/s 6.7-33 A/g	210-400	6.7A/g Negligible losses	[141]
MnO_2	Nanoflower,	1V	0.2-1.2 A/g	250-550	0.2 A/g 21% loss	[85]
	Nanoparticle	1V	0-100 mV/s	100-475	~2 A/g 8% loss	[140]
Co_3O_4	Nanowire	0.5V	10-100 mV/s 10-30 A/g	456-1100	10 A/g Negligible losses	[142]
NiO	Nanoparticle	0.5V	5-40 mV/s 1-20 A/g	573-816	80 mV/s Negligible losses	[86]

3.4 Summary

This review of graphene foam establishes several important concepts which affect the approach used within this project. Firstly, CVD grown graphene foam has high conductivity making it an excellent support material for pseudocapacitance, but it exhibits poor performance for double layer storage. The methodology also involves high temperature CVD treatments which do not follow the low temperature scheme, and the pore sizes are unnecessarily large for double layer application.

Other methodologies involving self assembly and direct freeze drying of graphene are able to produce more uniform growth over a large area with tighter pore structure, where the sheet size of GO plays a major role and self-assembly lends itself more closely to low temperature processing. Further, structure is more variable by this methodology, leaving room for improvement and continued development compared to the CVD template approach. The shift in character between hydrophilic to hydrophobic states during reduction enables a tightly packed network which can be tuned to control performance. In addition, ascorbic acid newly realized as an efficient reducing agent for graphene

oxide, can operate at very low temperatures. Lastly, controlling sheet interaction during the hydrophobic shift by utilizing cross linking or pH control to reduce sheet restacking, has been shown to provide further control of pore structure. Increased understanding of GO self assembly plays an important role in developing the process used within section 6 of this project.

Section 4: Characterization

4.1 Introduction

This chapter is dedicated toward providing background on the important characterization tools and testing protocols used to analyze the synthesized materials in this project and in the background information provided. Without a thorough understanding of the technical background related to the research area, it is more difficult to determine the success of this project.

In order to develop an understanding of materials composition and structural properties a suite of tests can help develop important knowledge required to direct future studies. The characterization techniques used for the work in this thesis and understanding its background are detailed in this section. They relevant techniques include: scanning electron microscopy (SEM) in addition to optional energy dispersive X-ray (EDX) imaging, transmission electron microscopy (TEM), X-ray powder diffraction (XRD) and X-ray photoelectron spectroscopy (XPS).

The most common electrochemical tests used for supercapacitor testing are identified as cyclic voltammetry, charge discharge potentiometry and electrochemical impedance spectroscopy. These tests are also used to determine capacitance, identify cycle life and determine resistive characteristics. Configuration of the electrochemical test cell can also be an important factor in determining, as well as, it can become a variable in performance estimation. This section describes the individual tests and the fundamental equations that govern the trends observed, allowing for better understanding of the tests enable stronger comprehension of the results in sections 5 and 6.

4.2 Physical and Electrochemical Characterization Techniques

4.2.1 Scanning Electron Microscopy (SEM)/ Energy Dispersive X-ray (EDX)

SEM is one of the most common and reliable techniques used for analyzing the composition and topography of solid materials. SEM is capable of achieving magnification many times that of optical microscopes which rely of the relatively large wavelength of photons by using a focused beam of electrons under high vacuum. This enables scientists and engineers around the globe to unveil the morphology and structure of a large variety of materials at a micro and nanoscale great detail. A high voltage electron gun fires a beam of electrons, which is then focused by a series of magnetic fields (condenser lenses), apertures which filter out high angle electrons and the adjustable objective lenses magnetic field refocuses and directs the beam to the sample position [144], [145], [146]. During imaging, the beam is rastered across the sample surface and the electrons interact with the surface, these interactions are collected by specifically designed electron detectors and then the information is fed back to a computer to digitize the image. To prevent electrons absorbing and charging the sample must be conductive and well grounded, the electrostatic signals can significant affect the detectors signal output. If these conditions are met when the emitted high energy electrons bombard the sample a number of different interactions can occur displayed in **Figure 11**. The topographical information down to only a few nanometers is determined from the secondary electrons ejected from atomic orbitals only a few nanometers from the sample surface which are picked up by the off angle secondary electron detector for optimal topographical information or by an in-lens detector for greater contrast. Back-scattered electrons are elastically scattered back to the surface and are collected directly above the sample and gives information relating to the distribution of atomic weight throughout a sample.

Further atomic information can be gathered by analyzing the characteristic x-rays that are emitted when the electron beam removes an inner shell electron causing a higher energy electron in the atom to fill the shell and release an x-ray with a specific energy level. The penetrating x-rays then return to a detector and the energy levels correspond to specific atomic energy of various elements. This process is known as energy dispersive x-ray analysis and by matching the atomic transition peaks to the intensity vs. energy spectrum we can gather information about the atomic distribution for a single spot on the sample or map the distribution over a greater area.

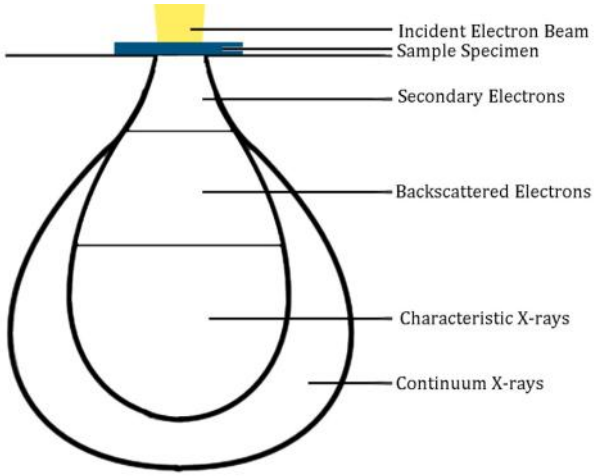

Figure 11: Signals generated by interaction of electron beam and specimen and regions from which each signal type can be detected.

4.2.2 Transmission Electron Microscopy (TEM)

TEM is similar to SEM in many ways, utilizing a focused electron beams interaction with a sample. However, TEM concerns ultrathin samples which allows the transmission of electrons through the sample [147]. The transmitted image is then passed through another series of magnetic objective and projector lens which magnify and project the image onto a fluorescent screen which is imaged by a high resolution camera. The high resolution is due to the extremely short de Broglie wavelength of an

electron which allows imaging down to only a few nanometers. This allows us to study the crystallographic structure and pore structure, determining the number of layers present in graphene or other materials.

4.2.3 X-ray Powder Diffraction (XRD)

In XRD a beam of high energy electrons strikes a metal plate, often copper, generating X-rays. The X-rays are filtered through a slit which causes the X-ray beam to hit the powder samples at a specific angle, which changes as the x-ray arm changes position throughout the test. The X-rays then interact with the sample, elastically scattering toward the photographic film used to count the X-rays [148], [149], [150], [151]. Some of the rays will interact with the surface atom, while some will miss the surface atoms, and pass through to impact the atoms behind it in the crystal lattice. The X-rays are used to then determine information about the lattice spacing of the material because based on bragg's law, the rays will destructively interfere in all cases except where the angles of the generated x-rays are the same as the incident angle.

$$n\lambda = 2d \sin\theta \qquad \textbf{Equation 1}$$

Where n is an integer, λ is the incident wave, d is the crystal spacing between planes in the atomic lattice and θ angle between the incident ray and the scattering plane. Therefore a set angle with interact strongly with a crystal with a specific *d*-spacing and the constructive interference will create an intensity peak at a specific angle (bragg angle). Depending on the materials crystal structure the peak will correspond to interaction with a specific lattice plane. Further, scherrer equation can also be used to determine information about the crystallite size [152].

$$L_c = A\lambda \,/\, (B\cos\theta) \qquad \textbf{Equation 2}$$

where A is the shape factor (~ 0.9); λ is the X-ray wavelength; θ the Bragg angle; B is the full width at half maximum (FWHM) of the peak in radians. In practice the spectrum of angles versus intensity can be compared against reference card database based on the crystallographic information of many materials in order to find a match. Here we use XRD to study the crystallinity of carbon and identify the presence of graphene.

4.2.4 X-Ray Photoelectron Spectroscopy (XPS)

XPS is a quantitative elemental analysis technique that measures elemental composition and the bond states of interacting atoms. In operation a high energy X-ray beam knocks off electrons from the sample which are collected and measured [153], [154]. The XPS spectra is a intensity peak count of the binding energy, which is the incident X-ray hitting the sample minus the variable energy of the captured electrons [155]. Each element has a different energy and within that at high resolution a set of characteristic binding energies corresponds to the specific electron states within the atom and help determine the specific bond energy with a neighboring element. This technique is a very effective way to determine the elemental composition of a material, as long as the atomic number is greater than 3, and to determine the type of functionalities present on a material surface. In the case of this thesis, XPS can be used to determine the binding type and functionality on graphene and other carbon structures.

4.2.5 Raman Spectroscopy (RS)

RS is based on the inelastic scattering of a monochromatic light source hitting a sample. In a typical system a compound microscope is used to position the sample and align the position of the light

source, and then the sample chamber is closed and placed under darkness so the only light source is the monochromatic beam [156], [157]. The photons are absorbed by the sample materials and can often re-emit at different wavelengths due to the different vibrational, bending or rotational states of the molecules. A filter removes the elastically scattered light which remains at the incident energy level. The information can be used to determine characteristic information about the sample with reference to its atoms binding types and can be used to identify materials based on a fingerprint spectrum. Specific to carbons raman is helpful for determining the graphitic character compared to the defect level of the graphitic compounds and also for determining thickness [158].

4.3 Electrochemical Characterization Techniques

In developing electrochemical capacitors the most necessary characterization is that of performance evaluation. This can be done in a number of ways including the most common cyclic voltammetry (CV) and charge discharge (CD). Another important performance indicator is electrochemical impedance spectroscopy (EIS) which can also gather capacitive information in addition to resistive information of the materials being tested. These tests can be performed either in either a three electrode system which derives information about the cycling behavior of the material, from a single active electrode, in addition to a counter current and reference voltage electrodes. Alternatively, a two electrode design can be used to describe the overall performance of a full cell with active electrodes on both sides of a separator (see **Figure 12**).

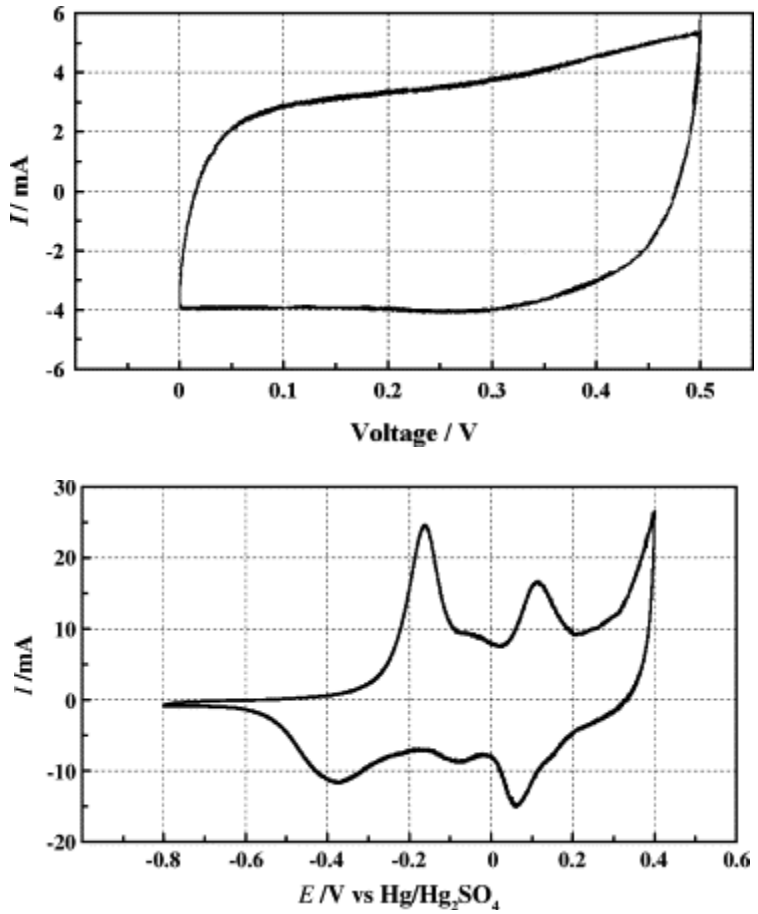

Figure 12: a) CV of PANI/MWNT electrodes using two-electrode cell (2mV/s, 10.4mg per electrode) and b) using three-electrode cell (5.4mg active mass, 2mV/s). The images highlight that electrode behaviour can be imaged by a three electrode system, but two electrodes provides a smoothed curve. Reproduced with permission from [159]. Copyright Elsevier 2006.

4.2.1 Half Cell Design

On the lab scale, for ease of testing most performance characteristics are investigated using aqueous solvents in a three electrode system. This electrode design is composed of three main components in addition to electrolyte: 1) the working potential and current are measured at a stable metal or glassy carbon coated with the active materials being analyzed, which develops a double layer capacitance. Opposed to the active electrode are 2) the current measured at a Pt counter electrode which is a catalyst to oxygen and hydrogen evolution as well as a strong conductor and 3) the potential measured at the reference electrode. The reference electrodes potential, commonly a calomel

electrode (SCE)(0.244V vs standard hydrogen potential), is fixed to a specified level based on a controlled reaction within the electrode. The stable reference voltage and free flowing counter current enable the detailed analysis of reactions occurring on the active electrode material. Before testing N_2 gas is used to purge the dissolved oxygen in the cell which can help avoid potential oxygen evolution issues in the cell during cycling.

To prepare small working electrode layers, a quantifiable amount of electrode material is mixed with a conductive carbon additive and a binder material (10-20%) and mixed to form an ink with concentration between 0.5-2 mg/mL. The ink is well dispersed before pipetting a small quantity between 10-80 ug on the electrode. Best practices for testing suggest a larger amount of mass be used which provides a greater degree of accuracy and better states the performance of the materials when considering resistive losses that would exist in industrial electrode slurry coatings [160]. However, for screening and determining active material characteristics this technique still remains popular. For larger scale testing, milligram or greater quantity of material is deposited onto a metal surface via slurry before drying and pressing the electrode. In this case electrode preparation can be as important as material characteristic and can greatly affect the performance outcome of a practical capacitive electrode design.

4.2.2 Full Cell Design

In a symmetric cell both porous electrodes are identical and are charged by an external power supply to hold opposite charges, one negative and the other positive (**Figure 13**). The electrode's active layers are made from active particles that are compacted together through a binder and two pressed current collectors. A separator between the two electrodes is made of a porous electrically insulated material used to prevent contact and short circuiting and also provide pathways for electrolyte ions.

The electrode layers and the porous separator are filled with or soaked in an electrolyte solution, with the electrolyte normally being composed of 2M potassium hydroxide, sodium/potassium sulfate or sulfuric acid.

An important aspect to consider is that a double-layer is established at each electrode and contains the Helmholtz and diffusion layers along the carbon particle-electrolyte solution interface. The electrodes are connected in series across the circuit and therefore the overall capacitance of a supercapacitor can be treated as two capacitances connected in series. Therefore the capacitance (F) for the active material in a symmetric full cell can be expressed as half that of the single electrode. In an asymmetric supercapacitor, the electrode with the smaller capacitance will dominate the total capacitance. Further to determine the specific capacitance the value for each must be divided by the active mass in the electrode cell which is two times greater in the full cell. Therefore the calculated specific capacitance of a symmetric full cell will be theoretically equivalent to four times that of the half cell value.

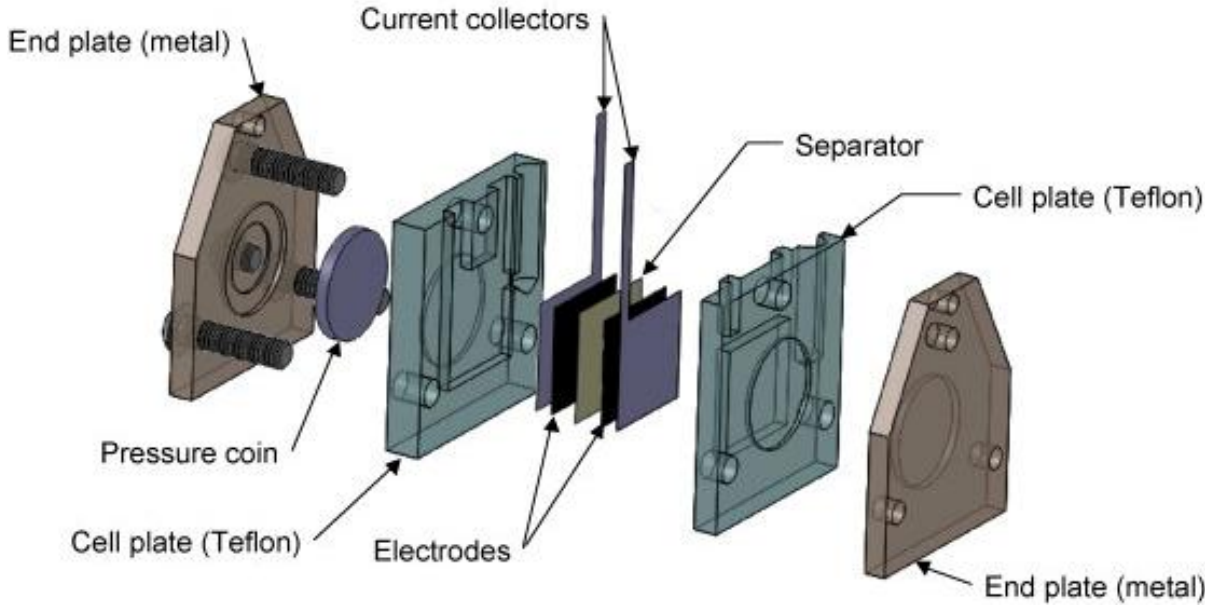

Figure 13: Schematic illustration of the two-electrode supercapacitor test cell. Reproduced with permission [161]. Copyright: Elsevier 2012.

4.2.3 Cyclic Voltammetry

Cyclic Voltammetry (CV) is a common screening technique for capacitor materials that swiftly cycles from a neutral open circuit potential, charges up to a predetermined high voltage (ex . 1 V) and then discharges down to a low voltage (ex. 0 V). Measured is the output current due to the charging and the area beneath the curve can be used to calculate the capacitance. Capacitance stored on a charge is based on the derivation [72]:

$$Cs = \frac{\Delta q}{m*\Delta V} = (m * \Delta V)^{-1} \int idt = (m * \Delta V)^{-1} \int idV * \frac{dt}{dV} \qquad \textbf{Equation 3}$$

Here m is the mass of the active material on the electrode, V is the voltage, $\frac{dt}{dV}$ is the predetermined voltage scan rate inverted, and the integral is the charge area. However to account for non-ideality between the charge and discharge the enclosed area of the CV curve is divided by two. Using commercial activated carbon as an example the non-ideal shape of the charge becomes worse as the resistive components become more prominent at high scan rates (**Figure 14**). This material has been mixed with sufficient highly conductive carbon (15%) to ensure retained performance at up to 100 $mV.s^{-1}$, a discharge time of only 10s in an aqueous capacitor. However, at high rates the curve begins to develop a resistive slope which results in lowered capacitance a normal resistive issue for any capacitive material.

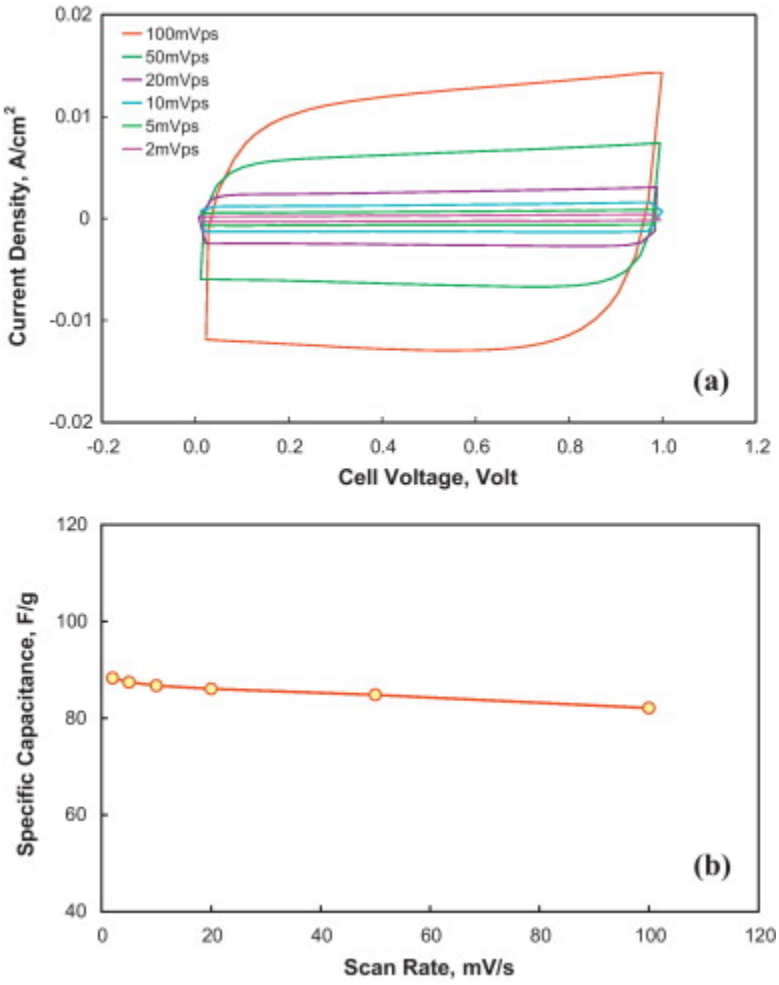

Figure 14:(a) Cyclic voltammograms, recorded at various voltage scan rates using a carbon BP2000-based supercapacitor with an electrode composition of BP2000:Super C45:PTFE = 80:15:5 (wt%), electrode thickness of 100 μ m, and active carbon loading of 3.0 mg/cm^2. (b) Specific capacitance as a function of voltage scan rate. Reproduced with permission [161]. Copyright: Elsevier 2012.

4.2.4 Charge/Discharge Chronopotentiometry

The other common method for determining capacitance is charge-discharge (CD) which more accurately reflects battery test protocol. Constant current is drawn from the cell which decreases the voltage, simplifying the current integral. As such the stored capacitance can be determined from the discharge time and the voltage range. However, an additional series resistance contribution, known as the iR drop, will occur. When charging starts, the contribution of resistance from both electrodes is

easily seen as a voltage jump (*IR*). When the voltage limit is reached discharge begins at which time the voltage component due to series resistance becomes negative, creating a drop equivalent to two times the series resistance. If the leakage current negligible to discharge current (R_p, very large) then the simplified equation can be applied as seen in equation 4 [72]:

$$V_{cell} = I_{cell}R_{ESR} + I_{cell}\frac{t}{C} \qquad \textbf{Equation 4}$$

Where *t* is discharge/charge time, *I* is the current and *C* is the capacitance. In the case of pseudocapacitance the simplified capacitance is still easily calculated if we assume a simplified form, neglecting the plateau voltage created by the redox charge storage. However, if there is a significant leakage current then the linear slope of the derivation becomes more complicated and will gain some exponential character, due to the voltage dependence of the resistance which affects the simplification [72]**.**

$$V_{cell} = I_{cell}R_{ESR} + I_{cell}R_p(1 - \mathrm{e}^{-\frac{\mathrm{t}}{\mathrm{R_p C}}}) \qquad \textbf{Equation 5}$$

From the curves we can determine the overall stored capacitance between two voltages, an example of this phenomenon can be seen in **Figure 15**.

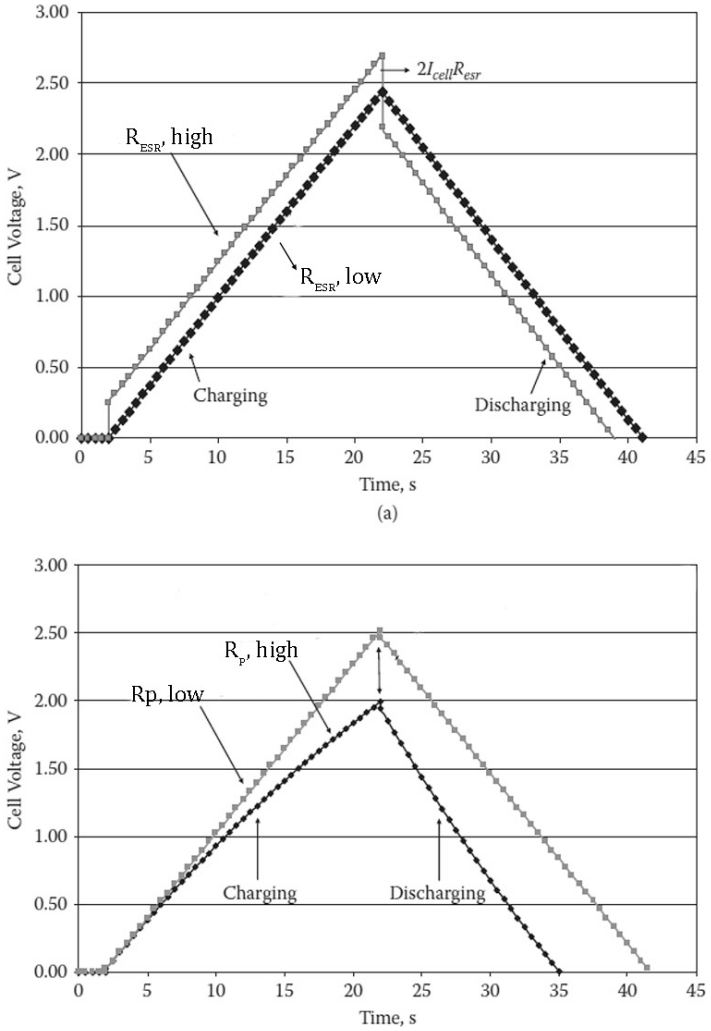

Figure 15: Calculated charge-discharge curves displaying the effect of a) non-negligible series resistance (R_{esr}) and b) non-negligible parallel leakage resistance (R_p). Adapted from [72].

4.2.5 Electrochemical Impedance Spectroscopy (EIS)

EIS, also known as AC impedance, is a technique used to determine the resistance and sometimes the resistive features of a capacitive system. Specifically EIS is a powerful tool for determining the resistive contributions of series resistance and the parallel leakage resistance which is a combination of leakage in EDLC and the faradic resistance in pseudocapacitive contributions. Also, the shape of the curve can be modeled and fit in order to find an equivalent circuit model for the cell. The technique is conducted by applying an alternating voltage to an electrode interface which could be

either half or full cell. The response function is then mapped from very high frequencies above 100kHz (low impedance, Z) down to 0.1 mHz (high impedance, Z). The nyquist plot formed displays the recorded real (Z') vs imaginary (Z") components of the response. In practice, the x-intercept of real impedance represents the series resistance (ESR), which is then followed by a semicircular hump region which is extrapolated back to the x-intercept. The extrapolated intercept is known as the charge transfer resistance, parallel leakage and/or the equivalent distributed resistance. At lower frequencies a 45^{o} region, known as Warburg diffusion regime, is often observed due to the transition diffusion control. To extract further information from the often complex curve shapes seen in practice circuit modeling software is often used to fit and solve for the resistive and capacitive parameters. At low frequencies if EDLC dominates and there is very little leakage resistance a close approximation of capacitance can also be made from Equation 6. Where Z'' is the imaginary impedance and f is the frequency [5].

$$C = -j\frac{1}{(2\pi f)Z''} \qquad \textbf{Equation 6}$$

Section 5: Pyrrolic-structure enriched nitrogen doped graphene

5.1 Introduction and Motivation

Recapping the background covered in previous in this thesis, supercapacitors are devices that can store greater amounts of energy than conventional capacitors, and they are able to deliver more power than batteries. Furthermore, they have relatively long cycle life and are capable of rapidly charging or discharging at high power density [16], [162]. There is significant interest to increase the use of supercapacitors in a wide and growing range of applications including electric vehicles, electric utilities, backup power and more [56], [163].Various materials have been used as electrode materials for supercapacitors including carbon materials [47], [164], [165], [166], [167], metal oxides [168], [169], [170] or conducting polymers [171]. However, carbon in its various forms is the most common electrode material for supercapacitor applications that require high capacitance and high power density. Graphene, the 2D carbon nanostructure, has attracted great interest for its excellent and unique properties e.g. high chemical stability, high electrical conductivity and large surface area. [55], [172], [173], [174], [175]

Many attempts have been made to modify graphene properties by controlling its surface structure. This method for controlling graphene structure acts as the basis for the first part of this thesis projects experimental investigation. The background for apply this strategy to graphene is derived from the success of doping carbon nanotubes with nitrogen heteroatoms [176], [177], [178]. Further, nitrogen has comparable atomic size and high electronegativity compared to carbon [17], [127]. This was postulated to also be an effective method to intrinsically modify graphene, where nitrogen chemically binds to the carbon lattice of graphene. Nitrogen doped graphene (NG) can be synthesized by a CVD approach where the nitrogen containing precursors are introduced to graphene at high temperature

with controlled atmosphere [17], [179]. Other methods include nitrogen plasma treatment or DC arc-discharge [61], [180]. The NG produced from these methods exhibit four different types of nitrogen bonding configurations: pyridine-like (N-6, 398.1-398.3 eV), pyrrole-like (N-5, 399.8-401.2eV), quaternary (N-Q, 401.1-402.7 eV), and oxidized nitrogen (N-O, 403-405eV). There are limited experimental or modelling studies available that investigate the difference of these four different nitrogen configurations and their contribution to supercapacitor performance [127], [181].

It is reported that NG prepared from the identified methods contain predominantly N-6 configured nitrogen [17], [61]. In this project we introduce an approach to produce NG using a hydrothermal method and systematically study the temperature impact on nitrogen configuration and performance. In addition, the graphene synthesized by this approach is more enriched with nitrogen in the N-5 configuration. The morphology and the introduction of nitrogen to the graphene were confirmed by SEM, XRD, Raman and XPS spectroscopy. The maximum supercapacitor performance was found using the NG sample prepared at 130^{o}C.

5.2 Experimental Procedures

5.2.1 Synthesis of graphitic oxide

The graphitic oxide (GO) was prepared following the modified Hummers' method in which graphite flakes are oxidized using a mixture of potassium permanganate, sulfuric acid and sodium nitrate [35]. In a typical synthesis 2 g of graphite powder and 1 g of sodium nitrate were stirred into 46 mL conc. H_2SO_4 in a round bottom flask while keeping the temperature at 0^{o}C using an ice bath. 6 g of $KMnO_4$ were added slowly to initiate the oxidization reaction. After 16 hours the mixture was diluted by deionized water, followed by the addition of 40 mL of 30% H_2O_2. After, the mixture was filtered, washed and dried.

5.2.2 Synthesis of NG

Figure 16 shows the hydrothermal synthesis of NG. In brief, a 2 mg/mL solution of graphitic oxide in deionized water was made and sonicated for an hour to ensure that the graphitic oxide was uniformly dispersed into few layer graphene sheets. Then, the pH was adjusted to 11 using an ammonia solution before adding 1.75 mL of aqueous hydrazine. The mixture was magnetically stirred for 10 minutes, transferred to a Teflon-lined autoclave and subjected to hydrothermal treatment for 3 hours, at various temperatures. After cooling, the mixture was filtered, washed with deionized water and dried in a vacuum oven. For the preparation of pristine graphene, $NaBH_4$ was used following our teams previous procedure instead of using ammonia and hydrazine [59]. The rest of the reaction conditions were kept the same as that of NG. Three different temperatures including 80^{o}C, 130^{o}C and 180^{o}C were investigated to determine the temperature effect. Correspondingly, the products were denoted as NG80, NG130, and NG180, respectively [182], [183].

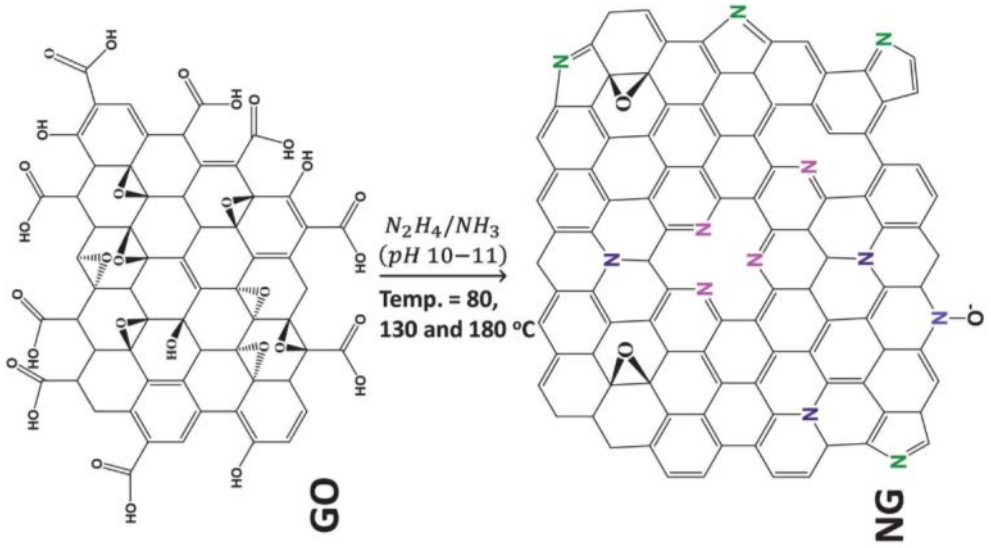

Figure 16: Hydrothermal reduction/doping of GO to NG. Reproduced with permission from [182]. Copyright Royal Society of Chemistry 2013.

5.2.3. Physical characterizations

Morphology of the NG materials was characterized by scanning electron microscopy (SEM) (LEO FESEM 1530) and transmission electron microscopy (TEM) (Philips CM300). XRD patterns were recorded by a Bruker-AXS D8 Discover diffractometer (Co-Kα source). X-ray photoelectron spectroscopy (XPS) was conducted to determine the atomic composition using a Thermal Scientific K-Alpha XPS spectrometer. Raman scattering spectra were recorded on a HORIBA Scientific LabRAM HR system (532.4 nm laser).

5.2.4 Electrochemical measurements

Electrochemical measurements were carried out using a CHI 760D electrochemical workstation (CH Instruments, USA). Cyclic voltammetry (CV), charge discharge (CD), and electrochemical impedance spectroscopy (EIS) techniques were all carried out following a 25-cycle CV activation between −0.1 and 0.9 V versus SCE at a scan rate of 0.1 $V.s^{-1}$ in 1 M KCl electrolyte. CV was carried out between −0.1 and 0.9 V versus SCE at scan rates between 0.01 and 0.2 $V.s^{-1}$. Working electrodes were prepared by pipetting an aqueous 2 $mg.mL^{-1}$ dispersion of NG onto glassy carbon. Charge/discharge (CD) was carried out between −0.1 and 0.9 V versus SCE at current densities between 0.5 and 1 $A.g^{-1}$. The capacitance of the three electrode supercapacitor cells was calculated based on the mass of the graphene or NG within the electrodes.

5.3 Result and Discussion

5.3.1 Structure and morphology characterization

Figure 17 shows the XRD results of NG prepared at different temperatures with comparison to the pristine graphene, G80. The figure shows a major peak (002) at about 24 ± 0.2^{o} which is corresponding to average interlayer spacing of 3.79, 3.73, 3.67, and 3.62 Å for G80, NG80, NG130, and NG180 respectively. These spacing values are a little greater than that of graphite (~ 3.36 Å) due to doping with nitrogen and oxygen and much larger from that of GO which exhibits its 002 plane diffraction at 10-12^{o}, corresponding to 8 Å lattice spacing, due to the oxygen functionalities on the surface. It is expected that by increasing the temperature more functionality is removed. This is expected to cause a slight decrease in the d-spacing as is observed here. In addition, the broadening of the peaks is evidence for the exfoliation and conversion of graphitic oxide into graphene and NG. In addition to the 002 plane there are weak diffraction peaks that are corresponding to 100 planes at 43^{o}. The crystal size (L_c) was estimated using the Scherrer equation where B is the full width at half maximum (FWHM) of the 002 peak in radians. The results listed in **Table 2** reveal the crystallite size increased slightly on introduction of nitrogen at 80^{o}C from G80 to NG80. However, the increase in L_c becomes more significant by increasing the temperature. L_c is based on the 002 peak therefore reflects the Z dimension of the graphene plates. Dividing the L_c with the corresponding d-spacing of the material gives an estimation of the number of layers; this is also listed in **Table 2**, which verifies the presence of few-layer graphene common with reduced graphene oxide materials.

Table 2. List of parameters deduced from XRD data for different materials. Reproduced with permission from [182]. Copyright Royal Society of Chemistry 2013.

Sample Description	2 θ, degree	d-spacing, Å	FWHM, radian	L_c, Å	No of layers
G80	23.48	3.79	0.0836	13.13	3.46
NG80	23.86	3.73	0.0925	13.23	3.55
NG130	24.24	3.67	0.1071	15.33	4.18
NG180	24.63	3.62	0.1079	16.98	4.69

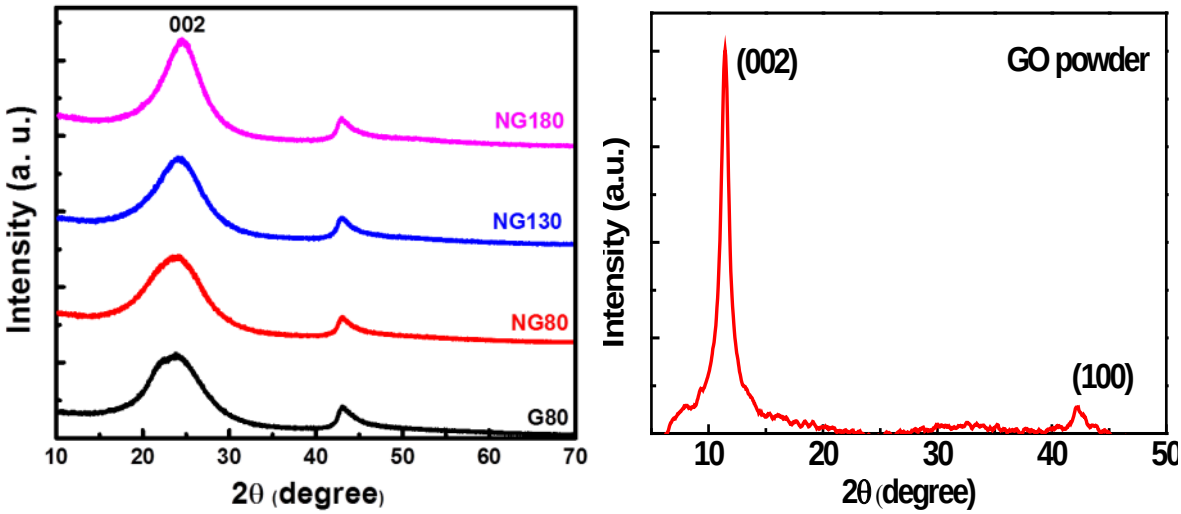

Figure 17. XRD for a) NG samples prepared at different temperatures with comparison with pristine graphene and b) GO. Reproduced with permission from [182](a). Copyright Royal Society of Chemistry 2013(a).

Figure 18a shows an SEM image of NG180. The figure shows exfoliated and wrinkled nanoplatelet texture characteristic for graphene. **Figure 18b** displays high resolution TEM image for NG180. The image shows that the NG prepared by this hydrothermal method is reasonably exfoliated and is only a few layers thick, in agreement with XRD. In order to estimate layer thickness the TEM was brought into focus on several sheet edges, enabling the count and averaging of the clearly seen termination of each layer at the particle edge.

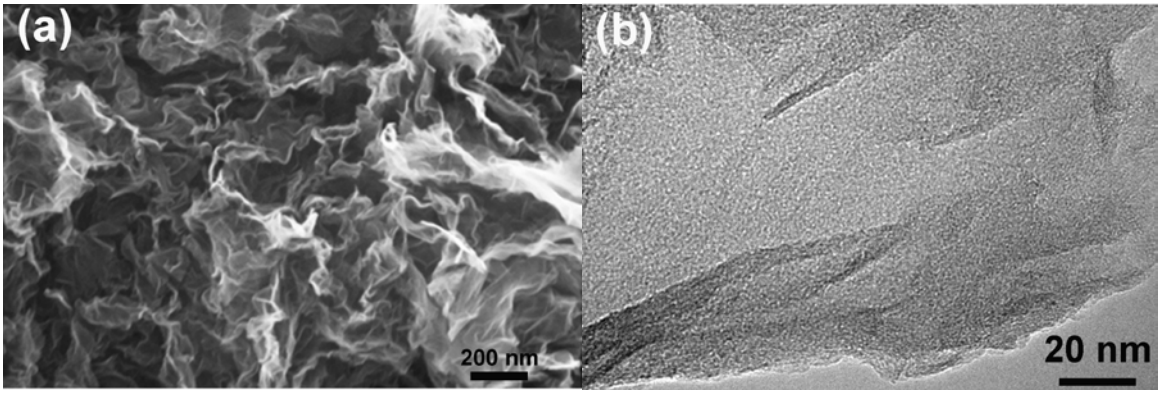

Figure 18. SEM micrograph of NG180 (a) and the corresponding high resolution TEM image (b). Reproduced with permission from [182]. Copyright Royal Society of Chemistry 2013.

Figure 19 displays the results of the Raman spectra of NG samples in comparison with pristine graphene. The presence of the D band peak as well as the very weak 2D band is a typical characteristic of chemically synthesized graphene [184], [185], [186]. The G band (peaks at 1500-1600 cm^{-1}) is attributed to the first order scattering of the stretching vibration mode observed for the sp_2 carbon domain, while the D band (1300-1400 cm^{-1}) is strongly associated to the degree of disorder within the graphitic structure [127]. A quantitative measure to estimate the degree of disorder in graphene is the ratio of intensities of the D and G bands [185], [186]. The values for I_D/I_G are 1.27, 1.36, 1.24 and 1.34 for G80, NG80, NG130, and NG180, respectively. This implies that the doped graphene in general has higher defect ratio (I_D/I_G) than the pristine graphene with the exception of this is NG130 which shows the lowest value for I_D/I_G. This might be attributed to structural differences in the nitrogen content for NG130. The I_{2D}/I_G ratios of 4.22, 4.23, 0.21, and 0.25 for G80, NG80, NG130, and NG180, respectively, are inversely related to the charge carrier concentration. These results indicate that I_{2D}/I_G is smallest for NG130, indicating that this sample has higher charge carrier concentration, which means it is more conductive.

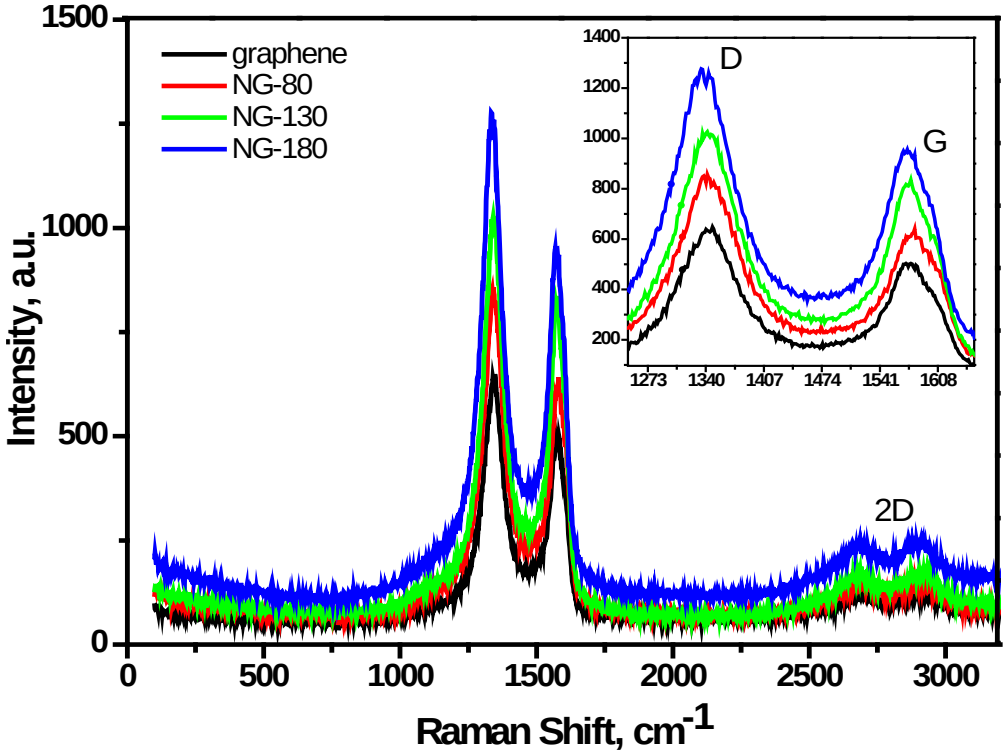

Figure 19. Raman spectroscopy of the NG samples prepared at different temperatures in comparison with pristine graphene.

Figure 20 compares the XPS results of the nitrogen doped graphene (NG). The figure clearly shows the appearance of a peak at about 400 eV which is corresponding to nitrogen. In addition, there is some residual oxygen in both samples (5-10%), which is common for the solution prepared graphene which are not as highly reduced as thermal reduction at high temperatures. The percentage of doped nitrogen was estimated by XPS analysis to be 3.20, 2.77, 2.77 atom% for NG80, NG130 and NG180. **Figure 20 b-d** show high resolutions of the nitrogen for the samples NG80, NG130 and NG180. The results of fitting of these spectra show that nitrogen bonds to the graphene matrix in four different forms including Pyridinic, Pyrrolic, Quaternary (graphitic) and oxidized nitrogen, which are centered at 398.9, 400.3, 401.8 and 405 eV [187], [188], [189], respectively in **Figure 20f**. In all samples, the pyrrolic nitrogen predominates, but the ratio of the pyrrolic nitrogen to the overall nitrogen is the highest for NG130.

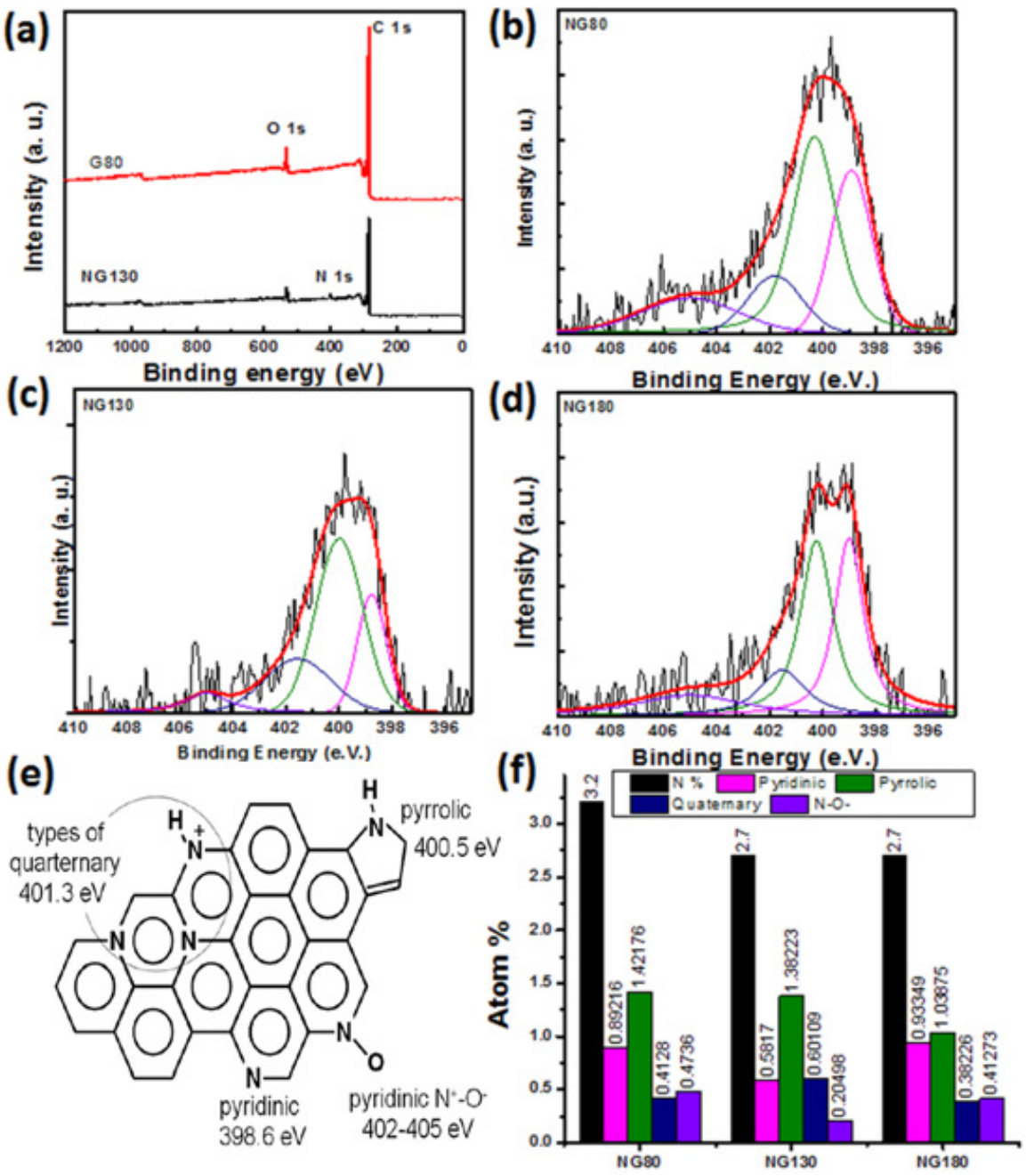

Figure 20: (a) XPS spectra for NG prepared at 130°C and pristine graphene; (b), (c) and (d) high resolution XPS for different NG samples prepared at 80, 130, and 180°C, respectively; (e) are the available nitrogen doping structures possible and their XPS signatures; and (f) is atomic % nitrogen in every NG sample and its associated resolved components in atom%. The black bar is the total atomic % nitrogen in that sample. Reproduced with permission from [182]. Copyright Royal Society of Chemistry 2013.

5.3.2 Electrochemical measurements

Figure 21a shows the cyclic voltammetry curves for NG prepared at different temperatures with a scan rate of 100 mV/s in 1 M KCl. The CV curves are virtually rectangular, showing that an approach to ideal and reversible capacitive behavior was almost achieved. The loop area for NG130 is greatest, depicting an optimal configuration. It is noteworthy that NG130 has the smallest band gap, the smallest I_D/I_G ratio, the highest predicted charge carrier concentration (based on smallest I_{2D}/I_G), and the highest proportion of Pyrrolic nitrogen to the overall nitrogen. At lower temperatures the hydrazine reduction may be insufficient to provide the necessary conductivity, while at higher temperature the graphene may be more hydrophobic resulting in less wettability. An additional explanation suggests that the reason why NG130 performs better than NG180C is the more dominant pyrrolic nitrogen content, while the large quantity of pyrridinic nitrogen in NG180 may be binding to strongly to the K^+ ions, affecting rate capability. **Figure 21b** depicts the effect of scan rate on the CV for the NG130 electrodes and performance calculated by **Equation 3**. The results of these calculations are plotted in **Figure 21bc,** showing that NG130 retains 80% of its maximum 194 $F.g^{-1}$ capacitance at 200 $mV.s^{-1}$. This is significantly better than G-80, which reached 100-130 $F.g^{-1}$ at 10-200 $mV.s^{-1}$ scan rates in previous work by our group [190]. **Figure 21ef** reveals similar a capacitive trend as measured by charge-discharge testing at rates between 0.5-1 $A.g^{-1}$ of active material. As described by **Equation 4** the nearly ideal EDLC behaviour of the CD curves are calculated from the slope of the discharge curve $C_s = I_s/(\Delta V/\Delta t)$, with no visible iR drop.

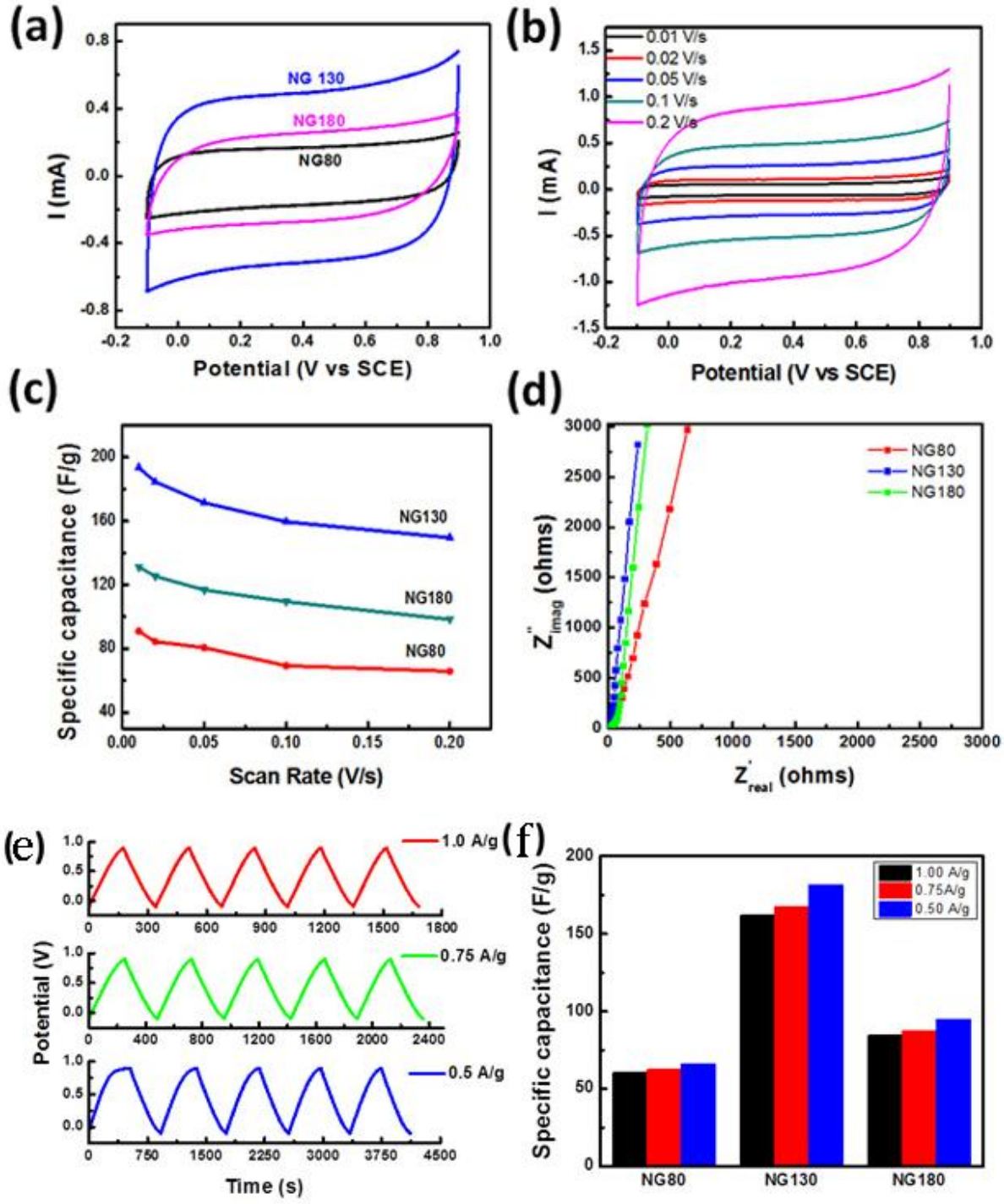

Figure 21: (a) CV curves for NG samples prepared at different temperatures measured at 100 mV/s in 1 M KCl, (b) CV curves for NG130 at different scan rate, (c) The capacitance of the different material as a function of the scan rate, and (d) the EIS of the different NG electrodes. e) Testing results from CD for discharge rates between 0.5-1 A/g and f) the capacitive performance calculated from CD. Reproduced with permission from [182]. Copyright Royal Society of Chemistry 2013.

The results show that optimal processing with nitrogen doped graphene clearly increases its capacitive behavior. The reason may be attributed to the high electronegativity of nitrogen which helps create dipoles on the surface of graphene, resulting in higher tendency to attract charged species to the surface. This interesting result is further confirmed by EIS measurements of the different NG electrodes **Figure 21d**. The figure shows the Nyquist plots for the three different electrode materials; NG80, NG130, and NG180. The linearity in the EIS plots at low frequency suggests that the electrode process is under diffusion control, related to the formation rate of the electric double layer (EDL). The larger the slope the lower the diffusion resistance and the faster the EDL will be formed [191], [192]. The slope for the NG130 electrode is obviously greater than it is for the G80, NG180 and NG80 electrodes, which further emphasizes that NG130 forms more ideal supercapacitor behavior. The three electrodes have semicircles at the high frequency with very small diameters, this suggest a small charge transfer resistance. Meanwhile, the intersections with x-axis at high frequency represent the ESR of the NG and G materials at close to 6Ω for each.

For supercapacitors, energy and power densities are two important parameters to consider. However, it should be noted that performance calculations based on a three-electrode system can overstate material performance in real devices due to the low weight loading on the electrode. With that in mind, the energy density estimate for an equivalent two electrode cell composed of NG130 is calculated using the following equation [30], [160], [193].

$$E = \left(\frac{C_s}{4}\right)\left(\frac{\Delta V^2}{7.2}\right) \qquad \textbf{Equation 7}$$

Where $C_s/4$ is the specific capacitance estimate of a two electrode cell in farads per gram as discussed in **section 3.2.2** of the thesis, ΔV is the potential window for CV measurements in volts, and E is the energy density in Wh.kg^{-1}. Utilizing the three electrode test data from the CV measurements, the maximum energy densities (measured at a scan rate of 0.01 V/s) of a two electrode cell are estimated to be 6.7 Wh.kg^{-1} for the NG130. The maximum average power density of the electrode was calculated using the energy densities and the discharge time *t*, from CV at 0.2 V/s, to be 3.7 kW/kg.

5.4 Summary

Graphene and nitrogen doped graphene have been synthesized by hydrothermal technique from graphitic oxide. XPS confirmed the percentage of doping was 2.77-3.2 %. In addition, among the different nitrogen species, pyrrolic nitrogen was found to predominate. The doping was found to significantly enhance the specific capacitance in the temperature optimized condition, partially due to the improved electrical conductivity of the materials. This is in agreement with the lower band gap and lower impedance results among the NG series. High performance reaching: capacitance of 194 F/g, equivalent cell energy density as high as 6.7 Wh.kg^{-1} and average power density for the equivalent cell as high as 3.7 kW.kg^{-1}. This material is an excellent candidate for electrical double layer supercapacitor and suggests future study is required to keep improving functionality, quality, and performance of our graphene.

Section 6: Free Standing Graphene foam for supercapacitor

6.1 Introduction and Motivation

Two dimensional graphene electrodes have proven to have the potential to outperform activated carbon materials in supercapacitor applications for reasons discussed in sections 2 and 3 of this thesis. Three dimensional graphene foams have the potential to push these advantages further by doing several things including: increasing accessible surface area, providing large channels for rapid ion transport, creation of conductive networks on a macro-scale and allowing for free-standing electrodes free of inactive binder and conductive electrode materials. Cell fabrication can also be simplified by combining material synthesis and electrode fabrication into a single process. Templated graphene foams produced by CVD growth of graphene have been demonstrated with high success when deposited with pseudocapacitive materials [85], [140], [141], [142]. However, its double layer capacitance (40-50 F/g) is lacking and the foams formed are not robust enough or dense enough to be useful on a production scale. In his chapter, we investigate several approaches with the intention to find a method for the production of free-standing graphene foam networks. The foams formed from GO need to have high capacitance, with sufficient conductivity to support full cell operation at practical weight loading of more than ~1 mg/cm^2 of electrode area. The chosen platform to satisfy these projects goals will also provide the support for future work on graphene supercapacitors.

6.2 Experimental

6.2.1 Characterization

Morphology of the foam materials was characterized by scanning electron microscopy (SEM) (LEO FESEM 1530). Electrochemical measurements were carried out using a Versastat electrochemical

workstation (Princeton Applied Research, USA). Cyclic voltammetry (CV), charge discharge (CD), and electrochemical impedance spectroscopy (EIS) techniques were all carried out following a 25-cycle and performed on a 2-electrode cell with a minimum active mass of 0.5 mg. The cells were prepared by pressing the freestanding electrodes and assembling the cell using a similar configuration to **Figure 13**. The cell was soaked 10 hours in 2 M KOH electrolyte and bubbled with N_2 for 30 minutes before CV activation between 0 and 1 V at a scan rate of 0.05 $V.s^{-1}$. CV was carried out with a 1V range at scan rates between 0.05 and 1 $V.s^{-1}$. Charge/discharge (CD) was carried out between current densities of 0.5 and 1 $A.g^{-1}$. EIS was performed using a frequency range between 0.1Hz and 1MHz. The capacitance of the three electrode supercapacitor cells was calculated based on the mass of the graphene within the electrodes or the area/volume of the electrode layer. Freeze drying of the materials was performed using a labconco freezone drying system which operates at -50^oC and pressure below 0.1 mbar.

6.2.2 Synthesis of GO

Recent work on GO has discovered a less toxic procedure by eliminating $NaNO_3$ and the toxic gases NO_2 and N_2O_4 that are formed during oxidation. Further, the phosphoric acid used instead improves the exfoliation efficiency [111]. With this in mind we have adapted our GO procedure to improve the safety of the process.

The graphitic oxide (GO) was prepared following the modified improved hummers' method in which graphite flakes are oxidized using a mixture of potassium permanganate, sulfuric acid and phosphoric acid [110], [111]. In a typical synthesis 2.5 g of graphite powder were stirred into 360 mL conc. H_2SO_4 and 40mL conc. H_3PO_4 in a round bottom flask while keeping the temperature at 0^oC using an ice bath. 18 g of $KMnO_4$ was added slowly to initiate the oxidization reaction. The ice bath was

removed; the solution heated to 50^{o}C and after stirring for 16 hours the mixture was diluted by deionized water, followed by the addition of 10 mL of 30% H_2O_2. After, the mixture was filtered, washed and small portion of the product dried using a freeze dryer to preserve the surface area of the sheets.

6.2.3 Synthesis of exfoliated rGO film

Robust, flexible GO films were prepared from a viscous GO solution by capitalizing on the highly dispersed hydrophilic flakes. 200 mg of a stock 4 mg.mL^{-1} solution were concentrated to 20mg.mL^{-1} using centrifugation. The solution was then cast into a polished glass mold and leveled to ensure even thickness distribution in the final film. The films were allowed to dry undisturbed under laminar air flow overnight and peeled off the mold to yield 25um±3um thick compact GO films (**Figure 22**). However, the insulating nature of these films made them undesirable for supercapacitor and had to be reduced before use.

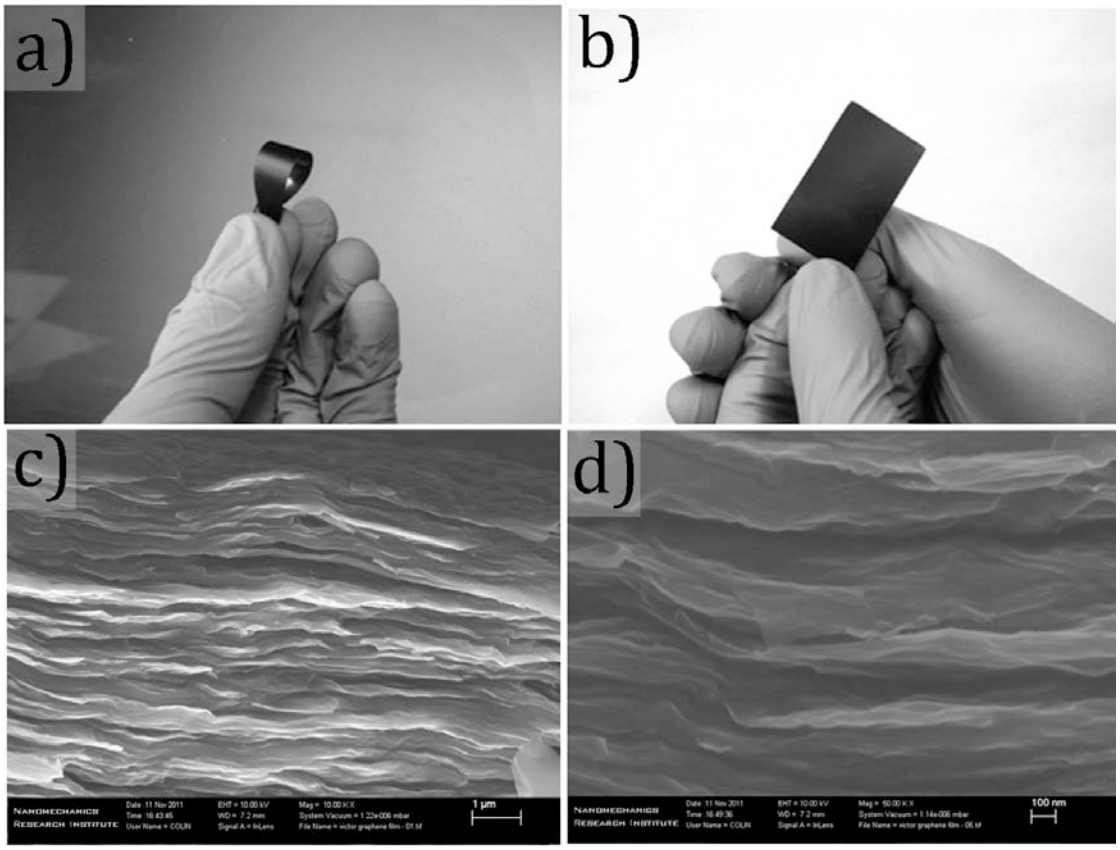

Figure 22: Visual images of the a) flexible property and b) well formed GO films. SEM images of the films cross-section reveal the tightly layered structure at both 10000x and 50000x magnification.

Two methodologies were used to reduce the films. The first method involved a slow temperature ramp (10^{o}C/min) under argon to preserve the flexibility of the GO sheets while attempting to achieve high conductivity and expose the layered pore structure. This method produced a 13um thick sheet similar in appearance to aluminum foil, using an annealing temperature of 800^{o}C for 3hr. However, the tightly restacked pore structure resulted in very low capacitive performance, not discussed further in this thesis. In a second method, the GO film was placed between two quartz plates and exposed to rapid thermal shock at 800^{o}C and held for 10 min (ex-rGO film, **Figure 23**)). The film is porous but very brittle due to deflagration of the rapid gas escape through the compact GO layers.

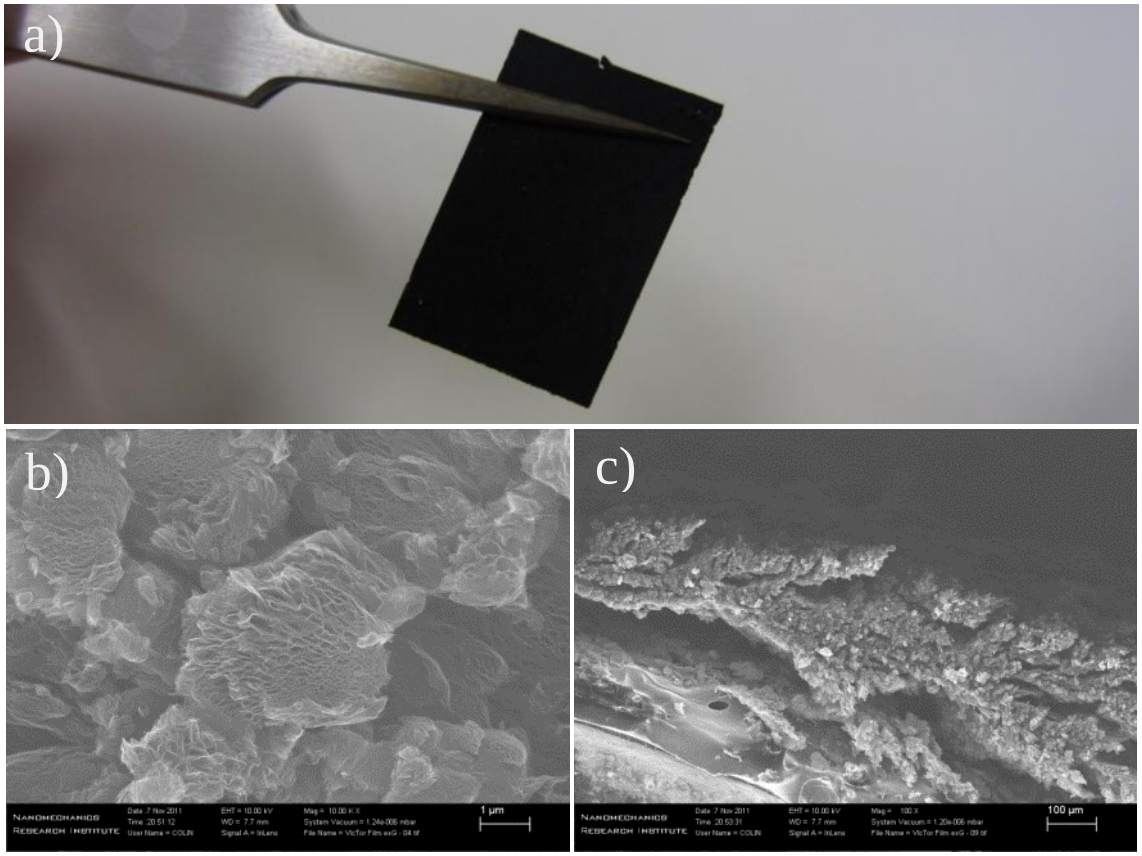

Figure 23: a) Image of the ex-rGO film after annealing at high temperature and SEM of the exfoliated layers cross-section at b) 10000x and c). 100x

6.2.4 Synthesis of freestanding directly freeze dried foam

Freeze cracking of the GO foams is an issue, through experience we have discovered that cryogenic type freezing with liquid nitrogen or nitrogen cooled alcohol causes an ice shell to form, which cracks once the internal fluid freezes. However, using only a standard freezer the ice crystal size is significantly increased which results in non-uniform freezing and agglomeration of GO. To get uniform ice crystallization we drew on inspiration from the freezing mechanism of rivers. The cold front is only exposed to one surface of the liquid which is under constant motion. The motion prevents irregular growth of the ice phase and more uniform cooling. The result is crystal clear ice formation. In our experiment the solution was placed on an insulated pedestal with the bottom face

exposed to liquid nitrogen for cooling. 20 mL of 4 $mg.mL^{-1}$ GO poured into the chamber and kept in motion by constant air flow on the solution surface. The result was the rapid, but uniform growth of the ice front toward the surface (**Figure 24**). After freeze drying, the graphene oxide foam was pyrolyzed for 1.5hr at 900^{o}C under Ar at 150 sccm. To prevent deflagration of the foam structure a slow temperature ramp of $5^{o}C.min^{-1}$ was used which enabled the gas to gradual escape through the highly porous network (FD-rGO foam).

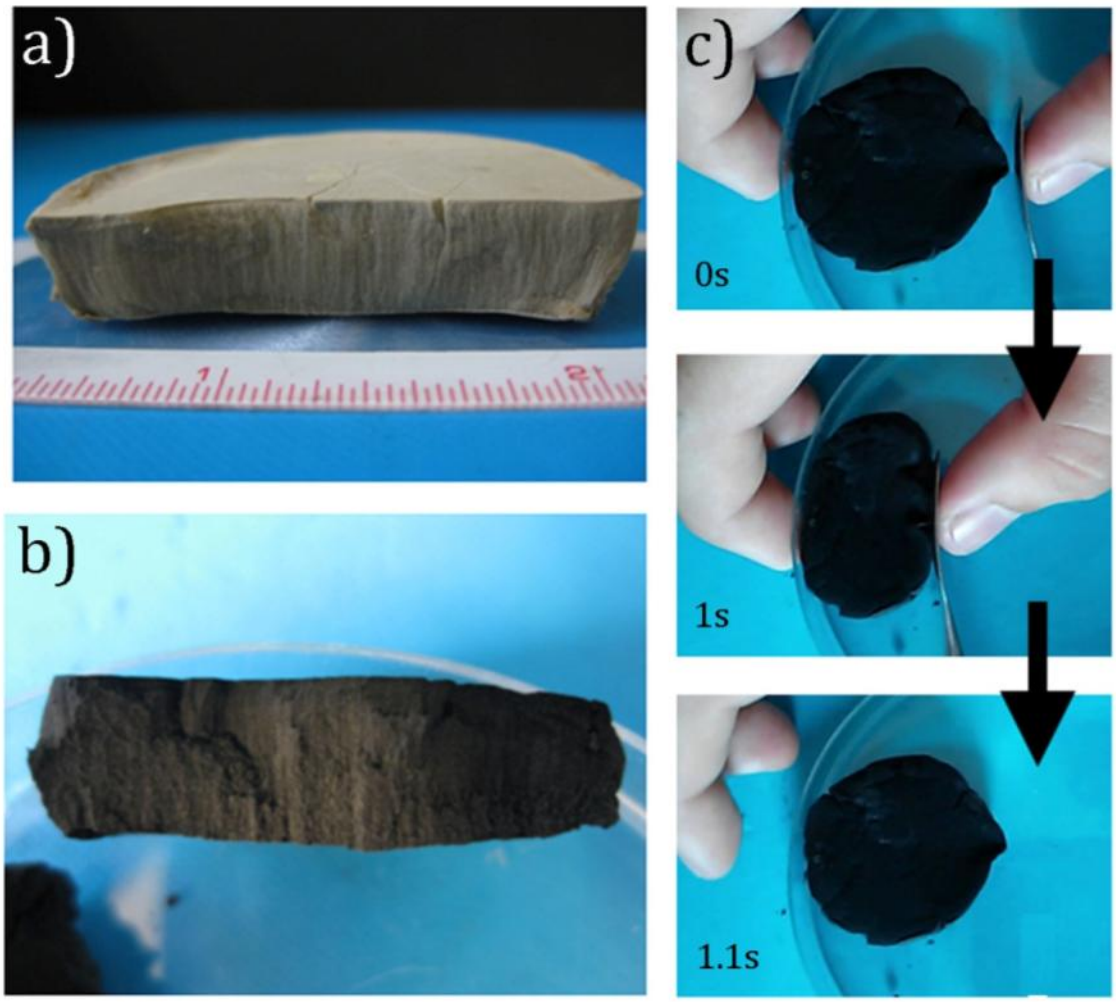

Figure 24: Cross-section images of the unidirectional and uniform ice growth resulting in a) GO foam and after annealing b) FD-rGO foam. c) Images of the rapid recovery to original shape after subjecting the foam to ~50% strain, repeated with similar results for 10 cycles.

6.2.5 Synthesis of freestanding and nickel supported self-assembled rGO foam

Freestanding, self-assembled foams (SA-rGO) were prepared using ascorbic acid which has been previously been discussed to be an effective reducing agent even at low temperature. Ascorbic Acid (AA) was added in a 2:1 mass ratio with 4mg/mL GO. Self assembly was done at 70^{o}C for 4 hours, before dialysing the impurities and excess AA by soaking in water. After assembly the foams were freeze dried and tested for performance (**Figure 25**).

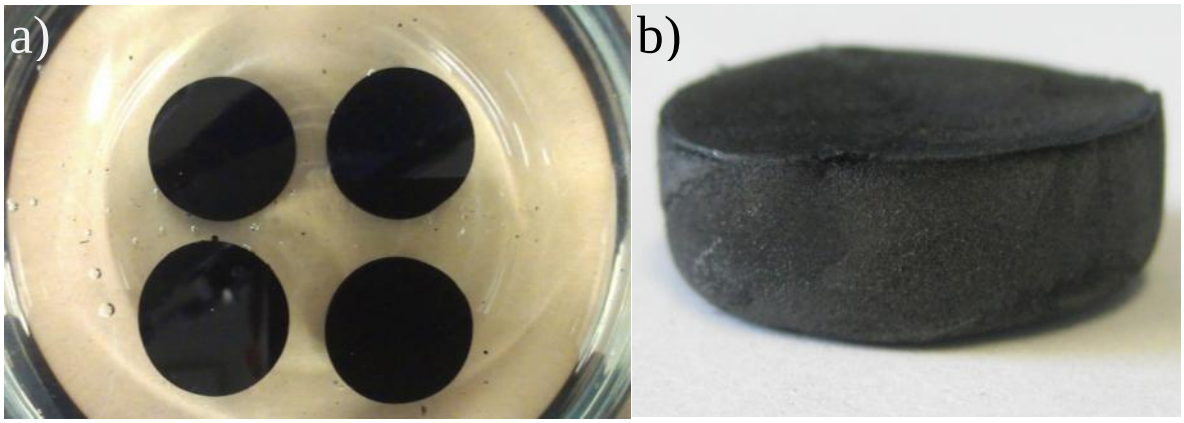

Figure 25: Images of the a) wet and b) post freeze drying SA-rGO foams.

Nickel foam supported rGO foam formed by self assembly (Ni/rGO foam) was also prepared after it was discovered that the foam grows preferentially on the nickel foam surface enabling the growth of an integrated foam electrode and current collector during material synthesis. To produce the foams Ni foam was punched into electrodes with a 14mm punch and pressed to a uniform thickness of 0.8mm. The background information presented in this thesis showed that Ethylenediamine (EDA) can prevent restacking at high concentrations during GO reduction by functionalizing the surface. Therefore, the Ni electrodes were processed for the purpose of higher loading and foam density necessary for scalable supercapacitor application that considers volume density. This was done by impregnating GO solution between 10-20 mg.mL^{-1} into the Ni foam before reduction.

Using the in-situ reduction technique similar to SA-rGO the foam could be grown on the nickel and removed, however the pore network was significantly less dense due to the lower concentration of GO present in the pores when self assembly begins to occur (in-situ Ni/rGO foam). As a result the volumetric capacitance suffered significantly and the connectivity/conductivity of the graphene network within the Ni foam collector was also insufficient to produce equivalent gravimetric performance to the impregnated Ni/rGO foams (**Figure 26**).

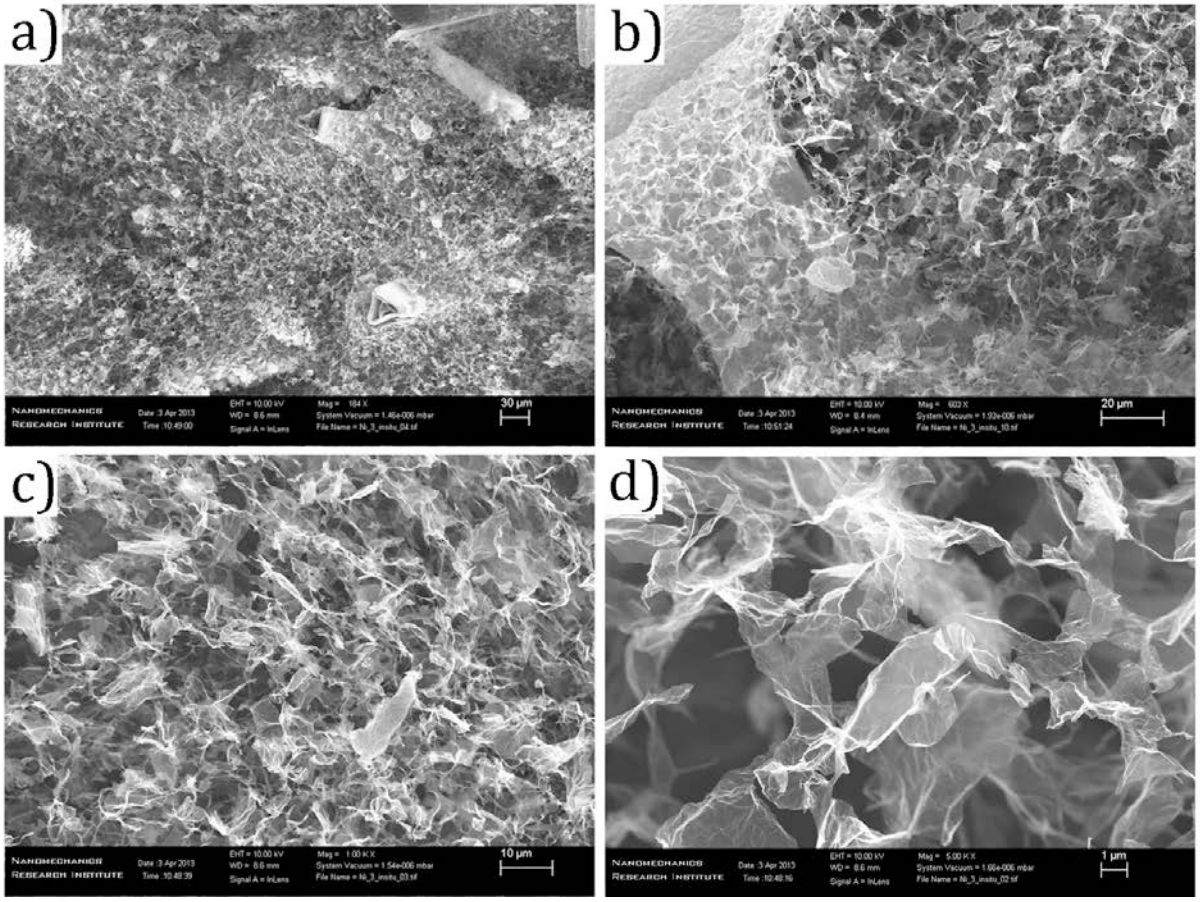

Figure 26: SEM images describing the pore structure of in-situ grown Ni/rGO foam depicting the well distributed but low density at a) 185x, b) 600x and c) 1000x. d) At 5000x magnification the thin pore walls are clearly evident in addition to the narrow connection points of the sheet edges.

The GO impregnated Ni electrode was placed at the bottom of an aqueous reaction vessel with EDA between 0.05-1 M and the viscous GO solution remained trapped in the 400-600 um pores of the Ni foam. The electrodes were then reduced for 8hr using a range of 60-90^{o}C for 4hr. After which time the foams were formed but only slightly reduced. To effectively reduce, the wet foams were placed in 0.05M AA solution for 4 hours at the designated batch temperature. The internal pore structure of the Ni/rGO foams was analyzed by SEM in **Figure 27**. Clearly, there is a dense assembly of the foam within the nickel structure and based on the high resolution imaging it is also clear that there has been minimal sheet restacking. As a control, foams made using AA only at 75^{o}C, 4 hr was also prepared to verify the performance improvement due to EDA.

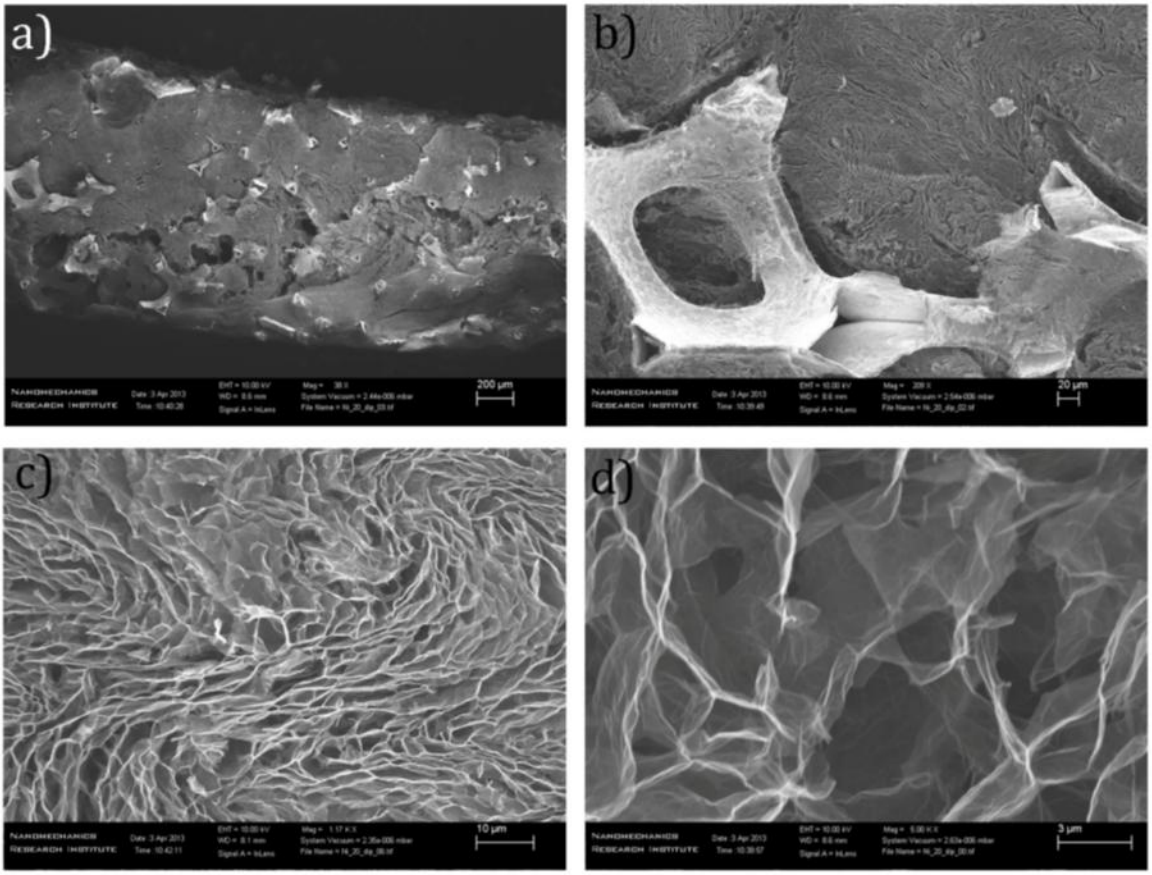

Figure 27: SEM images of the 20mg.mL^{-1} impregnated Ni/rGO foams depicting the dense layering at a) 40x, b) 200x, c)1200x. Higher 5000x magnification reveals the separated structure that results in thin few layer graphene pore walls.

6.3 Electrochemical Results and Discussion

In order to determine which method to utilize, CV performance testing was performed on each electrode system. Further, in evaluation of applicability to scalable production the mechanical integrity of the materials were considered. For comparison r-GO powder prepared by standard $NaBH_4$ reduction [59], [194] and following common practice were mixed into a slurry [34][195][160]. The best performance of this method was able to yield glassy carbon three electrode test performance of 140 F/g in KCl electrolyte for the rGO. However, the increased ion mobility of the OH^- ions in KOH electrolyte boosts the performance significantly over neutral electrolyte such as KCl, to nearly 190

$F.g^{-1}$ when only a few micrograms are deposited on the electrode surface by this method. However, at larger mass scales close to 1 mg this number is expected to decrease significantly, and requires the use of additional conductive and binder components to support the current. To do this, the slurry of electrode materials were made of 20wt% PVDF, 20wt% Carbon Black and 60wt% prepared graphene powder and drop cast a thin coating, onto stainless steel current collector plates. When considering both the active and inactive electrode mass of the electrode materials CV full cell performance was 16.7 and 27.7 $F.g^{-1}$, for the $100mV.s^{-1}$ and $10mV.s^{-1}$ scan rates respectively (**Figure 28a**). This suggests that considering the active graphene material only, the half cell equivalent performance was close to 173 $F.g^{-1}$ and lost ~66% of the capacitance at the higher $100mV.s^{-1}$ discharge rate.

The initial ex-rGO method to exfoliate robust and flexible GO films by thermal shock resulted in the retention of film shape. However, the brittle nature made the foam film unworkable and further exhibited insufficient material performance of only 72 $F.g^{-1}$ at 10 $mV.s^{-1}$ (**Figure 28b**). In a similar high temperature method, FD-rGO was much lower in density (~ 4 $mg.cm^{-3}$) and the flow channels in the resulting foam allowed for gas to escape rapidly and prevented sheet restacking similar to that of annealing the GO film. This proved sufficient to avoid deflagration of the surface when furnace ramp rates were kept slow. As a result, the FD-rGO provided a more robust, scalable process but performance was only slightly improved from that of the slurry, although a more ideal capacitive shape can be seen **(Figure 28c)**. As a result when considering just the graphene mass within the slurry, it still outperformed the FD-rGO foam. However, the well distributed pores and restacking prevention was able to achieve a strong long range network with comparable performance and over 1 mg/cm^2 loading on the electrode, even without a conductive additive. With further work, this process could provide even higher specific capacitance. However, the low density/low volumetric performance suggests the most promising method for supercapacitor development may be higher density self-assembled rGO foams (SA-rGO). From the CV performance test we reached similar

performance to the FD-rGO but the SA-rGO materials were significantly more dense, ~15-20 mg.cm^{-3} depending on the reduction time. The CV curve in **Figure 28d** depicts capacitance of 28.7 F.g^{-1} and 19 F.g^{-1}, at 10 mV.s^{-1} and 100 mV.s^{-1} respectively.

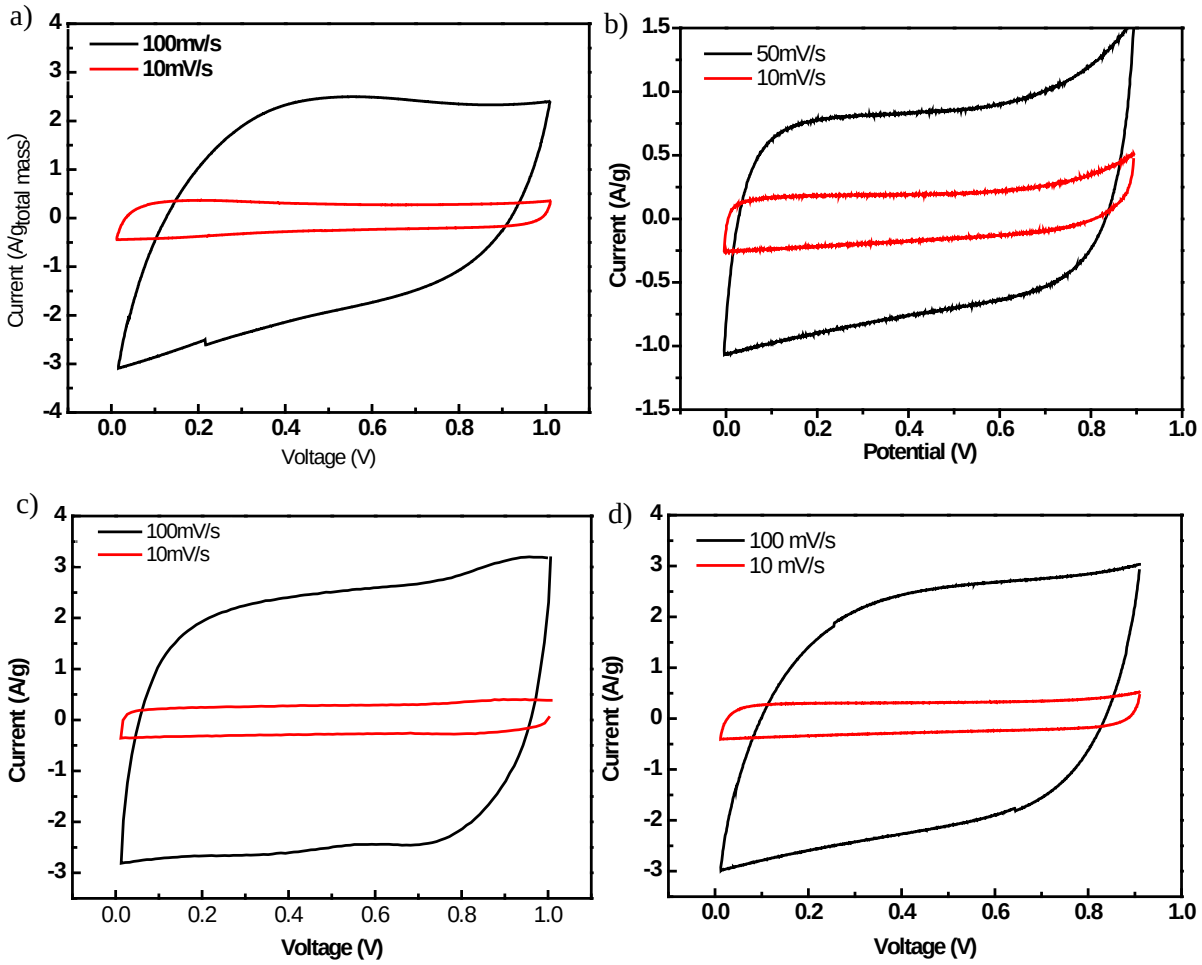

Figure 28: Full cell CV performance at both low and high scan rates for graphene materials including: a) 2D rGO powder in a liquid slurry, b) ex-rGO film, c) FD-rGO foam and SA-rGO foam. Mass is that of the active/inactive mass on both electrodes, not including current collector plates.

The outstanding problem with all of these techniques however is the variability in cell preparation and difficulty in prepping and cutting the foam materials for testing, in order to get a sufficiently strong electrical contact. Despite the acceptable performance of FD-rGO and SA-rGO, neither is truly capable of being tested freestanding. Without pressing the foams onto the current collector

performance was poor and was highly resistive as indicated by a significant linear slope in the CV curve. Further, neither material was able to outperform the graphene only capacitance of the slurry method. However, the use of nickel foam as a current collector enables the self assembly to occur with a much shorter conduction pathway than in the unsupported foam and further integrates added strength required to make the as synthesized foam applicable directly as a supercapacitor electrode. Initial testing of the impregnated Ni/rGO foams was conducted to find an optimal impregnation concentration. After synthesis of foams with impregnation concentrations of 5,10,15,20 $mg.mL^{-1}$ the mass loading of five electrodes was averaged to reveal 0.85 $mg.cm^{-2}$, 1.1 $mg.cm^{-2}$, 1.3 $mg.cm^{-2}$and 2.5 $mg.cm^{-2}$, respectively. At 20$mg.mL^{-1}$ impregnation the viscosity was high enough that it trapped a significantly increased amount of GO within the Ni foam matrix. Further, as seen by **Figure 29ab** the increased concentration lead to stronger gravimetric and much higher volumetric performance at higher concentration (**Figure 29c**). This suggests the presence of improved network connectivity and is in agreement with the SEM in **Figure 27.** Even at high concentrations the graphene restacking is prevented by the low temperature reduction and the presence of EDA as a cross-linking agent along the basal plane of the graphene sheets. This is also supported by the lower performance of the impregnated Ni/rGO foam prepared without the use of EDA (**Figure 29c**). EIS testing shown in F**igure 29d** for the 20 $mg.mL^{-1}$ impregnated rGO/Ni foam electrode depicts that the ESR is only 720 mΩ, the charge transfer resistance is 300 mΩ and the large slope indicates very little diffusion resistance. More importantly, the equivalent half cell capacitance of the material approaches 144 $F.g^{-1}$, which is much greater than the electrode mass in the slurry method performance and comparable to the performance if only the graphene mass is considered for the slurry method.

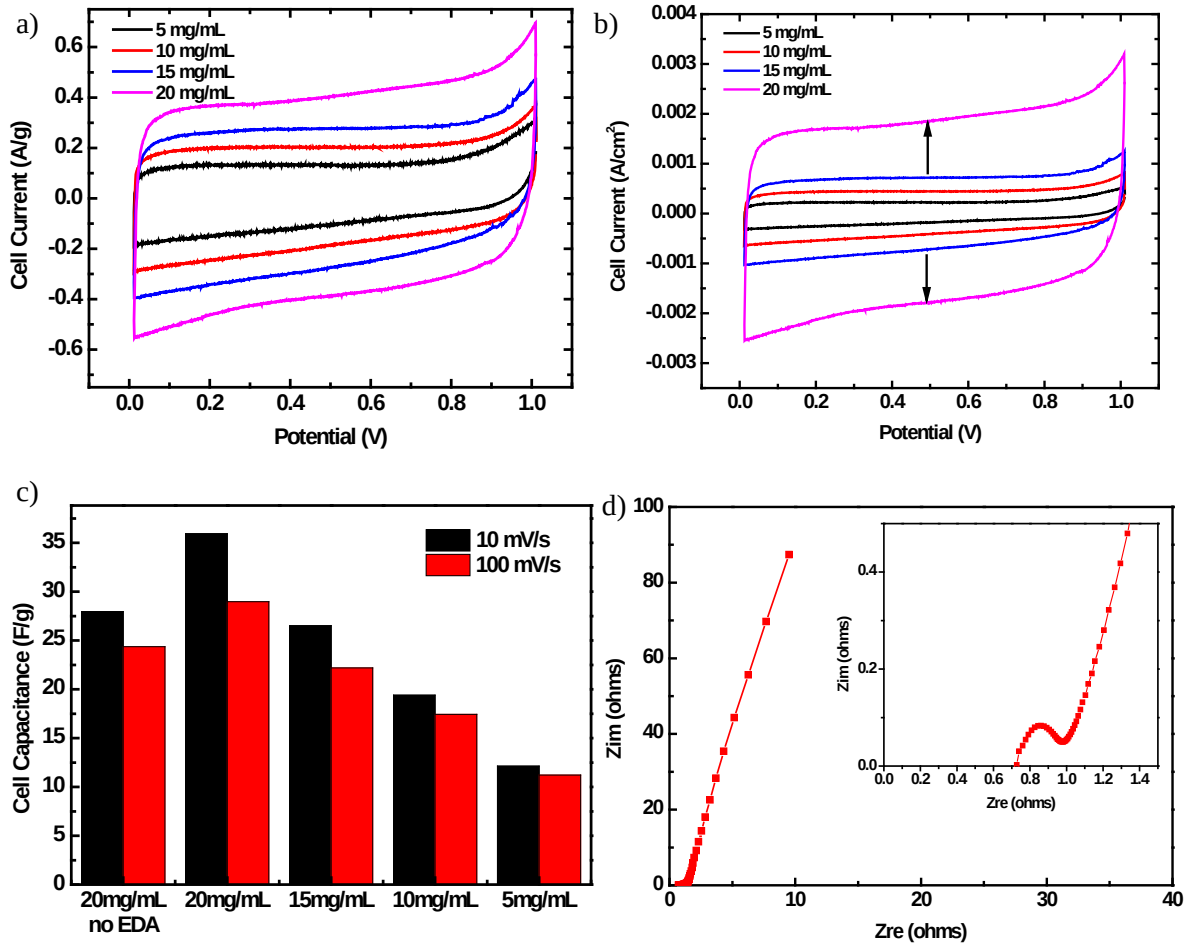

Figure 29: Performance characteristics of Ni/rGO foams prepared by a GO impregnation method. CV data from various impregnation concentrations between 5-20 mg.mL^{-1} considering both capacitances per unit: (a) mass of foam within both electrodes and (b) area of the cell. c) Comparison of the gravimetric performance results. (d) EIS spectrum of 20mg/mL impregnated Ni/rGO foam.

To see if the performance could be optimized further the 20 mg.mL^{-1} impregnated Ni/rGO foam electrodes were also made with increased EDA concentration and with varied reduction temperature. Within the batch test, electrodes were impregnated and electrochemical characterization was performed in a random order. To keep the aqueous batch processing simple and safe, temperatures were kept below the boiling point of water. By refining the dip impregnation technique the GO mass became more consistent, with less excess coating. This creates less electrode-electrode variation and the mass loading on the final electrodes decreased to 1.95 mg.cm^{-2}, compared to the 2.5 mg.cm^{-2}

reported for the concentration study. The evidence in **Table 3** reveals that the electrode to electrode variation is likely confounding any factor effects that may exist. However, it can be observed that the 90°C electrodes overall performed slightly better, with greater high rate capacitance retention probably due to improved conductivity. At the higher temperature it is also seen that lower EDA concentration led to the highest performance.

Table 3: Investigation of cell capacitance per unit area with respect to change in the reduction temperature and cross-linker concentration.

Scan Rate	**Cell Capacitance (mF/cm^2)**			
(V/s)	**0.05 M EDA**	**0.1M EDA**	**0.5M EDA**	**1M EDA**
75°C reduction temperature (original method)				
0.01	139.4	N/A	N/A	N/A
0.1	118.5	N/A	N/A	N/A
60°C reduction temperature				
0.01	111.4	136.5	122.2	139.0
0.1	89.9	110.5	103.3	120.0
90°C reduction temperature				
0.01	145.2	137.8	124.4	122.5
0.1	124.0	118.4	106.2	106.2

Further, performance verification of the electrode production utilizing 20 $mg.mL^{-1}$ impregnation, 90°C and 0.05M EDA can be seen in **Figure 30**. Utilizing **Equation 4** to determine the capacitive performance charge discharge that capacitance measured at 27-35 $F.g^{-1}$, for 1-10 $A.g^{-1}$ respectively. This is in close agreement with that observed for CV results. Based on the CD data the maximum measured energy stored within the cells is determined to be 4.9 $Wh.kg^{-1}$ and the highest average power output tested was 5.5 $kW.kg^{-1}$, where mass represents the graphene within the Ni/rGO foam electrode. Based on the equation ($P_{maximum}=V^2/4R_{ESR}$)[5], the IR drop from CD testing suggests the maximum power of the cells are 28.1 $kW.kg^{-1}$. Considering the thickness of the electrodes after pressing for cell preparation (100 um each), shrink wrap (~50um thick) and the thickness of commercial separator membranes (~25um), the three component cells could be packaged into credit card type cells approximately 325 um in thickness. Based on these assumptions the volumetric capacitance of the packaged cells would be 4.3 $F.cm^{-3}$ and considering both the graphene and nickel

foam masses (1.539cm^2 Ni foam weighs 66mg) the specific capacitance of the cells would be 1.56 F.g^{-1}. As a standalone electrode, this is comparable to other small package double layer devices which range from 0.4-7 F.cm^{-3} and 0.3-4 F.g^{-1} [196]. Future improvements to the foams conductive network, and capacitance by higher temperature treatments could make the integrated electrodes more competitive with large EDLC devices which exhibit 2.5-15 F.cm^{-3} and 3-8.5 F.g^{-1}. Significant engineering improvements could also be found by selecting lower density Ni foam or reducing the thickness of the Ni foams walls by etching. This is because, in its current design nickel accounts for 95% of the cells mass. More importantly, the integrated electrodes could make an excellent support for anchoring dense pseudocapacitive materials that could significantly improve both the gravimetric and volumetric capacitance of the active material. Results of a short term cycle test can be seen in **Figure 30b**, which depicts irreversible loss quickly approaching a stable reversible capacitance equal to 87% of the initial measured capacitance. Longer term testing would be necessary to better determine the cycle life of the devices.

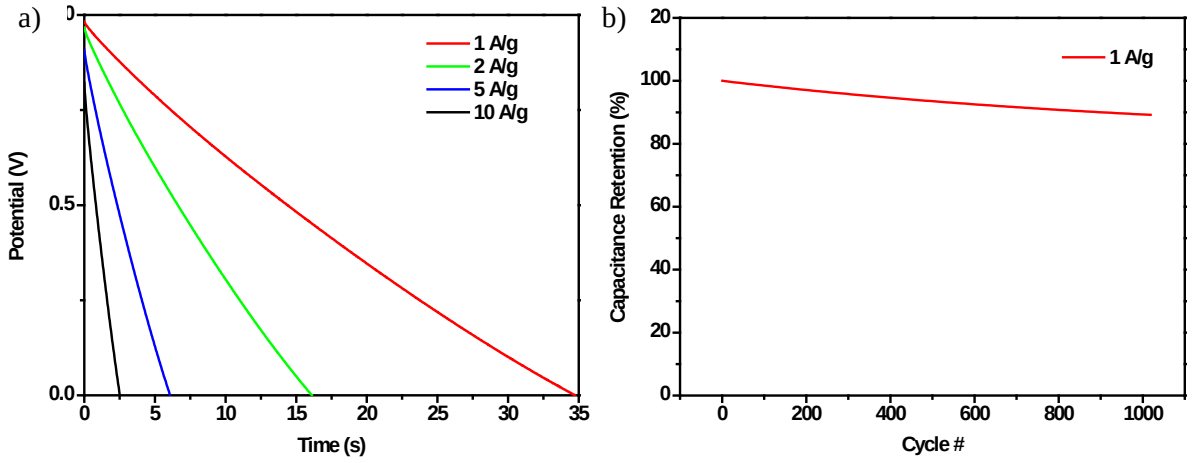

Figure 30: a) CD data for cells built using an integrated 20 mg.mL^{-1} impregnated Ni/rGO foam electrode/current collector from 1A.g^{-1} up to high rate performance at 10 A.g^{-1}. b) Short cycle stability test conducted at 1 A.g^{-1}.

6.4 Summary

We have successfully tested and synthesized graphene foam by several methods. The foams were able to successfully prevent the restacking of graphene, as shown by SEM. The higher density self-assembled graphene foams were of the best CV performance and were able to self assemble onto nickel foam. The result of this investigation was an integrated current collector/electrode as prepared by the synthesis of graphene foam on a nickel foam substrate (impregnated Ni/rGO foam). The optimized electrodes exhibited a high carbon mass loading of ~2 $mg.cm^{-2}$. This was much higher than that reported by CVD based graphene growth which only covers the surface of the nickel foam. Further, this integration eliminated the need for separate dispersion, addition of inactive binder and conductive materials and electrode preparation steps in the manufacturing process. The process also utilized low temperatures below the boiling point of water and an environmentally friendly reducing agent ascorbic acid. The self assembled networks created tight, well ordered morphology that enabled the high loading of graphene material to store capacitance of 144 F/g, retaining ~85% capacitance at a rate of 10 A/g. Currently, the full cell design is estimated to have comparable performance to that of other commercial small capacitance devices (<10 F). With further optimization to reduce the mass of the nickel foam and improve graphene performance, capacitance of the cells could also be comparable to higher performance large capacity cells. Thus, the porous graphene electrodes could be ideal for future investigations to focus on the integration of pseudocapacitive materials into the pore structure to significantly boost performance. Alternatively, the conductive pore network would allow the infusion of solid/gel electrolytes deep into the electrode matrix, potentially reducing issues that occur with thick electrodes.

Section 7: Perspectives of Future work

In summary, two different sets of experiments were carried out to explore graphene materials as a carbon material for next generation supercapacitor devices. The primary objective was to investigate the contribution of controlling the unique properties of graphene to enhance performance. The first study focused on the effect of nitrogen functionality on the performance of hydrothermally prepared graphene materials. In depth characterization of the material structure were also carried out. The second study was based upon a review of methods for the preparation of graphene foams, to reduce the loss of surface area achieved by the original exfoliation of graphite to graphene oxide (GO). The main objective was to establish a scalable, foam support for use in future studies involving pseudocapacitive materials.

In the first study, nitrogen doped graphene (NG) was prepared by the introduction of ammonium hydroxide as a precursor during hydrothermal reduction with sodium borohydride. The heteroatom doping is intended to alter the band gap structure of the graphene and increase both conduction and capacitance. The results obtained from the optimized NG130 material, using conductive carbon (KJ600) and polymer binder (Nafion), showed improved capacitance over un-doped graphene prepared by a similar method. The X-ray photoelectron spectroscopy (XPS) study indicated that pyrrolic type nitrogen was dominant in the NG130 sample and responsible for the improved capacitance and charge carrier density.

In the second study, we have synthesized and tested graphene foam prepared by several methods. It was found that in all conditions the stand-alone foams exhibited insufficient conductivity to produce the necessary capacitance. Further, handling and preparing the foams created others challenges that made reproducible and scalable production challenging. Using self-assembly the foam was instead

grown on nickel foam, integrating the electrode and the current collector materials. The integrated Ni/rGO foams were then optimized for performance. The advantages of this method include: low temperature, combination of synthesis and electrode manufacturing process, scalable batch production, high loading, elimination of binder and conductive carbon additives and extensive pore structure for ion transport. SEM analysis revealed the well ordered; dense pore structure of the electrodes, which enabled high capacitance and rate capability.

Based on the findings of these studies, some future directions for supercapacitors concerning graphene foaming and heteroatom functionality can be suggested:

1. Synthesis of heteroatom doped graphene with different nitrogen precursors to further study the effect of different doping configurations. Further investigation could also include the investigation of other heteroatom dopants such as sulfur and phosphorous.
2. Investigation of the effect of varying oxygen reduction of GO to investigate different residual oxygen functionalities and their pseudocapacitive impact on performance of graphene prepared by hydrothermal methods.
3. Synthesis of Ni/rGO electrodes which utilize pre-etched nickel foam to thin the pore walls and decrease inactive mass in the cell
4. Verification of Ni/rGO cells in organic electrolyte and investigation of their performance for solid state or gel electrolytes which exhibit poor performance with thick-film electrodes and could benefit from the extensive pore network of the integrated foam.
5. Synthesize composite rGO foams containing high density and capacitance pseudocapacitive material, integrated within the nickel foam current collector.

References

[1] "Global Greenhouse Gas Emissions Data," *United States EPA*, 2013. [Online]. Available: http://www.epa.gov/climatechange/ghgemissions/global.html. [Accessed: 01-Jul-2013].

[2] H. E. Becker, "Low Voltage Electrolytic Capacitor," 1957.

[3] D. I. Boos and G. Heights, "Electrolytic Capacitor Having Carbon Paste Electrodes," 1970.

[4] A. Davies and A. Yu, "Material advancements in supercapacitors: From activated carbon to carbon nanotube and graphene," *The Canadian Journal of Chemical Engineering*, vol. 89, no. December, pp. 1342–1357, Jun. 2011.

[5] B. E. E. Conway, *Electrochemical Supercapacitors*. New York: Plenum Publishing, 1999.

[6] B. W. Ricketts, "Self-discharge of carbon-based supercapacitors with organic electrolytes," *Journal of Power Sources*, vol. 89, no. 1, pp. 64–69, 2000.

[7] O. Barbieri, M. Hahn, a Herzog, and R. Kotz, "Capacitance limits of high surface area activated carbons for double layer capacitors," *Carbon*, vol. 43, no. 6, pp. 1303–1310, May 2005.

[8] D. Qu and H. Shi, "Studies of activated carbons used in double-layer capacitors," *Journal of Power Sources*, vol. 74, no. 1, pp. 99–107, Jul. 1998.

[9] Y. Kim, Y. Horiea, S. Ozakia, Y. Matsuzawaa, H. Suezakia, C. Kima, N. Miyashitab, and M. Endoa, "Correlation between the pore and solvated ion size on capacitance uptake of PVDC-based carbons," *Carbon*, vol. 42, no. 8–9, pp. 1491–1500, 2004.

[10] J. Chmiola, C. Largeot, P.-L. Taberna, P. Simon, and Y. Gogotsi, “Desolvation of ions in subnanometer pores and its effect on capacitance and double-layer theory.,” *Angewandte Chemie (International ed. in English)*, vol. 47, no. 18, pp. 3392–5, Jan. 2008.

[11] J. Chmiola, G. Yushin, Y. Gogotsi, C. Portet, P. Simon, P. L. Taberna, and C. Protet, “Anomalous increase in carbon capacitance at pore sizes less than 1 nanometer.,” *Science*, vol. 313, no. 5794, pp. 1760–3, Sep. 2006.

[12] C. Largeot, C. Portet, J. Chmiola, P.-L. Taberna, Y. Gogotsi, and P. Simon, “Relation between the ion size and pore size for an electric double layer capacitor,” *J. Am. Chem. Soc.*, vol. 130, no. 9, pp. 2730–2731, 2008.

[13] J. Huang, B. Sumpter, and V. Meunier, “Universal model for nanoporous carbon supercapacitors applicable to diverse pore regimes, carbons, and electrolytes.,” *Chem. Eur. J.*, vol. 14, no. 22, pp. 6614–6626, 2008.

[14] J. Huang, B. Sumpter, and V. Meunier, “Theoretical model for nanoporous carbon supercapacitors,” *Angewandte Chemie (International ed. in English)*, vol. 47, no. 3, pp. 520–524, 2008.

[15] C. Liu, F. Li, L.-P. Ma, and H.-M. Cheng, “Advanced materials for energy storage.,” *Advanced materials (Deerfield Beach, Fla.)*, vol. 22, no. 8, pp. E28–62, Feb. 2010.

[16] P. Simon and Y. Gogotsi, “Materials for electrochemical capacitors.,” *Nature materials*, vol. 7, no. 11, pp. 845–854, Nov. 2008.

[17] D. S. Geng, S. L. Yang, Y. Zhang, J. L. Yang, J. Liu, R. Y. Li, T.-K. K. Sham, X. L. Sun, S. Y. Ye, and S. Knights, “Nitrogen doping effects on the structure of graphene,” *Applied Surface Science*, vol. 257, no. 21, pp. 9193–9198, Aug. 2011.

[18] Z. Lin, Y. Liu, Y. Yao, O. J. Hildreth, Z. Li, K. Moon, J. C. Agar, and C. Wong, “Surface Engineering of Graphene for High Performance Supercapacitors,” *Synthesis*, pp. 236–241, 2011.

[19] G. Pognon, T. Brousse, L. Demarconnay, and D. Bélanger, “Performance and stability of electrochemical capacitor based on anthraquinone modified activated carbon,” *Journal of Power Sources*, vol. 196, no. 8, pp. 4117–4122, Apr. 2011.

[20] Z. Fan, J. Chen, M. Wang, K. Cui, H. Zhou, and Y. Kuang, “Preparation and characterization of manganese oxide/CNT composites as supercapacitive materials,” *Diamond and Related Materials*, vol. 15, no. 9, pp. 1478–1483, Sep. 2006.

[21] G. Gryglewicz, J. Machnikowski, E. Lorencgrabowska, G. Lota, and E. Frackowiak, “Effect of pore size distribution of coal-based activated carbons on double layer capacitance,” *Electrochimica Acta*, vol. 50, no. 5, pp. 1197–1206, Jan. 2005.

[22] E. Frackowiak, “Carbon materials for supercapacitor application.,” *Physical chemistry chemical physics : PCCP*, vol. 9, no. 15, pp. 1774–85, Apr. 2007.

[23] F.-C. Wu, R.-L. Tseng, C.-C. Hu, and C.-C. Wang, “Physical and electrochemical characterization of activated carbons prepared from firwoods for supercapacitors,” *Journal of Power Sources*, vol. 138, no. 1–2, pp. 351–359, Nov. 2004.

[24] X. Wang and D. Wang, “Performance of electric double layer capacitors using active carbons prepared from petroleum coke by KOH and vapor re-etching,” *Journal of Materials Science and Technology*, vol. 19, no. 3, 2003.

[25] P. Smith and T. Jiang, “High Energy Density Ultracapacitors,” 2009.

[26] T. Otowa, R. Tanibata, and M. Itoh, “Production and adsorption characteristics of MAXSORB: high-surface-area active carbon,” *Gas Seperation and Purification*, vol. 7, no. 4, pp. 241–245, 1993.

[27] Z. Wen, Q. Qu, Q. Gao, and X. Zheng, “An activated carbon with high capacitance from carbonization of a resorcinol-formaldehyde resin,” *Electrochemistry Communications*, vol. 11, no. 3, pp. 715–718, 2009.

[28] C. O. Ania, V. Khomenko, E. Raymundo-Piñero, J. B. Parra, and F. Béguin, “The Large Electrochemical Capacitance of Microporous Doped Carbon Obtained by Using a Zeolite Template,” *Advanced Functional Materials*, vol. 17, no. 11, pp. 1828–1836, Jul. 2007.

[29] A. Fuertes, G. Lota, T. Centeno, and E. Frackowiak, “Templated mesoporous carbons for supercapacitor application,” *Electrochimica Acta*, vol. 50, no. 14, pp. 2799–2805, May 2005.

[30] L. L. Zhang and X. S. Zhao, “Carbon-based materials as supercapacitor electrodes.,” *Chem. Soc. Rev.*, vol. 38, no. 9, pp. 2520–31, Sep. 2009.

[31] H. Wang, Q. Gao, J. Hu, and Z. Chen, “High performance of nanoporous carbon in cryogenic hydrogen storage and electrochemical capacitance,” *Carbon*, vol. 47, no. 9, pp. 2259–2268, Aug. 2009.

[32] C. Portet, Z. Yang, Y. Korenblit, Y. Gogotsi, R. Mokaya, and G. Yushin, “Electrical Double-Layer Capacitance of Zeolite-Templated Carbon in Organic Electrolyte,” *Journal of The Electrochemical Society*, vol. 156, no. 1, pp. A1–A6, 2009.

[33] H. Nishihara, H. Itoi, T. Kogure, P.-X. Hou, H. Touhara, F. Okino, and T. Kyotani, “Investigation of the ion storage/transfer behavior in an electrical double-layer capacitor by using ordered microporous carbons as model materials.,” *Chemistry (Weinheim an der Bergstrasse, Germany)*, vol. 15, no. 21, pp. 5355–63, Jan. 2009.

[34] C. Vixguterl, S. Saadallah, K. Jurewicz, E. Frackowiak, M. Reda, J. Parmentier, J. Patarin, and F. Beguin, “Supercapacitor electrodes from new ordered porous carbon materials obtained by a templating procedure,” *Materials Science and Engineering B*, vol. 108, no. 1–2, pp. 148–155, Apr. 2004.

[35] N. D. Kim, W. Kim, J. B. Joo, S. Oh, P. Kim, Y. Kim, and J. Yi, “Electrochemical capacitor performance of N-doped mesoporous carbons prepared by ammoxidation,” *Journal of Power Sources*, vol. 180, no. 1, pp. 671–675, May 2008.

[36] F. Lufrano, P. Staiti, T. Avanzate, and E. Nicola, “Mesoporous Carbon Materials as Electrodes for Electrochemical Supercapacitors,” *Int. J. Electrochem. Sci*, vol. 5, pp. 903 – 916, 2010.

[37] J. S. Beck, K. D. Schmitt, J. B. Higgins, and J. L. Schlenkert, “New Family of Mesoporous Molecular Sieves Prepared with Liquid Crystal Templates,” *Journal of the American Chemical Society*, vol. 114, no. 27, pp. 10834–10843, 1992.

[38] C. Vixguterl, E. Frackowiak, K. Jurewicz, M. Friebe, J. Parmentier, and F. Beguin, “Electrochemical energy storage in ordered porous carbon materials,” *Carbon*, vol. 43, no. 6, pp. 1293–1302, May 2005.

[39] Z. Lei, N. Christov, L. L. Zhang, and X. S. Zhao, “Mesoporous carbon nanospheres with an excellent electrocapacitive performance,” *Journal of Materials Chemistry*, vol. 21, no. 7, p. 2274, 2011.

[40] D. W. Wang, L. Feng, L. Min, Q. G. Lu, and H.-M. Cheng, “A 3D Aperiodic Hierarchical Porous Graphitic Carbon for High Rate,” *Angewandte Chemie (International ed. in English)*, 2007.

[41] D.-W. Wang, F. Li, M. Liu, G. Q. Lu, and H.-M. Cheng, “3D aperiodic hierarchical porous graphitic carbon material for high-rate electrochemical capacitive energy storage.,” *Angewandte Chemie (International ed. in English)*, vol. 47, no. 2, pp. 373–6, Jan. 2008.

[42] L. Hu, J. W. Choi, Y. Yang, S. Jeong, F. La Mantia, L.-F. Cui, and Y. Cui, “Highly conductive paper for energy-storage devices.,” *Proceedings of the National Academy of Sciences of the United States of America*, vol. 106, no. 51, pp. 21490–4, Dec. 2009.

[43] R. Zhou, C. Meng, F. Zhu, Q. Li, C. Liu, S. Fan, and K. Jiang, “High-performance supercapacitors using a nanoporous current collector made from super-aligned carbon nanotubes.,” *Nanotechnology*, vol. 21, no. 34. p. 345701, 27-Aug-2010.

[44] Y. Honda, T. Haramoto, M. Takeshige, H. Shiozaki, T. Kitamura, and M. Ishikawa, “Aligned MWCNT Sheet Electrodes Prepared by Transfer Methodology Providing High-Power

Capacitor Performance," *Electrochemical and Solid-State Letters*, vol. 10, no. 4, pp. A106–A110, 2007.

[45] T. Hasan and V. Scardaci, "Stabilization and 'Debundling' of Single-Wall Carbon Nanotube Dispersions in N-Methyl-2-pyrrolidone (NMP) by Polyvinylpyrrolidone (PVP)," *Journal of Physical Chemistry C*, vol. 111, no. 34, pp. 12594–12602, 2007.

[46] M. Inagaki, H. Konno, and O. Tanaike, "Carbon materials for electrochemical capacitors," *Journal of Power Sources*, vol. 195, no. 24, pp. 7880–7903, Dec. 2010.

[47] K. H. An, W. S. Kim, Y. S. Park, J.-M. M. Moon, D. J. Bae, S. C. Lim, and Y. S. H. S. Lee, "Electrochemical Properties of High-Power Supercapacitors Using Single-Walled Carbon Nanotube Electrodes," *Advanced Functional Materials*, vol. 11, no. 5, pp. 387–392, Oct. 2001.

[48] C. Niu, E. K. Sichel, R. Hoch, D. Moy, and H. Tennent, "High power electrochemical capacitors based on carbon nanotube electrodes," *Applied Physics Letters*, vol. 70, no. 11, p. 1480, 1997.

[49] C. Liu, "The electrochemical capacitance charactersitics of activated carbon electrode material with a multi-walled carbon nanotube additive," *New Carbon Materials*, vol. 20, no. 3, pp. 205–210, 2005.

[50] T. Hiraoka, A. Izadi-Najafabadi, T. Yamada, D. N. Futaba, S. Yasuda, O. Tanaike, H. Hatori, M. Yumura, S. Iijima, and K. Hata, "Compact and Light Supercapacitor Electrodes from a Surface-Only Solid by Opened Carbon Nanotubes with 2 200 m 2 g −1 Surface Area," *Advanced Functional Materials*, vol. 20, no. 3, pp. 422–428, Feb. 2010.

[51] V. Obreja, “On the performance of supercapacitors with electrodes based on carbon nanotubes and carbon activated material—A review,” *Physica E: Low-dimensional Systems and Nanostructures*, vol. 40, no. 7, pp. 2596–2605, May 2008.

[52] C. N. R. Rao, a K. Sood, K. S. Subrahmanyam, and A. Govindaraj, “Graphene: the new two-dimensional nanomaterial.,” *Angew. Chem. Int. Ed.*, vol. 48, no. 42, pp. 7752–7777, Jan. 2009.

[53] S. Park and R. S. Ruoff, “Chemical methods for the production of graphenes.,” *Nat. Nanotechnol.*, vol. 4, no. 4, pp. 217–224, Apr. 2009.

[54] Y. Wang, Y. Wu, Y. Huang, F. Zhang, X. Yang, Y. Ma, and Y. Chen, “Preventing Graphene Sheets from Restacking for High-Capacitance Performance,” *J. Phys. Chem. C*, vol. 115, no. 46, pp. 23192–23197, Nov. 2011.

[55] S. Stankovich, D. A. Dikin, R. D. Piner, K. A. Kohlhaas, A. Kleinhammes, Y. Jia, Y. Wu, S. T. Nguyen, and R. S. Ruoff, “Synthesis of graphene-based nanosheets via chemical reduction of exfoliated graphite oxide,” *Carbon*, vol. 45, no. 7, pp. 1558–1565, Jun. 2007.

[56] M. D. Stoller, S. Park, Y. Zhu, J. An, and R. S. Ruoff, “Graphene-based ultracapacitors.,” *Nano Lett.*, vol. 8, no. 10, pp. 3498–502, Oct. 2008.

[57] Y. Zhu, S. Murali, M. D. Stoller, K. J. Ganesh, W. Cai, P. J. Ferreira, A. Pirkle, R. M. Wallace, K. a Cychosz, M. Thommes, D. Su, E. a Stach, and R. S. Ruoff, “Carbon-Based Supercapacitors Produced by Activation of Graphene,” *Science*, vol. 332, no. 6037, pp. 1537–1541, May 2011.

[58] Y. Wang, Z. Shi, Y. Huang, Y. Ma, C. Wang, M. Chen, and Y. Chen, “Supercapacitor Devices Based on Graphene Materials,” *J. Phys. Chem. C*, vol. 113, no. 30, pp. 13103–13107, Jul. 2009.

[59] A. P. Yu, I. Roes, A. Davies, and Z. W. Chen, “Ultrathin, transparent, and flexible graphene films for supercapacitor application,” *App. Phys. Lett.*, vol. 96, no. 25, p. 253105, 2010.

[60] L. L. Zhang, X. Zhao, H. Ji, M. D. Stoller, L. Lai, S. Murali, S. Mcdonnell, B. Cleveger, R. M. Wallace, and R. S. Ruoff, “Nitrogen doping of graphene and its effect on quantum capacitance, and a new insight on the enhanced capacitance of N-doped carbon,” *Energy Environ. Sci.*, vol. 5, no. 11, pp. 9618–9625, 2012.

[61] H. M. Jeong, J. W. Lee, W. H. Shin, Y. J. Choi, H. J. Shin, J. K. Kang, and J. W. Choi, “Nitrogen-doped graphene for high-performance ultracapacitors and the importance of nitrogen-doped sites at Basal planes.,” *Nano Lett.*, vol. 11, no. 6, pp. 2472–7, Jun. 2011.

[62] K. Moskvitch, “Ultrashort laser pulses squeezed out of graphene,” *Nature News*, 2013.

[63] X. Yang, J. Zhu, L. Qiu, and D. Li, “Bioinspired effective prevention of restacking in multilayered graphene films: towards the next generation of high-performance supercapacitors,” *Advanced materials (Deerfield Beach, Fla.)*, vol. 23, no. 25, pp. 2833–8, Jul. 2011.

[64] X. Sun, G. Wang, J.-Y. Hwang, and J. Lian, “Porous nickel oxide nano-sheets for high performance pseudocapacitance materials,” *J. Mater. Chem.*, vol. 21, no. 41, p. 16581, 2011.

[65] W. Hong, Y. Xu, G. Lu, C. Li, and G. Shi, “Transparent graphene/PEDOT–PSS composite films as counter electrodes of dye-sensitized solar cells,” *Electrochem. Commun.*, vol. 10, no. 10, pp. 1555–1558, Oct. 2008.

[66] Y. Wang, A. Yuan, and X. Wang, “Pseudocapacitive behaviors of nanostructured manganese dioxide/carbon nanotubes composite electrodes in mild aqueous electrolytes: effects of electrolytes and current collectors,” *J Solid State Electrochem.*, vol. 12, no. 9, pp. 1101–1107, Oct. 2007.

[67] I.-H. Kim, J.-H. Kim, B.-W. Cho, and K.-B. Kim, “Pseudocapacitive Properties of Electrochemically Prepared Vanadium Oxide on Carbon Nanotube Film Substrate,” *Journal of The Electrochemical Society*, vol. 153, no. 8, p. A1451, 2006.

[68] X. Xia, J. Tu, Y. Mai, R. Chen, X. Wang, C. Gu, and X. Zhao, “Graphene Sheet/Porous NiO Hybrid Film for Supercapacitor Applications.,” *Chem. Eur. J.*, vol. 17, no. 39, pp. 10898–10905, Aug. 2011.

[69] S. Biswas and L. T. Drzal, “Multilayered Nanoarchitecture of Graphene Nanosheets and Polypyrrole Nanowires for High Performance Supercapacitor Electrodes,” *Chem. Mater.*, vol. 22, no. 20, pp. 5667–5671, Oct. 2010.

[70] S. Sivakkumar, J. Ko, D. Kim, B. Kim, and G. Wallace, “Performance evaluation of CNT/polypyrrole/MnO2 composite electrodes for electrochemical capacitors,” *Electrochimica Acta*, vol. 52, no. 25, pp. 7377–7385, Sep. 2007.

[71] X. Wang, D. Ruan, P. Wang, and Y. Lu, “Pseudo-capacitance of ruthenium oxide/carbon black composites for electrochemical capacitors,” *Journal of University of Science and Technology Beijing, Mineral, Metallurgy, Material*, vol. 15, no. 6, pp. 816–821, Dec. 2008.

[72] A. Yu, V. Chabot, and J. Zhang, *Electrochemical Supercapacitors for Energy Storage and Delivery*. New York: CRC Press, 2013, p. 348.

[73] B. E. Conway and W. G. Pell, “Double-layer and pseudocapacitance types of electrochemical capacitors and their applications to the development of hybrid devices,” *Journal of Solid State Electrochemistry*, vol. 7, no. 9, pp. 637–644, Sep. 2003.

[74] B. E. Conway, V. Birss, and J. Wojtowicz, “The role and utilization of pseudocapacitance for energy storage by supercapacitors,” *J. Power Sources*, vol. 66, no. 1–2, pp. 1–14, May 1997.

[75] A. Burke and M. Miller, “The power capability of ultracapacitors and lithium batteries for electric and hybrid vehicle applications,” *Journal of Power Sources*, vol. 196, no. 1, pp. 514–522, Jan. 2011.

[76] C. Meng, C. Liu, L. Chen, C. Hu, and S. Fan, “Highly flexible and all-solid-state paperlike polymer supercapacitors.,” *Nano letters*, vol. 10, no. 10, pp. 4025–31, Oct. 2010.

[77] X. Yang, F. Zhang, L. Zhang, T. Zhang, Y. Huang, and Y. Chen, “A High-Performance Graphene Oxide-Doped Ion Gel as Gel Polymer Electrolyte for All-Solid-State Supercapacitor Applications,” *Advanced Functional Materials*, vol. 23, no. 26, pp. 3353–3360, 2013.

[78] A. Lewandowski, M. Zajder, E. Frąckowiak1, and F. Béguin, “Supercapacitor based on activated carbon and polyethylene oxide–KOH–H2O polymer electrolyte,” *Electrochimica Acta*, vol. 46, no. 18, pp. 2777–2780, May 2001.

[79] A. Lewandowski, A. Olejniczak, M. Galinski, and I. Stepniak, “Performance of carbon–carbon supercapacitors based on organic, aqueous and ionic liquid electrolytes,” *Journal of Power Sources*, vol. 195, no. 17, pp. 5814–5819, Sep. 2010.

[80] C. Liu, Z. Yu, D. Neff, A. Zhamu, and B. Z. Jang, “Graphene-Based Supercapacitor with an Ultrahigh Energy Density.,” *Nano Lett.*, vol. 10, pp. 4863–4868, Nov. 2010.

[81] S. A. Hashmi, “Ionic liquid incorporated polymer electrolytes for supercapacitor application,” *Indian Journal of Chemistry*, vol. 49, pp. 743–751.

[82] X. Xiao, P. Liu, J. S. Wang, M. W. Verbrugge, and M. P. Balogh, “Vertically aligned graphene electrode for lithium ion battery with high rate capability,” *Electrochem. Commun.*, vol. 13, no. 2, pp. 209–212, Feb. 2011.

[83] N. Li, Z. Chen, W. Ren, F. Li, and H.-M. Cheng, “Flexible graphene-based lithium ion batteries with ultrafast charge and discharge rates.,” *Proc. Natl. Acad. Sci. U.S.A*, vol. 109, no. 43, pp. 17360–5, Oct. 2012.

[84] H. Ji, L. Zhang, M. Pettes, H. Li, and S. Chen, “Ultrathin graphite foam: A three-dimensional conductive network for battery electrodes,” *Nano Lett.*, vol. 12, pp. 2446–2451, 2012.

[85] X. Dong, X. Wang, J. Wang, H. Song, X. Li, L. Wang, M. B. Chan-Park, C. M. Li, and P. Chen, “Synthesis of a MnO2–graphene foam hybrid with controlled MnO2 particle shape and its use as a supercapacitor electrode,” *Carbon*, vol. 50, no. 13, pp. 4865–4870, Nov. 2012.

[86] X. Cao, Y. Shi, W. Shi, G. Lu, X. Huang, Q. Yan, Q. Zhang, and H. Zhang, “Preparation of novel 3D graphene networks for supercapacitor applications.,” *Small*, vol. 7, no. 22, pp. 3163–8, Nov. 2011.

[87] W. Wang, S. Guo, M. Penchev, I. Ruiz, K. N. Bozhilov, D. Yan, M. Ozkan, and C. S. Ozkan, "Three dimensional few layer graphene and carbon nanotube foam architectures for high fidelity supercapacitors," *Nano Energy*, vol. 2, no. 2, pp. 294–303, Oct. 2013.

[88] L. Ren, K. S. Hui, and K. N. Hui, "Self-assembled free-standing three-dimensional nickel nanoparticle/graphene aerogel for direct ethanol fuel cells," *J. Mater. Chem. A*, vol. 1, pp. 5689–5694, 2013.

[89] Z.-S. Wu, S. Yang, Y. Sun, K. Parvez, X. Feng, and K. Müllen, "3D nitrogen-doped graphene aerogel-supported Fe3O4 nanoparticles as efficient electrocatalysts for the oxygen reduction reaction.," *J. Am. Chem. Soc.*, vol. 134, no. 22, pp. 9082–5, Jun. 2012.

[90] Z.-L. Wang, D. Xu, J.-J. Xu, L.-L. Zhang, and X.-B. Zhang, "Graphene Oxide Gel-Derived, Free-Standing, Hierarchically Porous Carbon for High-Capacity and High-Rate Rechargeable Li-O2 Batteries," *Adv. Funct. Mater.*, vol. 22, no. 17, pp. 3699–3705, Sep. 2012.

[91] L. Xiao, D. Wu, S. Han, Y. Huang, S. Li, M. He, F. Zhang, and X. Feng, "Self-Assembled Fe2O3/Graphene Aerogel with High Lithium Storage Performance.," *ACS Appl. Mater. Interfaces*, vol. 5, no. 9, pp. 3764–3769, Apr. 2013.

[92] W. Chen, S. Li, C. Chen, and L. Yan, "Self-assembly and embedding of nanoparticles by in situ reduced graphene for preparation of a 3D graphene/nanoparticle aerogel.," *Adv. Mater.*, vol. 23, no. 47, pp. 5679–83, Dec. 2011.

[93] S. Yang, Y. Gong, Z. Liu, L. Zhan, D. P. Hashim, L. Ma, R. Vajtai, and P. M. Ajayan, "Bottom-up Approach toward Single-Crystalline VO2-Graphene Ribbons as Cathodes for Ultrafast Lithium Storage.," *Nano Lett.*, vol. 13, no. 4, pp. 1596–601, Apr. 2013.

[94] Y. Xu, K. Sheng, C. Li, and G. Shi, “Self-Assembled Graphene Hydrogel via a One-Step Hydrothermal Process,” *ACS Nano*, vol. 4, no. 7, pp. 4324–4330, 2010.

[95] X. Zhang, Z. Sui, B. Xu, S. Yue, Y. Luo, W. Zhan, and B. Liu, “Mechanically strong and highly conductive graphene aerogel and its use as electrodes for electrochemical power sources,” *J. Mater. Chem.*, vol. 21, no. 18, p. 6494, 2011.

[96] Y. Zhao, J. Liu, Y. Hu, H. Cheng, C. Hu, C. Jiang, L. Jiang, A. Cao, and L. Qu, “Highly Compression-Tolerant Supercapacitor Based on Polypyrrole-mediated Graphene Foam Electrodes.,” *Adv. Mater.*, vol. 25, pp. 591–595, Oct. 2012.

[97] Z.-S. Wu, A. Winter, L. Chen, Y. Sun, A. Turchanin, X. Feng, and K. Müllen, “Three-Dimensional Nitrogen and Boron Co-doped Graphene for High-Performance All-Solid-State Supercapacitors.,” *Adv. Mater.*, vol. 24, no. 37, pp. 5130–5, Sep. 2012.

[98] Y. Zhao, C. Hu, Y. Hu, H. Cheng, G. Shi, and L. Qu, “A versatile, ultralight, nitrogen-doped graphene framework.,” *Angew. Chem. Int. Ed.*, vol. 51, no. 45, pp. 11371–5, Nov. 2012.

[99] J. Chen, K. Sheng, P. Luo, C. Li, and G. Shi, “Graphene hydrogels deposited in nickel foams for high-rate electrochemical capacitors.,” *Adv. Mater.*, vol. 24, no. 33, pp. 4569–73, Aug. 2012.

[100] L. Zhang and G. Shi, “Preparation of Highly Conductive Graphene Hydrogels for Fabricating Supercapacitors with High Rate Capability,” *J. Phys. Chem. C*, vol. 115, no. 34, pp. 17206–17212, Sep. 2011.

[101] V. H. Luan, H. N. Tien, L. T. Hoa, N. T. M. Hien, E.-S. Oh, J. Chung, E. J. Kim, W. M. Choi, B.-S. Kong, and S. H. Hur, "Synthesis of a highly conductive and large surface area graphene oxide hydrogel and its use in a supercapacitor," *J. Mater. Chem. A*, vol. 1, no. 2, p. 208, 2013.

[102] A. C. Pierre and G. M. Pajonk, "Chemistry of aerogels and their applications.," *Chem. Rev.*, vol. 102, no. 11, pp. 4243–65, Nov. 2002.

[103] M. J. Pikal and S. Shah, "The collapse temperature in freeze drying: Dependence on measurement methodology and rate of water removal from the glassy phase," *Int. J. Pharm.*, vol. 62, no. 2–3, pp. 165–186, Jul. 1990.

[104] C. J. King and J. Bellows, "Freeze-Drying of Aqueoue Allowable Operating Solutions : Maximum Temperature," *Cryobiology*, vol. 561, pp. 559–561, 1972.

[105] L. Qiu, J. Z. Liu, S. L. Y. Chang, Y. Wu, and D. Li, "Biomimetic superelastic graphene-based cellular monoliths," *Nat. Commun.*, vol. 3, p. 1241, Dec. 2012.

[106] M. a Worsley, P. J. Pauzauskie, T. Y. Olson, J. Biener, J. H. Satcher, and T. F. Baumann, "Synthesis of graphene aerogel with high electrical conductivity.," *J. Am. Chem. Soc.*, vol. 132, no. 40, pp. 14067–9, Oct. 2010.

[107] M. Worsley, T. Olson, and J. Lee, "High surface area, sp2-cross-linked three-dimensional graphene monoliths," *J. Phys. Chem. Lett.*, vol. 2, pp. 921–925, 2011.

[108] "Phase change data for Carbon dioxide," *National Institute of Standards and Technology*. [Online]. Available: http://webbook.nist.gov/cgi/cbook.cgi?ID=C124389&Units=SI&Mask=4#Thermo-Phase. [Accessed: 20-Mar-2013].

[109] “Phase change data for Water,” *National Institute of Standards and Technology*. [Online]. Available: http://webbook.nist.gov/cgi/cbook.cgi?ID=C7732185&Mask=4#Thermo-Phase. [Accessed: 25-Mar-2013].

[110] W. S. Hummers and R. E. Offeman, “Preparation of graphitic oxide,” *J. Am. Chem. Soc.*, vol. 80, no. 6, p. 1339, 1958.

[111] D. C. Marcano, D. V Kosynkin, J. M. Berlin, A. Sinitskii, Z. Sun, A. Slesarev, L. B. Alemany, W. Lu, and J. M. Tour, “Improved synthesis of graphene oxide.,” *ACS Nano*, vol. 4, no. 8, pp. 4806–14, Aug. 2010.

[112] K. R. Koch, “Oxidation by Mn207: An impressive demonstration of the powerful oxidizing property of dimanganeseheptoxide,” *J. Chem. Educ.*, vol. 59, no. 11, pp. 973–974, 1982.

[113] S. Pei, J. Zhao, J. Du, W. Ren, and H.-M. Cheng, “Direct reduction of graphene oxide films into highly conductive and flexible graphene films by hydrohalic acids,” *Carbon*, vol. 48, no. 15, pp. 4466–4474, Dec. 2010.

[114] D. R. Dreyer, S. Park, C. W. Bielawski, and R. S. Ruoff, “The chemistry of graphene oxide.,” *Chem. Soc. Rev.*, vol. 39, no. 1, pp. 228–40, Jan. 2010.

[115] H. He, J. Klinowski, M. Forster, and A. Lerf, “A new structural model for graphite oxide,” *Chem. Phys. Lett.*, vol. 287, no. 1–2, pp. 53–56, 1998.

[116] J. Kim, L. J. Cote, F. Kim, W. Yuan, K. R. Shull, and J. Huang, “Graphene oxide sheets at interfaces.,” *J. Am. Chem. Soc.*, vol. 132, no. 23, pp. 8180–6, Jun. 2010.

[117] P. Guo, H. Song, and X. Chen, “Hollow graphene oxide spheres self-assembled by W/O emulsion,” *J. Mater. Chem.*, vol. 20, no. 23, p. 4867, 2010.

[118] Y. Xue, J. Liu, H. Chen, R. Wang, D. Li, J. Qu, and L. Dai, “Nitrogen-Doped Graphene Foams as Metal-Free Counter Electrodes in High-Performance Dye-Sensitized Solar Cells,” *Angew. Chem. Int. Ed.*, vol. 51, pp. 12124–12127, Nov. 2012.

[119] Y. Long, C. Zhang, X. Wang, J. Gao, W. Wang, and Y. Liu, “Oxidation of SO2 to SO3 catalyzed by graphene oxide foams,” *J. Mater. Chem.*, vol. 21, no. 36, p. 13934, 2011.

[120] Y. Lin, G. J. Ehlert, C. Bukowsky, and H. A. Sodano, “Superhydrophobic functionalized graphene aerogels.,” *ACS Appl. Mater. Interfaces*, vol. 3, no. 7, pp. 2200–3, Jul. 2011.

[121] X. Zhou and Z. Liu, “A scalable, solution-phase processing route to graphene oxide and graphene ultralarge sheets.,” *Chem. Commun.*, vol. 46, no. 15, pp. 2611–3, Apr. 2010.

[122] X. Mi, G. Huang, W. Xie, W. Wang, Y. Liu, and J. Gao, “Preparation of graphene oxide aerogel and its adsorption for Cu2+ ions,” *Carbon*, vol. 50, no. 13, pp. 4856–4864, Nov. 2012.

[123] H.-J. Shin, K. K. Kim, A. Benayad, S.-M. Yoon, H. K. Park, I.-S. Jung, M. H. Jin, H.-K. Jeong, J. M. Kim, J.-Y. Choi, and Y. H. Lee, “Efficient reduction of graphite oxide by sodium borohydride and its effect on electrical conductance,” *Adv. Funct. Mater.*, vol. 19, no. 12, pp. 1987–1992, Jun. 2009.

[124] M. Fernandez-Merino, L. Guardia, J. I. Paredes, P. Villar-Rodil, P. Solis-Fernandez, A. Martinez-Alonso, and J. M. D. Tascon, “Vitamin C is an ideal substitute for hydrazine in the reduction of graphene oxide suspensions,” *J. Phys. Chem. C*, vol. 114, no. 14, pp. 6426–6432, 2010.

[125] J. J. Yoo, K. Balakrishnan, J. Huang, V. Meunier, B. G. Sumpter, A. Srivastava, M. Conway, A. L. M. Reddy, J. Yu, R. Vajtai, and P. M. Ajayan, "Ultrathin planar graphene supercapacitors.," *Nano Lett.*, vol. 11, no. 4, pp. 1423–7, Apr. 2011.

[126] Z. Niu, J. Chen, H. H. Hng, J. Ma, and X. Chen, "A leavening strategy to prepare reduced graphene oxide foams.," *Adv. Mater.*, vol. 24, no. 30, pp. 4144–50, Aug. 2012.

[127] H. B. Wang, T. Maiyalagan, and X. Wang, "Review on Recent Progress in Nitrogen-Doped Graphene: Synthesis, Characterization, and Its Potential Applications," *ACS Catal.*, vol. 2, no. 5, pp. 781–794, May 2012.

[128] L. Qu, Y. Liu, J.-B. Baek, and L. Dai, "Nitrogen-doped graphene as efficient metal-free electrocatalyst for oxygen reduction in fuel cells.," *ACS Nano*, vol. 4, no. 3, pp. 1321–6, Mar. 2010.

[129] H. Bai, C. Li, X. Wang, and G. Shi, "On the Gelation of Graphene Oxide," *J. Phys. Chem. C*, vol. 115, no. 13, pp. 5545–5551, Apr. 2011.

[130] S. Pan and I. A. Aksay, "Factors controlling the size of graphene oxide sheets produced via the graphite oxide route.," *ACS Nano*, vol. 5, no. 5, pp. 4073–83, May 2011.

[131] S. Park, K. Lee, G. Bozoklu, and W. Cai, "Graphene oxide papers modified by divalent ions—Enhancing mechanical properties via chemical cross-linking," *ACS Nano*, vol. 2, no. 3, 2008.

[132] H. Sun, Z. Xu, and C. Gao, "Multifunctional, Ultra-Flyweight, Synergistically Assembled Carbon Aerogels.," *Adv. Mater.*, vol. 25, no. 18, pp. 2554–2560, Feb. 2013.

[133] Z. Xu, H. Sun, X. Zhao, and C. Gao, “Ultrastrong fibers assembled from giant graphene oxide sheets.,” *Adv. Mater.*, vol. 25, no. 2, pp. 188–93, Jan. 2013.

[134] J. Zhao, W. Ren, and H.-M. Cheng, “Graphene sponge for efficient and repeatable adsorption and desorption of water contaminations,” *J. Mater. Chem.*, vol. 22, no. 38, p. 20197, 2012.

[135] H. Hu, Z. Zhao, W. Wan, Y. Gogotsi, and J. Qiu, “Ultralight and Highly Compressible Graphene Aerogels.,” *Adv. Mater.*, vol. 25, no. 15, pp. 1–5, Feb. 2013.

[136] J. Che, L. Shen, and Y. Xiao, “A new approach to fabricate graphene nanosheets in organic medium: combination of reduction and dispersion,” *J. Mater. Chem.*, vol. 20, no. 9, p. 1722, 2010.

[137] J. Xia, F. Chen, J. Li, and N. Tao, “Measurement of the quantum capacitance of graphene.,” *Nat. Nanotechnol.*, vol. 4, no. 8, pp. 505–9, Aug. 2009.

[138] C.-C. Hu and W.-C. Chen, “Effects of substrates on the capacitive performance of RuO x · nH 2 O and activated carbon – RuO x electrodes for supercapacitors,” *Electrochim. Acta*, vol. 49, no. 21, pp. 3469–3477, Sep. 2004.

[139] G. Yu, L. Hu, M. Vosgueritchian, H. Wang, X. Xie, J. R. Mcdonough, X. Cui, Y. Cui, and Z. Bao, “Solution-Processed Graphene/MnO 2 Nanostructured Textiles for High-Performance Electrochemical Capacitors,” *Nano Lett.*, pp. 6–12, 2011.

[140] Y. He, W. Chen, X. Li, Z. Zhang, J. Fu, C. Zhao, and E. Xie, “Freestanding Three-Dimensional Graphene/MnO2 Composite Networks As Ultralight and Flexible Supercapacitor Electrodes,” *ACS Nano*, vol. 7, no. 1, pp. 174–182, 2013.

[141] X. Dong, Y. Cao, J. Wang, M. B. Chan-Park, L. Wang, W. Huang, and P. Chen, “Hybrid structure of zinc oxide nanorods and three dimensional graphene foam for supercapacitor and electrochemical sensor applications,” *RSC Adv.*, vol. 2, no. 10, p. 4364, 2012.

[142] X.-C. Dong, H. Xu, X.-W. Wang, Y.-X. Huang, M. B. Chan-Park, H. Zhang, L.-H. Wang, W. Huang, and P. Chen, “3D graphene-cobalt oxide electrode for high-performance supercapacitor and enzymeless glucose detection.,” *ACS Nano*, vol. 6, no. 4, pp. 3206–13, Apr. 2012.

[143] Z.-S. Wu, D.-W. Wang, W. Ren, J. Zhao, G. Zhou, F. Li, and H.-M. Cheng, “Anchoring Hydrous RuO2 on Graphene Sheets for High-Performance Electrochemical Capacitors,” *Adv. Funct. Mater.*, vol. 20, no. 20, pp. 3595–3602, Oct. 2010.

[144] W. Zhou and Z. L. Wang, *Scanning Microscopy for Nanotechnology - Techniques and Applications*. Verlag: Springer, 2006, pp. 1–32.

[145] O. C. Wells and S. S., “Scanning Electron Microscopy,” 1974. [Online]. Available: http://serc.carleton.edu/research_education/geochemsheets/techniques/SEM.html. [Accessed: 27-Mar-2012].

[146] J. Goldstein, D. Newbury, D. Joy, C. Lyman, and P. Echlin, *Scanning Electron Microscopy and X-ray Microanalysis*, 3rd ed. New York: Kluwer Academic/Plenum, 2002.

[147] D. B. Williams and C. B. Carter, *Tranmission Electron Microscpy - A Textbook for Materials Science*. New York: Springer, p. 141.

[148] L. V. Azaroff, R. Kaplow, N. Kato, R. J. Weiss, A. Wilson, and R. Young, *X-ray Diffraction*. New York: McGraw-Hill, 1974.

[149] “Introduction to X-ray Diffraction.” [Online]. Available: http://www.mrl.ucsb.edu/mrl/centralfacilities/xray/xray-basics/index.html. [Accessed: 20-Mar-2012].

[150] C. M. Clark and B. L. Dutrow, “X-ray Powder Diffraction.” [Online]. Available: http://serc.carleton.edu/research_education/geochemsheets/techniques/XRD.html. [Accessed: 20-Mar-2012].

[151] L. Vandier, “X-Ray Diffraction Laboratory.” [Online]. Available: http://www.lcc-toulouse.fr/lcc/spip.php?article120. [Accessed: 28-Mar-2012].

[152] J. I. Langford and A. J. C. Wilson, “Scherrer after 60 Years - Survey and Some New Results in Determination of Crystallite Size,” *Journal of Applied Crystallography*, vol. 11, no. Apr, pp. 102–113, 1978.

[153] “X-ray Photoelectron Specscopy,” *PHysical Electronics - A Division of ULCVAC-PHI*. [Online]. Available: http://www.phi.com/surface-analysis-techniques/xps.html. [Accessed: 27-Mar-2012].

[154] D. R. Vij, *Handbook of Applied Solid State Spectroscopy*. New York: Springer, p. 485.

[155] J. Hollander and M. Jolly, “X-ray Photoelectron Spectroscopy,” *Accounts of Chemical Research*, vol. 3, no. 6, pp. 193–200, 1970.

[156] “Raman Spectroscopy Basics,” *Princeton Instruments*. [Online]. Available: http://content.piacton.com/Uploads/Princeton/Documents/Library/UpdatedLibrary/Raman_Spectroscopy_Basics.pdf. [Accessed: 30-Mar-2012].

[157] D. J. Gardiner, *Practical Raman Spectroscopy*. Springer - Verlag, 1989.

[158] A. C. Ferrari, J. C. Meyer, V. Scardaci, C. Casiraghi, M. Lazzeri, F. Mauri, S. Piscanec, D. Jiang, K. S. Novoselov, S. Roth, and a. K. Geim, "Raman spectrum of graphene and graphene layers," *Phys. Rev. Lett.*, vol. 97, p. 187401, Oct. 2006.

[159] V. Khomenko, E. Frackowiak, and F. Beguin, "Determination of the specific capacitance of conducting polymer/nanotubes composite electrodes using different cell configurations," *Electrochimica Acta*, vol. 50, no. 12, pp. 2499–2506, Apr. 2005.

[160] M. D. Stoller and R. S. Ruoff, "Best practice methods for determining an electrode material's performance for ultracapacitors," *Energy & Environmental Science*, vol. 3, no. 9, pp. 1294–1301, 2010.

[161] K.-C. Tsay, L. Zhang, and J. Zhang, "Effects of electrode layer composition/thickness and electrolyte concentration on both specific capacitance and energy density of supercapacitor," *Electrochimica Acta*, vol. 60, pp. 428–436, Jan. 2012.

[162] C. Merlet, B. Rotenberg, P. A. Madden, P.-L. Taberna, P. Simon, Y. Gogotsi, and M. Salanne, "On the molecular origin of supercapacitance in nanoporous carbon electrodes," *Nat Mater*, vol. 11, no. 4, pp. 306–310, 2012.

[163] J. R. Miller and P. Simon, "Electrochemical Capacitors for Energy Management," *Science*, vol. 321, no. 5889, pp. 651–652, 2008.

[164] A. G. Pandolfo and A. F. Hollenkamp, "Carbon properties and their role in supercapacitors," *Journal of Power Sources*, vol. 157, no. 1, pp. 11–27, Jun. 2006.

[165] D. N. Futaba, K. Hata, T. Yamada, T. Hiraoka, Y. Hayamizu, Y. Kakudate, O. Tanaike, H. Hatori, M. Yumura, and S. Iijima, “Shape-engineerable and highly densely packed single-walled carbon nanotubes and their application as super-capacitor electrodes.,” *Nature materials*, vol. 5, no. 12, pp. 987–94, Dec. 2006.

[166] TalapatraS, KarS, S. K. Pal, VajtaiR, CiL, VictorP, M. M. Shaijumon, KaurS, NalamasuO, and P. M. Ajayan, “Direct growth of aligned carbon nanotubes on bulk metals,” *Nat Nano*, vol. 1, no. 2, pp. 112–116, 2006.

[167] M. M. Shaijumon, F. S. Ou, L. Ci, and P. M. Ajayan, “Synthesis of hybrid nanowire arrays and their application as high power supercapacitor electrodes,” *Chemical Communications*, no. 20, pp. 2373–2375, 2008.

[168] M. Toupin, T. Brousse, D. Belanger, and D. Bélanger, “Charge Storage Mechanism of MnO2 Electrode Used in Aqueous Electrochemical Capacitor,” *Chem. Mater.*, vol. 16, pp. 3184–3190, 2004.

[169] W. Sugimoto, H. Iwata, Y. Yasunaga, Y. Murakami, and Y. Takasu, “Preparation of Ruthenic Acid Nanosheets and Utilization of Its Interlayer Surface for Electrochemical Energy Storage,” *Angewandte Chemie International Edition*, vol. 42, no. 34, pp. 4092–4096, 2003.

[170] J. M. M. Miller, B. Dunn, T. D. Tran, and R. W. Pekala, “Deposition of Ruthenium Nanoparticles on Carbon Aerogels for High Energy Density Supercapacitor Electrodes,” *Journal of the Electrochemical Society*, vol. 144, no. 12, pp. 309–311, 1998.

[171] A. Rudge, J. Davey, I. Raistrick, S. Gottesfeld, and J. P. Ferraris, “Conducting polymers as active materials in electrochemical capacitors,” *Journal of Power Sources*, vol. 47, no. 1–2, pp. 89–107, 1994.

[172] D. S. L. Abergel, V. Apalkov, J. Berashevich, K. Ziegler, and T. Chakraborty, “Properties of graphene: a theoretical perspective,” *Advances in Physics*, vol. 59, no. 4, pp. 261–482, 2010.

[173] V. Singh, D. Joung, L. Zhai, S. Das, S. I. Khondaker, and S. Seal, “Graphene based materials: past, present and future,” *Progress in Materials Science*, vol. 56, no. 8, pp. 1178–1271, Oct. 2011.

[174] H. A. Becerril, J. Mao, Z. Liu, R. M. Stoltenberg, Z. Bao, and Y. Chen, “Evaluation of solution-processed reduced graphene oxide films as transparent conductors.,” *ACS nano*, vol. 2, no. 3, pp. 463–470, Mar. 2008.

[175] S. Stankovich, D. A. Dikin, G. H. B. Dommett, K. M. Kohlhaas, E. J. Zimney, E. A. Stach, R. D. Piner, S. T. Nguyen, and R. S. Ruoff, “Graphene-based composite materials,” *Nature*, vol. 442, no. 7100, pp. 282–286, 2006.

[176] Z. Chen, A. P. Yu, R. Ahmed, H. J. Wang, H. Li, and Z. W. Chen, “Manganese dioxide nanotube and nitrogen-doped carbon nanotube based composite bifunctional catalyst for rechargeable zinc-air battery,” *Electrochimica Acta*, vol. 69, pp. 295–300, 2012.

[177] D. Higgins, Z. Chen, and Z. W. Chen, “Nitrogen doped carbon nanotubes synthesized from aliphatic diamines for oxygen reduction reaction,” *Electrochimica Acta*, vol. 56, no. 3, pp. 1570–1575, 2011.

[178] D. C. Higgins, D. Meza, and Z. W. Chen, “Nitrogen-Doped Carbon Nanotubes as Platinum Catalyst Supports for Oxygen Reduction Reaction in Proton Exchange Membrane Fuel Cells,” *Journal of Physical Chemistry C*, vol. 114, no. 50, pp. 21982–21988, 2010.

[179] Y. L. Li, J. J. Wang, X. F. Li, D. S. Geng, M. N. Banis, R. Y. Li, and X. L. Sun, “Nitrogen-doped graphene nanosheets as cathode materials with excellent electrocatalytic activity for high capacity lithium-oxygen batteries,” *Electrochemistry Communications*, vol. 18, pp. 12–15, 2012.

[180] L. Guan, L. Cui, K. Lin, Y. Y. Wang, X. T. Wang, F. M. Jin, F. He, X. P. Chen, and S. Cui, “Preparation of few-layer nitrogen-doped graphene nanosheets by DC arc discharge under nitrogen atmosphere of high temperature,” *Applied Physics a-Materials Science & Processing*, vol. 102, no. 2, pp. 289–294, 2011.

[181] P. H. Matter, L. Zhang, and U. S. Ozkan, “The role of nanostructure in nitrogen-containing carbon catalysts for the oxygen reduction reaction,” *Journal of Catalysis*, vol. 239, no. 1, pp. 83–96, 2006.

[182] F. M. Hassan, V. Chabot, J. Li, B. K. Kim, L. Ricardez-Sandoval, and A. Yu, “Pyrrolic-structure enriched nitrogen doped graphene for highly efficient next generation supercapacitors,” *J. Mater. Chem. A*, vol. 1, no. 8, pp. 2904–2912, 2013.

[183] V. Chabot, F. Hassan, and A. Yu, “Nitrogen Doped Graphene as a high efficient electrode for next generation supercapacitors,” *ECS Transactions*, vol. 50, no. 43, pp. 19–26, 2013.

[184] K. N. Kudin, B. Ozbas, H. C. Schniepp, R. K. Prud'homme, I. A. Aksay, and R. Car, "Raman Spectra of Graphite Oxide and Functionalized Graphene Sheets," *Nano Letters*, vol. 8, no. 1, pp. 36–41, 2007.

[185] Z.-S. Wu, W. Ren, L. Gao, J. Zhao, Z. Chen, B. Liu, D. Tang, B. Yu, C. Jiang, and H.-M. Cheng, "Synthesis of Graphene Sheets with High Electrical Conductivity and Good Thermal Stability by Hydrogen Arc Discharge Exfoliation," *ACS Nano*, vol. 3, no. 2, pp. 411–417, 2009.

[186] N. Soin, S. Sinha Roy, S. Roy, K. S. Hazra, D. S. Misra, T. H. Lim, C. J. Hetherington, and J. A. McLaughlin, "Enhanced and Stable Field Emission from in Situ Nitrogen-Doped Few-Layered Graphene Nanoflakes," *The Journal of Physical Chemistry C*, vol. 115, no. 13, pp. 5366–5372, 2011.

[187] C. Zhang, L. Fu, N. Liu, M. Liu, Y. Wang, and Z. Liu, "Synthesis of Nitrogen-Doped Graphene Using Embedded Carbon and Nitrogen Sources," *Adv. Mater.*, vol. 23, no. 8, pp. 1020–1024, Feb. 2011.

[188] D. Wei, Y. Liu, Y. Wang, H. Zhang, L. Huang, and G. Yu, "Synthesis of N-Doped Graphene by Chemical Vapor Deposition and Its Electrical Properties," *Nano Letters*, vol. 9, no. 5, pp. 1752–1758, 2009.

[189] S. van Dommele, A. Romero-Izquirdo, R. Brydson, K. P. de Jong, and J. H. Bitter, "Tuning nitrogen functionalities in catalytically grown nitrogen-containing carbon nanotubes," *Carbon*, vol. 46, no. 1, pp. 138–148, 2008.

[190] A. Yu, A. Sy, and A. Davies, “Graphene nanoplatelets supported MnO2 nanoparticles for electrochemical supercapacitor,” *Synthetic Metals*, vol. 161, no. 17–18, pp. 2049–2054, Sep. 2011.

[191] W. Chen, T. Wen, and H. Teng, “Polyaniline-deposited porous carbon electrode for supercapacitor,” *Electrochimica Acta*, vol. 48, no. 6, pp. 641–649, 2003.

[192] D. Qu, “Studies of the activated carbons used in double-layer supercapacitors,” *Journal of Power Sources*, vol. 109, pp. 403–411, 2002.

[193] A. Burke, “R&D considerations for the performance and application of electrochemical capacitors,” *Electrochimica Acta*, vol. 53, no. 3, pp. 1083–1091, Dec. 2007.

[194] A. Davies, P. Audette, B. Farrow, F. Hassan, Z. Chen, J.-Y. Choi, and A. Yu, “Graphene-based flexible supercapacitors: pulse-electropolymerization of polypyrrole on free-standing graphene films,” *J. Phys. Chem. C*, vol. 115, no. 35, pp. 17612–17620, Sep. 2011.

[195] P. L. Taberna, P. Simon, and J. F. Fauvarque, “Electrochemical Characteristics and Impedance Spectroscopy Studies of Carbon-Carbon Supercapacitors,” *Journal of The Electrochemical Society*, vol. 150, no. 3, p. A292, 2003.

[196] D. Linden and T. Reddy, *Handbook of Batteries*, Fourth Edi. New York: McGraw Hill, 2010.

Appendix

I hereby declare that all images and tables reproduced in this thesis have been licensed for reuse. The standard rightslink permission agreements can be provided upon request.

Content from my publications have been reproduced or altered with appropriate permissions if required. [72], [182], [183]